CRANFIELD UNIVERSITY
School of Aerospace, Transport and Manufacturing
PhD Thesis
Academic Year 2014 – 2017

Clément Bühr

Development of a numerical modelling approach to predict residual stresses in Ti-6Al-4V linear friction welds

This thesis is submitted in fulfilment of the requirements for the degree of Doctorate of Philosophy

Supervisors: Dr Paul Colegrove and Dr Anthony McAndrew
Date of presentation: 1st December 2017

Abstract

Linear friction welding (LFW) is a solid-state joining process which has been successfully implemented to manufacture bladed-disks, chains and near-net shape components. During welding, large residual stresses are created as a consequence of a non-uniform heating of the component which can severely affect the integrity of the structure. Experimental measurement of residual stresses and temperatures on linear friction welds is difficult, so researchers have used modelling to provide a better understanding of these important characteristics. Models developed in the literature, replicate the welding process by including the oscillation of the workpieces, resulting in long computational times. Therefore, numerical models are mostly confined to 2D geometry and complex geometry cases such as keystone or bladed-disk welds are rarely considered. This thesis focuses on the development and validation of computational models capable of predicting the residual stress field developed in Ti-6Al-4V LFW without modelling the complex mechanical mixing occurring at the weld interface. Using a sequentially coupled thermo-mechanical analysis on a 3D model defined in ABAQUS, the heat was applied at the weld interface using the average heat flux post-processed from the machine data obtained during welding trials, for all the phases. The material deformation was ignored and the material expulsion is accounted for by sequentially removing rows of elements.

The models were validated against thermocouples, neutron diffraction and contour method measurements. The shearing occurring at the interface while welding was found to have little effect on the final residual stress field and therefore can be omitted. The residual stress field was found to be driven by the temperature profile obtained at the end of welding, prior to cooling and by the weld interface dimensions. A low weld interface temperature, shallow thermal gradient across the weld and small weld interface dimensions should be sought to minimise the residual stress magnitude. Therefore, a low burn-off rate obtained with reduced welding frequency, amplitude and applied force should be used; however the impact of using these parameters on the microstructure

and material properties may need to be considered. The modelling approach was successfully implemented on a blisk LFW and its peculiar geometry was found to have little effect on the residual stress field as the peak magnitude is driven by the overall length of the part and the thermal profile prior to cooling. Several cycles of post-weld heat treatment were also investigated for the blisk weld. The results showed that all post-weld heat treatments reduced the residual stresses, however the differences between the heat treatments on the resulting stress field was minimal.

In conclusion, the thesis presents an innovative computationally efficient modelling approach capable of predicting the residual stresses within standard and complex geometry LFW.

Acknowledgements

My warmest thanks to my supervisors Dr. Paul Colegrove and Dr. Anthony McAndrew who provided invaluable guidance through my PhD and who were always available to discuss my latest results and ideas.

I would like to acknowledge Dr. Supriyo Ganguly for his expertise on neutron diffraction and more generally for helping me during my PhD. The help of Jan R. Hönnige in conducting the neutron diffraction experiments was greatly appreciated.

Thank you to Dr. Bilal Ahmad and Professor Xiang Zhang for providing the contour method measurement presented in Chapter 4.

Thank you to Bertrand Flipo (TWI Cambridge) and Elena Izvolnesky (KUKA Systems Birmingham) for helping me to make the linear friction welds used in this thesis.

Thank you to Cranfield University notably the Welding Engineering and Laser Processing Centre and Honeywell Aerospace for sponsoring this project.

Special thanks to Daira Legzdina and Vincent Chung from Honeywell Aerospace for their insight into my work and listening to countless presentations.

Thank you to my colleagues of the Welding Engineering and Laser Processing Centre for their friendship.

Un grand merci à mes parents Régine et Philippe Bühr pour m'avoir soutenu dans mes choix d'études et m'avoir permis d'obtenir le plus haut degré de qualification académique. Je n'aurai pu accomplir qu'une fraction de mon parcours sans leurs efforts et leurs amours.

Et bien sûr, merci à ma partenaire de vie Dr. Sabrina Blackwell qui a toujours su trouver les mots d'encouragements dans les moments difficiles, me gardant avec le sourire aux lèvres pendant ces trois ans et plus.

Table of contents

List of figures

The figures displayed in this thesis and their associated page numbers are listed below:

List of tables

The tables displayed in this thesis and their associated page numbers are listed below:

List of equations

The equations presented in this thesis and their associated page numbers are listed below:

List of abbreviations

The abbreviations used in this thesis are listed below:

Abbreviation	*Definition*
1D	One-Dimensional
2D	Two-Dimensional
3D	Three-Dimensional
ANOVA	Analysis of Variance
BCC	Body-Centred-Cubic
Blisk	Bladed Disk
CM	Contour Method
CMM	Coordinate Measurement Machine
CWZ	Central Weld Zone
DOE	Design of Experiments
EDM	Electro Discharge Machining
EXP	Experiment
FEA	Finite Element Analysis
FEM	Finite Element Method
FSW	Friction Stir Welding
FSSW	Friction Stir Spot Welding
HAZ	Heat Affected Zone

HCF	High Cycle Fatigue
HCP	Hexagonal Close Packed
Hv	Vicker’s Hardness
IFW	Inertia Friction Welding
LCF	Low Cycle Fatigue
LFW	Linear Friction Welding
ND	Neutron Diffraction
OFW	Orbital Friction Welding
PWHT	Post-Weld Heat Treatment
RFW	Rotary Friction Welding
RSM	Response Surface Methodology
SD	Synchrotron X-ray Diffraction
TMAZ	Thermo-Mechanically Affected Zone
TOF	Time of Flight
TWI	The Welding Institute
UK	United Kingdom

List of nomenclatures

The nomenclatures used in this thesis are listed below:

Symbol	***Definition***	***Units***
A	Amplitude	m
Ad. Pr.	Adequate Precision	Dimensionless
Adj R^2	Adjusted R-squared	Dimensionless
a	Acceleration	$m \cdot s^{-2}$
Bdxx	Residual stress band width in the *x* direction	m
Bdzz	Residual stress band width in the *z* direction	m
BoR	Burn-off rate	$mm \cdot s^{-1}$
Clp_Px	Clamping pressure normal the *x* direction	Pa
Clp_Pz	Clamping pressure normal the *z* direction	Pa
c_p	Specific heat capacity	$J \cdot kg^{-1} \cdot K^{-1}$
E	Young's modulus	Pa
F_{in}	In-plane force	N
F_{int}	Interface force	N
f	Frequency	Hz
Lxx	Weld interface dimension in the *x* direction	m
Lzz	Weld interface dimension in the *z* direction	m
M	Mass	kg

P	Applied pressure	Pa
Prd R^2	Predicted R-squared	Dimensionless
P-V	P-values	Dimensionless
Q	Heat	J
$\dot{Q}$	Power	W
q	Heat flux	$W \cdot m^{-2}$
$\bar{q}$	Mises equivalent stress	Pa
R^2	R-squared	Dimensionless
Sxx	Stress in the *x* direction	Pa
Syy	Stress in the *y* direction	Pa
Szz	Stress in the *z* direction	Pa
T	Temperature	◦C or K
T_{flash}	Flash temperature	◦C or K
T_{init}	Initial temperature	◦C or K
t	Time	s
t_{phase}	Duration of a phase	s
v	Velocity	$m \cdot s^{-1}$
v_r	Rubbing velocity / Average rubbing velocity	$mm \cdot s^{-1}$
x	Oscillating workpiece displacement	m
α	Thermal diffusivity	$m^2 \cdot s^{-1}$

λ	Thermal conductivity	$W \cdot m^{-1} \cdot K^{-1}$
ε	Strain	Dimensionless
$\dot{\varepsilon}^{cr}$	Uniaxial creep strain rate	Dimensionless
ν	Poisson's ratio	Dimensionless
ρ	Density	$kg \cdot m^{-3}$
σ	Stress	Pa
ω	Angular frequency	Hz

Chapter 1: Introduction

1.1 Background and motivation

Linear friction welding (LFW) is a solid-state joining process which has been successfully implemented to manufacture titanium and nickel-based super alloy bladed-disks[1]. The process works by linearly rubbing one workpiece against another while applying a compressive force. Heat is generated first by friction then by plastic deformation. If appropriate parameters are used, the microstructure at the joint refines, resulting in higher hardness[2] and tensile strength[3] compared to the parent material. LFW is fast compared to other welding process (typically under 10 s) and offers good repeatability[4].

Numerical modelling has been successfully used to gain knowledge on a wide range of outputs including temperature history[5–9], flash morphology[7,9], interface contaminants[8] and effect of processing parameters[10–12]. Residual stresses can affect the structural integrity and are therefore an essential consideration for end users. Measurements of residual stress within LFW are difficult, particularly for the titanium alloys which are the main application of the process due to the steep stress gradients created and experimental limitations; therefore numerical simulations are seen as a practical alternative. Owing to computational constraints inherent to the modelling approaches available in the literature, where people have attempted to model the complex mechanical mixing of LFW at the weld interface between the two parts, very few publications on modelling the residual stress development within LFW structures are published[13,14]. More work on understanding the effect of the process parameters on the residual stress development is needed.

In this context, Cranfield University and Honeywell International Inc. have identified the need to use numerical modelling to gain knowledge on the development of residual stress within LFW. This thesis describes a series of instrumented linear friction welds which aim to provide the thermal history and residual stress measurements for validating the finite element models. The uniqueness of this work is that it bypasses the need of modelling the

computationally expensive oscillations inherent in the process while still accounting for the axial shortening of the workpiece. This approach allowed residual stress modelling of large engineering structures such as bladed-disks with a reasonable computational time. This will have practical benefits and may aid further development and optimisation of the linear friction welding process. This thesis also demonstrates how finite element analysis can be used to predict the effect of parameters on residual stresses developed in rectangular coupons and bladed-disk welds. The content of each chapter is described in the next section.

1.2 Thesis structure

In total, this thesis is composed of seven chapters and four appendices.

Chapter 2 presents an extensive literature review focusing on the LFW process, the titanium alloy Ti-6Al-4V, the computational modelling techniques and the development of residual stress within LFW. The literature review allowed the author to identify the gaps in knowledge and define the objectives displayed in section 2.6, so that the thesis will present an original, significant and rigorous work to contribute to the development of LFW.

Chapter 3 focuses on the development of a 3D thermal model able to predict thermal histories within LFW while bypassing the need of modelling the oscillations. Validation of the numerical predictions against thermocouple data is presented as well as the effects of process parameters on the thermal history.

Chapter 4 extends the work from the previous chapter to a 3D mechanical model capable of predicting the residual stress field without modelling the oscillations. Validation against neutron diffraction and contour method measurements is provided and the effects of the process parameters studied in chapter 3 on the residual stress field are investigated.

Chapter 5 uses the knowledge developed in chapters 3 and 4 to conduct an extensive parametric study to identify variables that have a significant effect on

the residual stresses as well as providing guidelines to mitigate their development.

Chapter 6 applies the methodology previously developed to a bladed-disk joint geometry. The distribution and magnitude of the residual stresses developed on such engineering component are analysed and several post-weld heat treatment cycles are simulated.

Chapter 7 presents the thesis conclusion by summarising the outcomes of the research project and demonstrating that the objectives set have been reached. Finally, recommendations for further research are provided.

Several chapters have been or are intended to be published in a research journal. A reference to the relevant article is given at the start of each chapter.

Chapter 2: Literature review

2.1 Introduction and context

This chapter presents a review of the state of the art of linear friction welding with a particular emphasis on computational modelling techniques, residual stresses and the titanium alloy Ti-6Al-4V. This chapter aims to reveal certain "gaps" in knowledge present in the literature which will constitute the fundamental problems investigated in this thesis.

2.2 Friction welding processes

Friction welding processes are usually solid-state, that is to say no melting of the workpiece occurs. Typically, one workpiece moves while the other is stationary. Heat is generated by sliding friction, plastic work within the material or a combination of the two, between the components facilitating their plasticisation. A force is applied during the process to displace the plasticised layer formed between the two materials and bind them together[4,11,15,16].

Solid-state welding processes possess the advantage of avoiding solidification related problems associated with fusion welding techniques. Therefore, there are usually no issues with oxidation, shrinkage cracks, porosity or hydrogen solubility[17,18]. Furthermore, no filler metal and no shielding gas are required[19]. Friction welding methods create high integrity joints with mechanical properties which usually surpass those of the parent material[2,3,19]. Moreover, the process is easily repeatable since it is fully automated. Since the fusion temperature of the materials is not reached during the process, dissimilar materials can be welded more easily[5,16,17,20,21].

The main friction welding processes are:

Friction stir welding

Friction stir welding (FSW) process was invented at The Welding Institute (TWI), UK in 1991. The machine is made of a non-consumable tool composed of a pin, which penetrates the plates while welding, and a shoulder. The tool

generates heat by friction with the workpiece and its motion will produce the weld by mixing the layers of plasticised material[22], as shown in Figure 2-1.

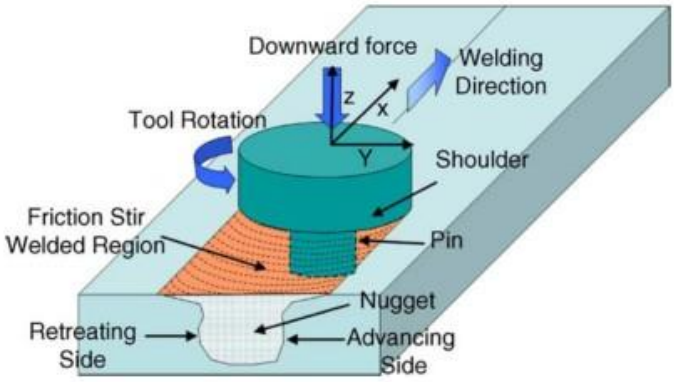

Figure 2-1: Friction stir welding[22]

Friction stir spot welding

Friction stir spot welding (FSSW) is a single point joining process which was created by Mazda Motor Corporation and Kawasaki Heavy Industries. This process is particularly suited to the creation of lap welds, see Figure 2-2. This welding process was inspired by friction stir welding and its main difference lies in the tool movement[23–25]. In friction stir spot welding, the rotating tool is plunged in the overlap sheets however no traversing motion occurs as opposed to friction stir welding. A variation of the process called refill friction stir spot welding exists which eliminates the tool exit hole usually left by friction stir welding and friction stir spot welding.

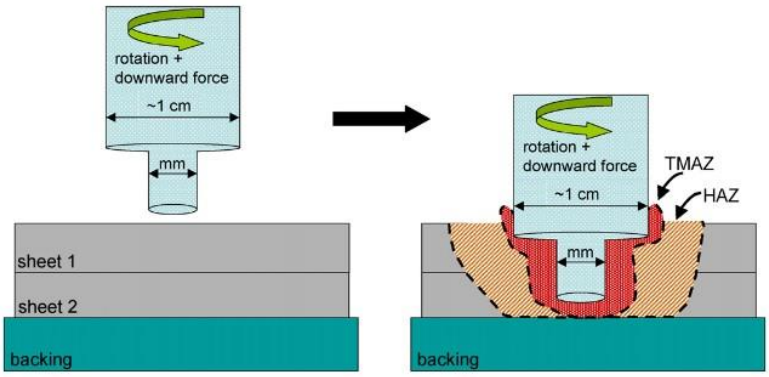

Figure 2-2: Friction stir spot welding[23]

Rotary friction welding/ Inertia friction welding

Rotary friction welding (RFW) is another solid-state joining process commercially used since the 1940s, involving two cylindrical workpieces. One is stationary while the other is rotating. Heating occurs once the two workpieces are in contact due to the normal force applied and the high rotation speed of the rotating workpiece, as shown in Figure 2-3. In contrast to rotary friction welding where the rotational speed is controlled during the whole process, in inertia friction welding (IFW) the rotational part is attached to a flywheel which is accelerated to a certain speed then disengaged while both parts are forced into contact[26]. During both processes, the heat is generated by friction and important plasticisation occurs at the interface of the workpieces. Due to the normal and centrifugal forces, material is expelled, creating a flash[27,28], which contains the contaminants initially on the workpiece interfaces.

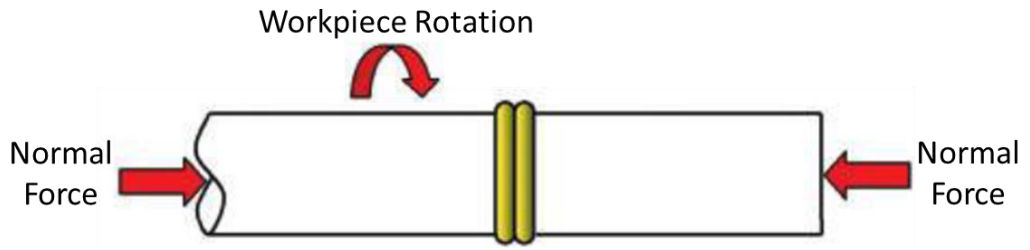

Figure 2-3: Rotary friction welding[19]

Orbital friction welding

Orbital friction welding (OFW) was developed in the 1970s as a combination between linear friction welding and rotary friction welding. In OFW, both parts to be joined are rotated in the same direction with the same constant angular speed while having their longitudinal axes parallel but offsetted by a small distanced d, as shown in Figure 2-4. Orbital friction welding overcomes two important limitations inherent to the rotary process. First of all, the workpieces are not limited to circular cross-sections[19] and secondly, it allows the heat affected zone to have an uniform thickness by creating a uniform heat generation over the interface[19,27].

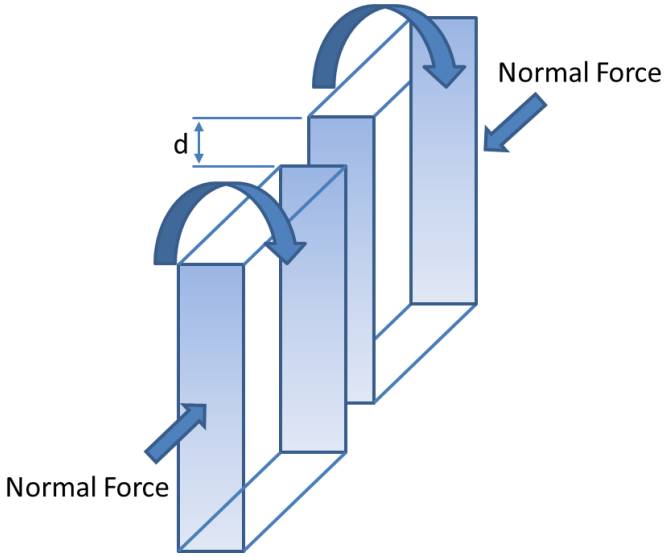

Figure 2-4: Orbital friction welding

2.3 Linear friction welding process

2.3.1 Background

Linear friction welding (LFW) was first patented in 1929[29], however there was little detail recorded on its use. Later on, patents covering particular aspects of the process such as welding methods or tooling concepts, emerged[21].

LFW is also a solid-state joining process and possesses the advantages that come with it. The large deformations undergone by the material during the process usually result in a refined microstructure which can improve the properties of the weld relative to the parent material. Typically, less than 10 seconds are required to complete a titanium alloy weld using LFW, making it a fast welding process which also offers a good repeatability[4]. While welding, parts do not require gas shielding to prevent oxidation[5,17,18,21,30]. The main disadvantage of the process lies in the important cost of the equipment and tooling[19]. Consequently, LFW applications are mostly confined to the aeroengine industry for titanium alloy bladed disk (blisk). Other applications have been found for LFW such as nickel-based super alloy assemblies and non-aeroengine metallic materials[2,5,13,16,21,30], notably, the process is spreading in the chain manufacturing industry[31].

2.3.2 Process phases

During the process a stationary workpiece is rubbed against another workpiece with a linear cyclic motion, under a compressive force to generate frictional heat, see Figure 2-5 a). The process is commonly divided into four phases[2,5,10,11,15], as displayed in Figure 2-5 b).

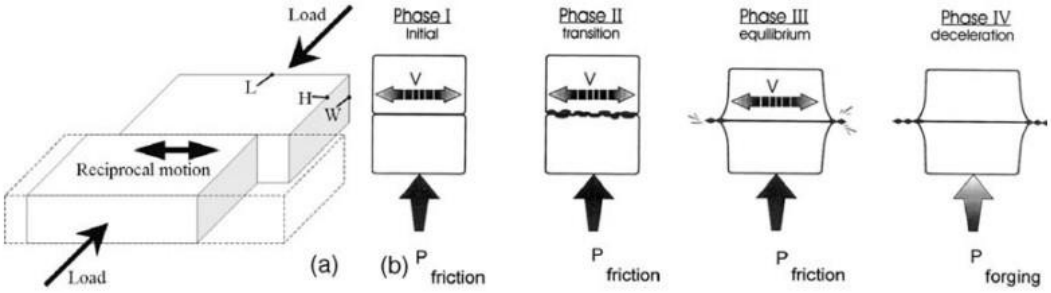

Figure 2-5: Schematic illustration of the LFW process a) and its stages b)[5]

Initial phase:

During the initial phase the two workpieces are forced together. The frictional heat is generated by the asperities at the interfaces of the workpieces, hence the material softens and the asperities wear down. At the end of this phase the true contact area will have considerably increased, as shown in Figure 2-6. During this phase only the asperities wear down, therefore negligible burn-off (axial shortening) occurs.

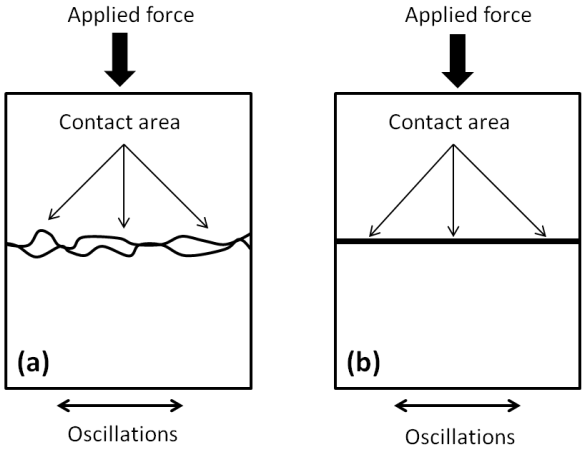

Figure 2-6: Schematic illustration of the contact area at the beginning of the initial phase a) and at the end of the initial phase b)

Transition phase:

During the transition phase, the heat affected zone expands and the temperature is sufficient for the material to plasticise, creating a soft viscoplastic layer which increases the true contact area to 100%. At this point, the viscous material starts to be expelled from the interface creating flash.

Equilibrium phase:

Significant burn-off occurs and most of the flash is created during the equilibrium phase. A quasi-steady state is reached for the interface force, thermal profile and burn-off rate.

Deceleration phase and forging:

Finally, once the desired upset is achieved, the two parts are quickly and accurately aligned. The deceleration time is typically under 0.1 s. Then, a forging force with the same or higher magnitude than the applied force[26] is applied to consolidate the joint for a duration of 5-15 s after the oscillation had ceased.

2.3.3 Process inputs

There are eight main input parameters that control the linear friction welding process.

1. **Frequency** of the oscillations.
2. **Ramp-up time** which is the time taken to reach the values defined for the different input variables.
3. **Amplitude** of the oscillations which defines the maximum displacement from the equilibrium position of the workpiece.
4. **Applied force** called also compressive force or normal force. This is the force applied during the first three phases of the process.
5. **Burn-off** parameter which can be defined as a time, number of cycles or more commonly as a distance. This parameter is often used as the criterion to start the forging process.
6. **Decay time** used to define the duration of the deceleration where the workpieces need to be accurately aligned before starting the forging process.

7. **Forging force** which is the force applied during the fourth phase of the process in order to consolidate the joint.
8. **Forging time** is the duration that the forging force is applied.

Beside these inputs other important parameters influence the process but cannot be easily and accurately defined through the main input parameters despite their dependency.

1. **Upset** which is the total shortening of the workpiece once the welding has been completed. It is the sum of the burn-off plus the loss of length resulting from the forging process.
2. **Shear/ In-plane/ Interface force** which is the force in the direction of the oscillatory motion.
3. **Burn-off rate** is the rate that the burn-off happens.
4. **Welding time** defines the total duration of the process.

2.3.4 Thermal aspect of the linear friction welding phases

During a linear friction weld, the heat can be transferred either by conduction, convection or radiation[10,27,32,33] with conduction being the primary transfer mechanism[32,34]. Convection phenomena may arise from heat transfer with the atmosphere or/and tooling. LFW, as also in RFW, exhibits a conditioning phase which includes the initial and transition phases, where the temperature at the interface rises until it reaches a maximum. This conditioning phase is followed by an equilibrium phase where the interface temperature remains constant due to a dynamic balance between heat input, heat conducted away and material expelled[12,35]. This trend is illustrated in Figure 2-7, where the temperature at the interface (z=0) increases only during the heating stage (i.e. conditioning phase), while back from the weld interface (z>0), the temperature keeps rising because of the burn-off occurring. Indeed, a point located further away from the interface will have a lower temperature than a point at the interface at a given time. As a consequence of having the material expelled (i.e. burn-off), this point will get closer to the interface and eventually reach it.

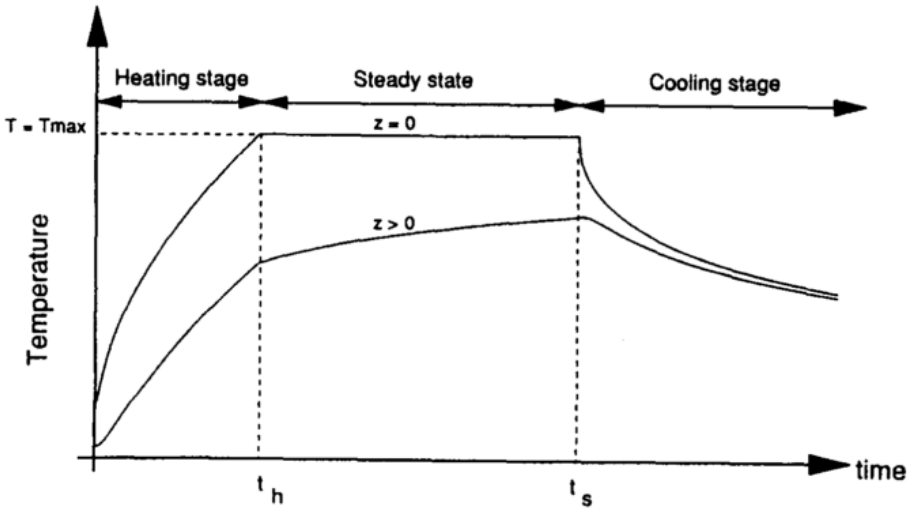

Figure 2-7: Schematic diagram showing the three main process stages in friction welding ($\mathbf{t_h}$: **heating time,** $\mathbf{t_s}$: **welding time and** $\mathbf{T_{max}}$: **maximum temperature located at** $\mathbf{z = 0}$)[35]

Two examples of thermal histories recorded using thermocouples are shown in Figure 2-8. Temperature trends previously described can be retrieved from the experimental measurements. The equilibrium phase has been clearly captured by the thermocouples of Schroeder et al.[9], see Figure 2-8 b). It is worth noting that Schroeder et al.[9] did not disclose the distances, back from the weld interface, at which the thermocouples were positioned. The steady state of the temperature during the equilibrium phase is less obvious on the measurements made by McAndrew et al., see Figure 2-8 a) and is believed to be a consequence of the viscous material entering in the thermocouple hole and pushing back the thermocouple. This issue was also encountered by Vairis et al.[33].

Typically for titanium alloys welded with LFW, maxima of temperature were found between 900ºC and 1400ºC[6,8–10,33,36–38]. Temperatures are mainly predicted by numerical models due to the difficulty of measuring the temperature at the weld interface which changes continuously during the process because of the burn-off[8,34]. Consequently, thermocouples are often positioned further back from the interface[8,10,33,34] which makes it difficult to predict the interface temperature owing to the steep thermal gradient.

Alternatively, Maio et al.[38] used infrared thermography for monitoring the heat generation in Ti-6Al-4V LFW where temperatures were found between 1050 ºC and 1200 ºC at the weld interface. However flash obstruction perhaps remains the main limitation of this technique making thermocouples a preferred technique in the literature.

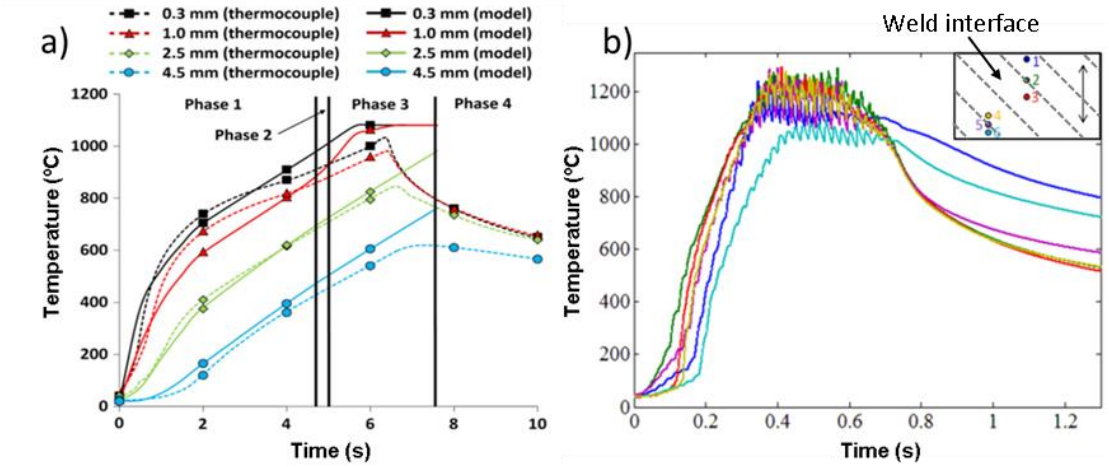

Figure 2-8: a) A comparison of thermal histories predicted numerically and measured using thermocouples by McAndrew et al.[8] extracted at different distances, prior welding, back from the weld interface b) thermal histories measured using thermocouples by Schroeder et al.[9] where their location on the weld interface is shown on the top right corner, with the oscillation direction indicated by the arrow

2.3.5 Material used and industrial applications

A large panel of materials from metals to plastic[39,40] and even wood[41–43] have been welded using LFW. Materials with good high-temperature properties including low thermal conductivity and compressive yield and shear strength are particularly suitable for the process[21,44]. Such properties will rapidly generate heat by plastic deformation while retaining the heat at the weld interface.

Research on LFW has been mostly carried out on titanium alloy parts[12,20,45–47] with an emphasis on the Ti-6Al-4V grade[2,3,8–11,37,45,48–51]. Nickel-based superalloys[26] have also received a lot of attention since it is also used to manufacture blisks. Ti-6Al-4V blisks are used in moderate temperature environments like aero fans and compressors (up to 300ºC) while nickel-based

superalloy blisks can be used for the higher temperature regions such as the last stages of the high pressure compressor and turbines[1].

A blisk is an alternative to a mechanically attached blade-disk, see Figure 2-9. In a blisk, the blades and disk are made in a single piece, allowing a weight reduction usually between 20 – 30%[1,52,53], improved aerodynamic efficiency with a reduction of the leakage flows[1] and it eliminates potential fatigue cracks arising from mechanical joints[1]. The downsides of the blisk are its cost and its laborious manufacturing and repairing processes[1]. A blisk can either be manufactured from a single block of material or by linear friction welding the blades to the disk. Manufacturing a blisk from a single block is a slow and costly process with a significant amount of material wastage.

More generally, LFW can be used to manufacture preforms (see Figure 2-10) by joining smaller structures together before machining, which reduces the buy-to-fly ratio[49] and therefore the manufacturing cost.

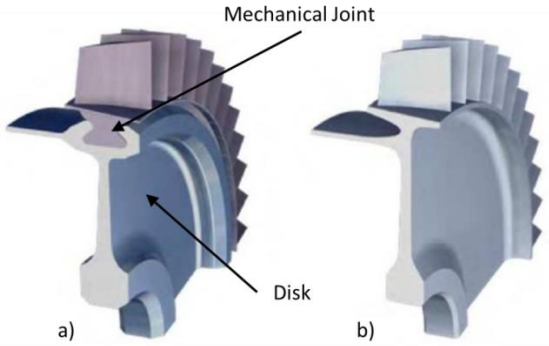

Figure 2-9: a) Blade-disk with mechanical joint and b) linear friction welded blisk[1]

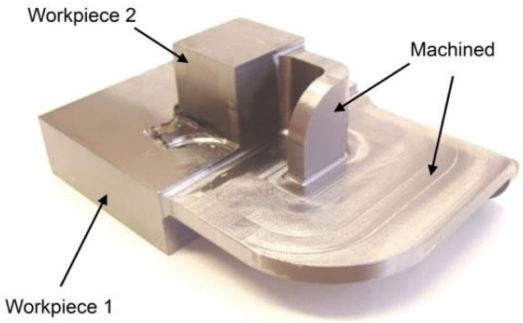

Figure 2-10: A Ti-6Al-4V LFW preform: on the left the as-welded structure and on the right the structure after machining[49]

Several aluminium alloys[16,54–57] and steel grades[34,58] have been successfully used with linear friction welding. Mechanical properties were at least equal or superior to the parent material. Furthermore, dissimilar materials have also been linear friction welded, including pure copper to pure aluminium[59], aluminium alloy to magnesium alloy[60] and titanium alloy to steel[61].

2.3.6 Ti-6Al-4V microstructure

Prior welding (parent material)

Ti-6Al-4V is approximately composed of titanium containing 6% aluminium and 4% vanadium. Ti-6Al-4V has an alpha-beta microstructure, where the alpha phase is stabilised by the aluminium while the beta phase is stabilised by the vanadium[62].

There are three typical types of microstructures encountered with alpha-beta titanium alloys: fully lamellar, fully equiaxed and bi-modal, which are shown Figure 2-11[62,63]. The type of microstructure developed depends on the thermo-mechanical treatments undergone by the material during the manufacturing process. Lamellar microstructures are obtained by simply cooling the material from a temperature above the beta-transus temperature which is the temperature upon which the original alpha-beta microstructure forms a single beta-phase microstructure. To obtain the equiaxed microstructure, the material needs to be highly deformed to force its recrystallization. Lamellar structures offer high fracture toughness and superior resistance to creep and fatigue crack growth while equiaxed structures have high ductility and fatigue strength[62]. Regarding linear friction welding, the bimodal microstructure is often used[2,8,11,18,37,45,50] because it combines the advantages of both lamellar and equiaxed microstructures, i.e. it has a balanced property profile[62].

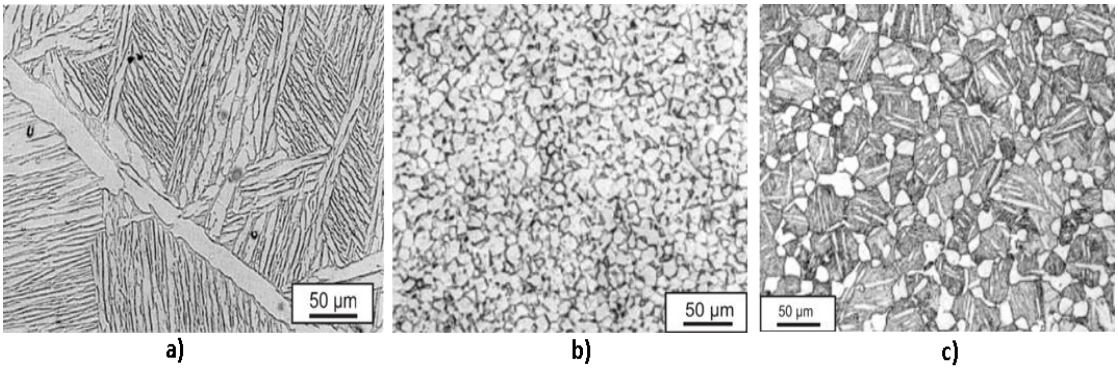

Figure 2-11: alpha-beta titanium alloy microstructures: a) fully lamellar, b) fully equiaxed and c) bi-modal[62]

After welding

During welding, the base material undergoes large deformations at high temperature which deeply affect its microstructure despite little or no melting occuring. The literature typically divides the microstructure of a linear friction weld into four areas[2,20,21,37,50,64] which are presented Figure 2-12.

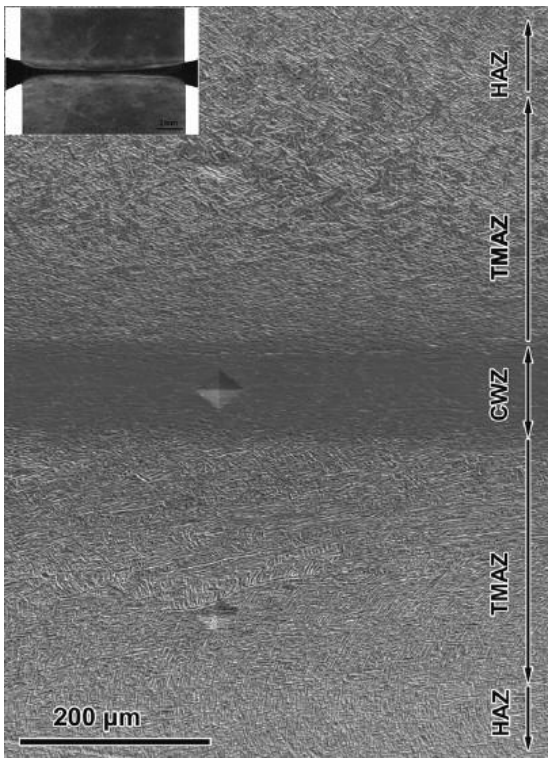

Figure 2-12: Metallographic section of a titanium alloy LF weld[20]

The combination of temperatures near or above the beta-transus temperature (~995ºC[50] for Ti-6Al-4V), and the large deformations undergone by alpha-beta titanium alloy LFW, triggers dynamic recrystallization of the material at the central weld zone (CWZ) resulting either in a Widmanstatten or Martensitic microstructure depending on the cooling rate (see Figure 2-13).

The CWZ exhibits a fine grain microstructure (grains typically under 10µm) with superior hardness properties in a 450-500 Hv range[37] compared to the parent material (about 300 Hv[2,6]). The thermo-mechanically affected zone (TMAZ) displays a heavily deformed alpha-beta microstructure with grains elongated in the oscillation direction, and lower hardness values are found in this region compared to the CWZ (360-400 Hv). The presence of alpha grains from the parent material, in addition to the lack of recrystallization in this region, lead researchers to conclude that the beta-transus temperature was not reached during the process in the TMAZ[2,37,48]. Finally, the heat affected zone (HAZ) does not undergo plastic deformation however the high temperature in this area results in a coarsening of the microstructure and as a result the hardness is often found to be inferior to the parent base material's hardness[37,50] although there are examples of TMAZ with higher hardness than parent material[65].

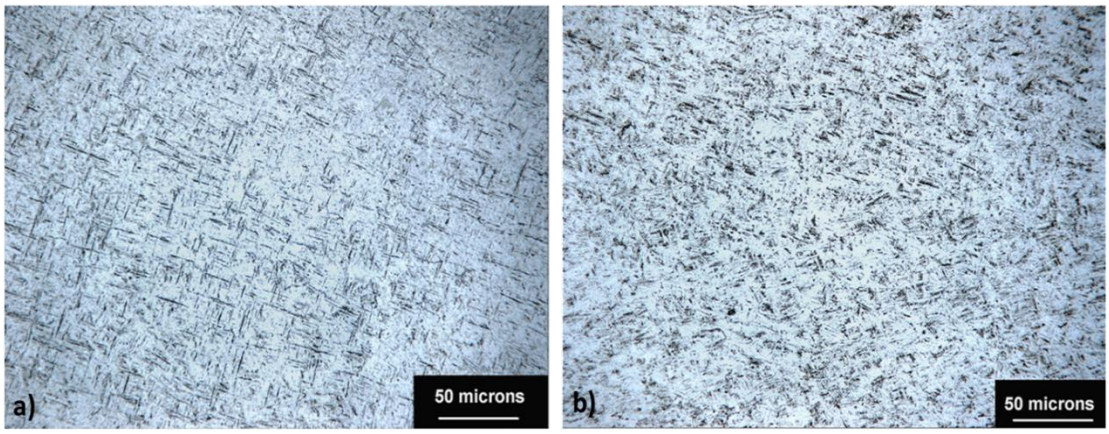

Figure 2-13: Ti-6Al-4V LF weld microstructures: a) Martensite and b) Widmanstatten[11]

2.4 Residual stresses

2.4.1 Background

Residual stresses are the stresses remaining within a component when no external force is applied[66]. They arise from misfits within the material caused by non-uniform plastic flow, steep thermal gradients and phase transformations[16,30,66]. Residual stresses can be beneficial, as in tempered glass, where they prevent crack propagation; or they can be critical, as in welding, where they may reduce significantly the fatigue life of a component.

Residual stresses combined with external loading, poor microstructure and existing defects, may lead to dangerously lower stress at which failure happens. Therefore, it is crucial to account for the effect of residual stresses during a structural integrity assessment, which adds to the manufacturing cost.

Note that within this thesis the analysis of residual stress is confined to type I macro stresses. Type II intergranular and type III atomistic residual stresses are not considered[66].

2.4.2 Residual stress formation in welding

Residual stresses are difficult to predict owing to the multiple factors that cause them, from the manufacturing processes to the service life history. In fusion and solid-state welding processes, the heat distribution and the temperature dependant material properties have the most significant influence on the residual stress formation[13,50,66,67]. However, the residual stress formation is also driven by the geometry of the workpiece, its thermal history, phase transformations and mechanical boundary conditions[66].

Welding processes generally involve high heat inputs which generate a steep thermal gradient across the weld. Under such thermal gradients, the heat affected zone due to thermal expansion tries to expand, but is constrained by the cold parent material, and therefore compressive stresses are created in the joint. Once compressive stresses have reached the material yield stress, plastic

deformations happen. Finally, a non-uniform cool down of the workpiece occurs, therefore the material tries to contract resulting in tensile stresses in the joint. These tensile stresses may overtake the tensile yield stress creating more plastic deformations. Compressive residual stresses are located elsewhere in the workpiece to counterbalance the tensile residual stresses present in the weld.

2.4.3 Effect of residual stress

The modes of failure discussed below are the most common modes where type I residual stresses (i.e. macro-stresses) affect the integrity of a structure.

Fracture and fatigue

Residual stresses affect both the resistance to fracture and the fatigue life of a component and need to be considered in addition to external loads. For a fracture assessment, considering a linear elastic body, the stress intensity contribution of residual stresses simply needs to be added to the stress intensity factor[66]. However, for an elastic-plastic body a finite element code has to be used to calculate the Rice's contour integral[66] to determine the contribution of residual stresses on crack propagation.

Fatigue has been divided in two categories[68], low cycle fatigue (LCF) and high cycle fatigue (HCF). Residual stresses have little effect on LCF since the stresses applied as external loads during the fatigue test are usually above the yield stress triggering failure before 10000 cycles. As a consequence, residual stresses are significantly relaxed by the large amplitude oscillating plastic strains. However, HCF can be positively affected by compressive residual stress mean, if they bring into contact the crack faces during the fatigue cycle, preventing variation in the crack-tip stress intensity. Although, with high tensile residual stresses, the mean stress becomes more tensile and induced closure effects become less likely[66].

Stress corrosion cracking

Stress corrosion cracking is a mode of failure mainly considered by the energy, oil and gas companies. When the structure is exposed to a corrosive environment, despite low magnitude mechanical stresses applied, failure of the structure may happen. Residual stresses in combination with a corrosive environment may initiate a crack in these environmental conditions[30,69].

Distortion

As previously explained, tensile residual stresses are located at the bond line and are balanced by compressive residual stresses further away. The response of the material to the residual stress field is to minimize the strain energy by distortion[70]. Masubuchi[71] distinguishes several types of distortion that can cause either bending, rotation and/or buckling, they are known as welding shrinkage distortion and are presented in Figure 2-14. Several methods exist to mitigate distortion by either reducing the plastic strained region during and after welding, elongating the region that contracts during welding or compensating the welding deformations by pre-welding deformations in the opposite direction before welding[72].

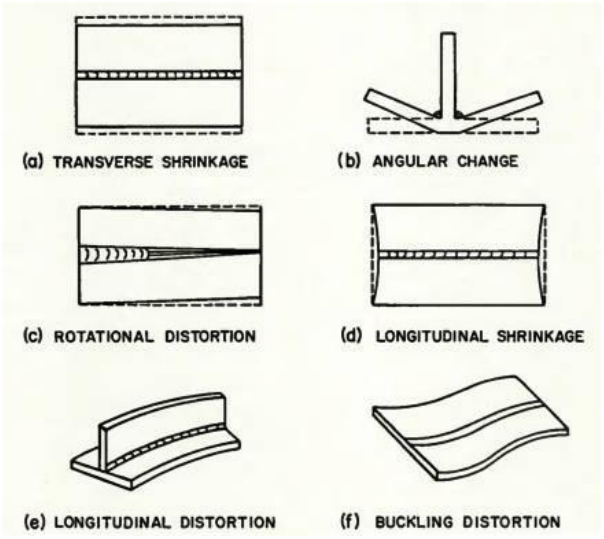

Figure 2-14: Various types of weld distortion[71]

2.4.4 Residual stress measurements

Measuring residual stresses is difficult[66], especially for titanium alloys. Residual stress measurement techniques can be separated in two categories: the destructive and non-destructive.

Residual stress measurements on LFW are mostly performed using the destructive contour method[18,45,64,73] or non-destructive neutron diffraction[18,51,74] and synchrotron X-ray diffraction[16,45,50] techniques.

Contour method

The contour method was first presented at a conference in Oxford in 2000 by Prime[75] making it a relatively new technique for residual stress measurement. A schematic diagram showing how it works is presented in Figure 2-15. A 2D part containing residual stresses is shown in Figure 2-15 a); note that the principle applies equally in 3D. The part is cut, relaxing the normal stress σ_{xx} and the shear stress σ_{xy} and causing the new free surfaces to distort, as shown in Figure 2-15 b). Wire electro discharge machining (EDM) is typically used to make the cut. A coordinate measurement machine (CMM) records the displacement in the *x* direction on the new free surfaces. Finally, an FE model is created to represent the distorted parts which are then forced back to flat surfaces to retrieve the original residual stress state, see Figure 2-15 c).

Unfortunately, only the stresses in the normal direction of the free surface can be retrieved since measurements provide only the displacement in the *x* direction, therefore the shear stress field cannot be deduced. A finite element model (FEM) is usually created to retrieve the residual stress field from the measured displacements. However, for convenience and since the problem is purely elastic, the model considers a flat surface where the negative values of the displacement previously measured are applied.

Three assumptions need to be fulfilled to apply this principle. First of all, the residual stress relaxation after cutting is only elastic. Secondly, the cutting method does not introduce stresses and finally the cut must happen in a plane

that was flat in the uncut part. In reality, cutting artefacts, bulge errors and plastic deformations occur, leading to significant uncertainities[45,76,77]. While cutting artefacts can be avoided by the use of appropriate EDM parameters and clamping, bulge errors and plastic deformations are dependent on the initial residual stress field and are more difficult to control. Bulge error occurs when the third assumption previously mentioned is not respected and is a consequence of the stress relaxation at the tip of the cut, deforming the material. Therefore, when the cut surface is forced back to a flat surface, the material will not return to its original position[78]. Bulge errors can be minimised by using thinner wire, improving clamping and conducting an iterative FE analysis[79]. Unlike bulge errors, cutting-induced plasticity cannot be corrected for after the part is cut[76]. Cutting-induced plasticity is a consequence of the stress concentration at the tip of the cut and generates plastic strains even when far-field residual stresses are lower than the yield strength[76].

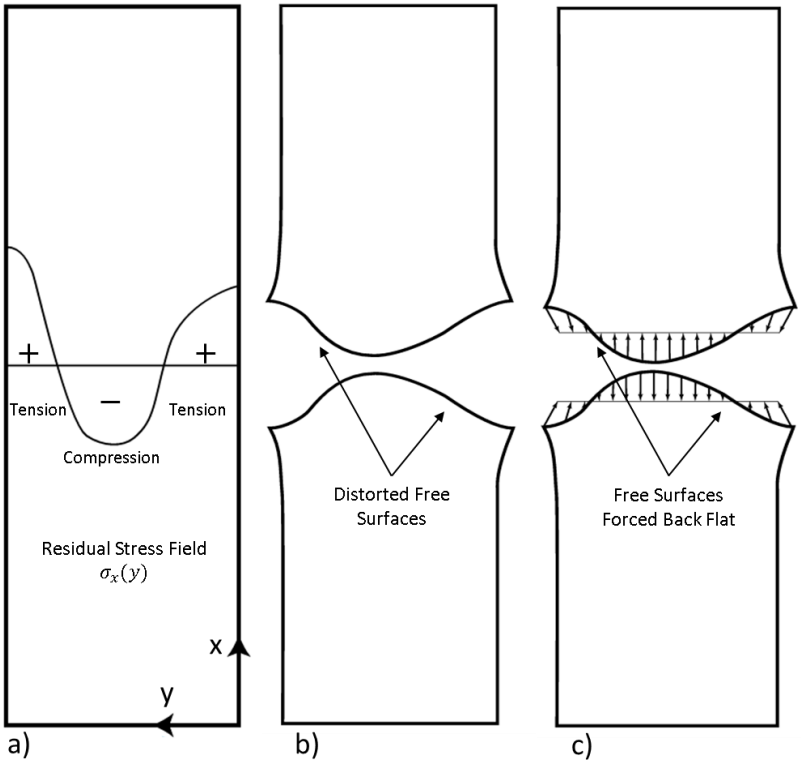

Figure 2-15: Schematic illustration of the different steps required in contour method: a) initial part containing residual stresses, b) cut of the part and c) distorted surfaces forced back flat

Neutron diffraction and synchrotron X-ray diffraction

Neutron diffraction and synchrotron X-ray diffraction both rely on the same diffraction principle which happens when an incident wave gets scattered by the atoms contained in a crystal, given that the wavelength of the wave has the same order of magnitude as the distance between the atoms. Being scattered, the incident beam creates in-phase scattered waves leading to constructive interference and producing a strong outgoing wave[80]. This behaviour is described by Bragg's law (see equation 2-1) and is illustrated Figure 2-16. As a consequence of Bragg's law, the spacing of lattice planes in a crystal can be either deduced by varying the incident wavelength or by detecting the signal of the outgoing wave from different angles of θ, using the relationship:

$$\boldsymbol{n\lambda = 2dsin(\theta)} \qquad 2\text{-}1$$

where λ is the wavelength of the incoming wave, n an integer, d the distance between two planes of atoms and θ the angle of incidence of the incident wave.

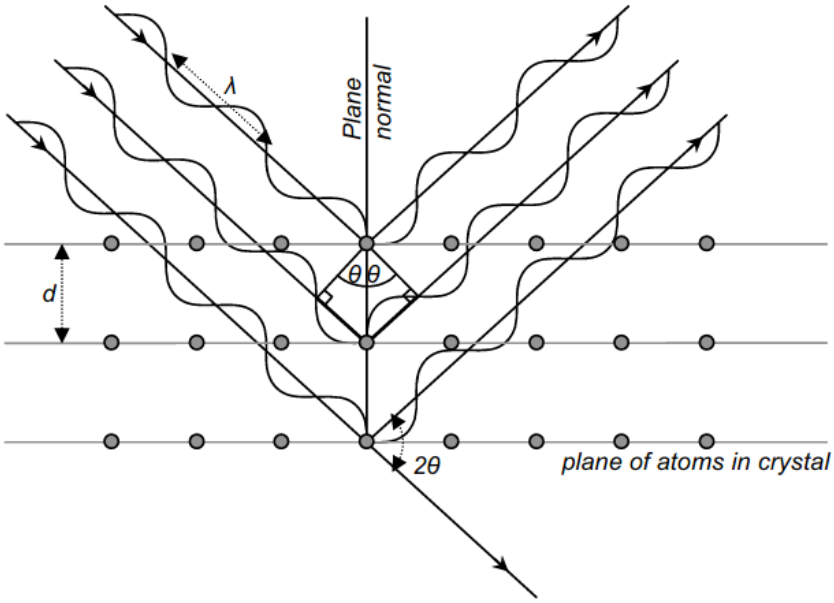

Figure 2-16: Illustration of Bragg's law[81]

Changes in lattice spacing are a consequence of elastic strains and can be linked with the diffraction angle[66] θ with equation 2-2:

$$\boldsymbol{\varepsilon = \frac{d - d^o}{d^o} = -cot(\theta)\Delta\theta} \qquad 2\text{-}2$$

where ε is the elastic strain, d^o the strain-free lattice spacing and $\Delta\theta$ the angular shifts. Finally, the residual stress value can be retrieve using the Hooke's law.

The difference between the neutron diffraction and synchrotron X-ray diffraction techniques lies in the type of radiation used to measure the atomic lattice spacing (i.e. the first uses a neutron beam while the second uses an X-ray photon beam). Neutron diffraction offers a better penetration into materials than X-ray, however it leads to noticeably higher counting times[66] (typically two orders of magnitude[81]). Furthermore, smaller gauge volumes (in at least two directions) can be used with X-ray compared to neutron diffraction but X-ray is more affected by highly textured material and large grain sizes.

Residual stress measurements in Ti-6Al-4V LFW

The main works from the literature on residual stress measurement on Ti-6Al-4V LFW parts are presented in Figure 2-17. Lengths of the longitudinal and transverse directions of the weld interface (i.e Lxx and Lzz, see Figure 2-18) are indicated in Figure 2-17.

Results in Figure 2-17 clearly show that the highest peak of residual stress is reached in the longest direction of the weld interface. Interestingly, the work from Daymond et al.[51] (Figure 2-17 a)) shows that if the two directions of the weld interface have a similar length it results in an equivalent residual stress profile in both directions. On the other hand, if a direction of the interface is noticeably smaller than the other (see Figure 2-17 b) from Dewald et al.[18]), low residual stress will develop in the shortest direction, as if a plane stress condition has been reached. Residual stresses developed in the direction of the applied pressure have a consistently a low magnitude. In the longest direction of the weld interface, peaks of magnitude range between 415 to 850 MPa and the band of tensile residual stress measured between 1.80 to 8 mm. These trends agree with the statement of Bhamji et al.[21] who claims that residual

stresses in LFW are affected by the weld geometry; however the mechanism by which it occurs is not yet fully understood.

Dewald (Figure 2-17 b)) and Frankel (Figure 2-17 c)) compared their measurements which were obtained with neutron diffraction and synchrotron X-ray diffraction respectively with the contour method, in the longest direction of the weld interface. In both cases, the contour method under-predicted the value of the maximum residual stress peak (up to 200 MPa). Furthermore, the band of tensile residual stress was also predicted to be wider by the contour method process in Frankel's work. High stress gradients are challenging to measure accurately for all measurement techniques. Dewald et al.[18] explain that part of the difference between the two techniques is due to the contour method which tends to smooth out the surface features created by high stress gradients. Frankel et al.[45] thought that the EDM cut could have introduced artefacts resulting in non-conservative results predicted by the contour method process. It is also worth mentioning that neutron and synchrotron X-ray diffraction measured values of residual strains are averaged over different gauge volumes (respectively 2 x 2 x 2 mm, Dewald et al.[18], and 0.25 x 0.25 x 3 mm, Frankel et al.[45]) meaning that the actual residual stress peak magnitude could be potentially much higher.

Romero et al.[50] (see Figure 2-17 d)) measured residual stresses on two coupons welded with a respective applied pressure of P and 9P. The value of P is not disclosed by the authors. Romero claims from his results that increasing the applied pressure decreases the magnitude of tensile residual stresses located in the part, although it is not clear on the figure.

It should be noted that Frankel and Romero do not display residual stress measurements at the weld centre line. Frankel encountered abnormal changes in the diffraction peaks recorded at the centre line because of the highly textured material. This is certainly a consequence of having used two separate instruments to measure the spacing of lattice planes (high energy synchrotron X-ray diffraction with a gauge volume of 0.25 x 0.25 x 3 mm) and the strain-free lattices (synchrotron X-ray diffraction with a beam size of 1 mm). Romero did

not record data at the weld centre line because the two joined block had originally two different microstructures which in combination with the size of the gauge volume would have led to inaccurate strain-free lattice measurements.

To conclude, measuring residual stress in titanium alloy LFW is challenging because of the steep stress gradients encountered. Furthermore, despite neutron diffraction offering the deepest penetration, the maximum path length of neutron within titanium is approximately 18 mm[82] resulting in only thin LFW having the ability to be measured.

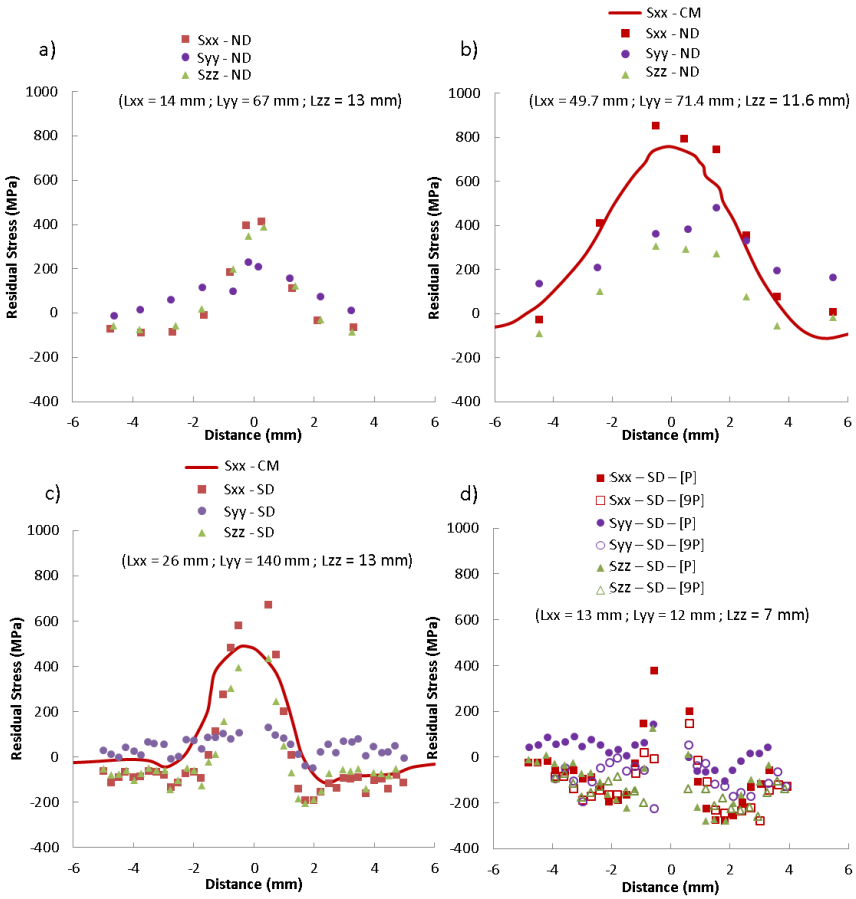

Figure 2-17: Residual Stress measured across the weld using different techniques (ND : neutron diffraction, SD: synchrotron X-ray diffraction, CM: contour method) on Ti-6Al-4V LFW by several authors: a) Daymond et al.[51], b) Dewald et a.[18], c) Frankel et al.[45] and d) Romero et al.[50] (with P and 9P the magnitude of applied pressures used)

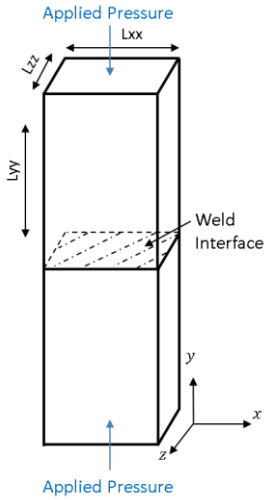

Figure 2-18: Schematic illustration of a LFW

2.4.5 Post-weld heat treatment

Post-weld heat treatment (PWHT) is the main technique used to mitigate residual stresses contained in LFW parts[3,45,47,48,73,83–86]. During PWHT, the structure is uniformly heated until a target temperature is reached which will be held for several hours before cooling at a slow rate to avoid introduction of new residual stresses. Usually, the target temperature used is under the recrystallization temperature to avoid any modification in the material properties. However, the temperature must be high enough to lower the yield stress and allow the material to yield due to the internal residual stresses[66,87]. Creep mechanisms will also influence the relief of the residual stresses[66,87]. PWHT is not universally applicable, it may result in over-aging the material or in the case of dissimilar materials, introduce new mismatching elastic strains due to differences in thermal expansion coefficients[30].

The literature is scarce on the effect of PWHT on residual stresses for LFW joints. Frankel et al.[45] performed two PWHT on Ti-6Al-4V LFW parts where the two target temperatures used are described as the conventional aging temperature of Ti-6Al-4V (about 550ºC according to the literature[63,88]) and 100ºC above (about 650ºC), the duration of the PWHT is not displayed. Considering a Ti-5Al-2Sn-2Zr-4Mo-4Cr (Ti17) LFW part, Xie et al.[73] used a target temperature of 630ºC, held for 3h to performed their PWHT. In Figure

2-19 a) and b), the longitudinal direction of the weld interface is indicated by its length. Results from Frankel et al. indicate that the target temperature of about 650ºC offers a near-complete stress relief of the structure, as shown Figure 2-19 a). Large discrepancies in the residual stresses were observed between the synchrotron X-ray diffraction and contour method results, for the PWHT at aging temperature. Indeed, the contour method seems to indicate an important stress relief after PWHT while the synchrotron method reveals a residual stress distribution almost unchanged compared to the as welded residual stresses. The reasons behind those discrepancies are the same as the ones described earlier in this thesis (see Residual stress measurements in Ti-6Al-4V LFW). Measurements of residual stresses conducted by Xie et al.[73] indicate a complete stress relief of the Ti17 structure after PWHT when a temperature of 630ºC is held for 3h (Figure 2-19 b)).

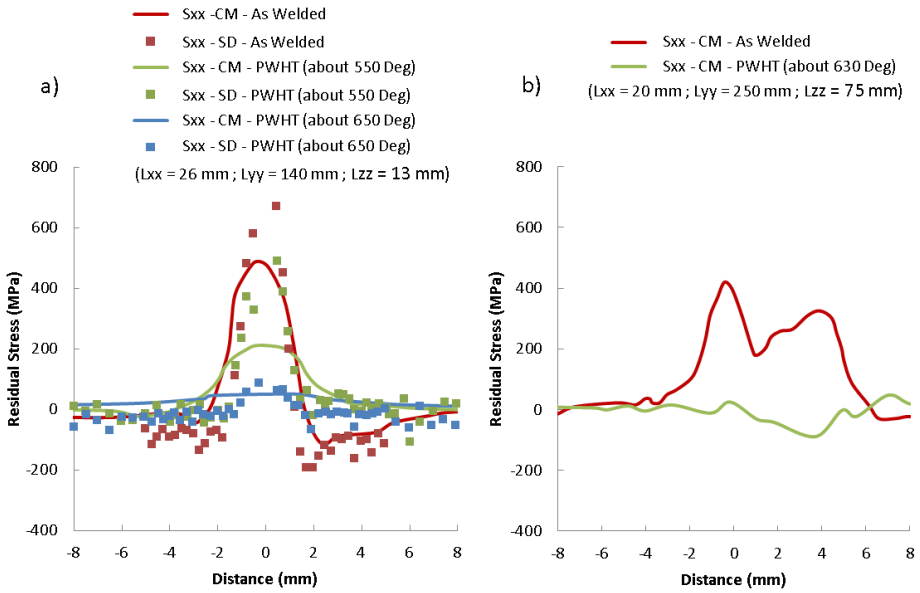

Figure 2-19: Residual Stress as welded and after PWHT measured across the weld interface in the longitudinal direction, using different techniques (SD: synchrotron X-ray diffraction and CM: contour method) by: a) Frankel et al.[45] on Ti-6Al-4V LFW and b) Xie et al.[73] on Ti17 LFW

2.5 Modelling of the linear friction welding process

Measuring residual stresses and temperatures on linear friction welds are difficult to achieve experimentally due to the high stress and temperature gradients created by the welding process, the technical limitations implied by the different measurement approaches and the accessibility of the equipment. Modelling is an alternative way to gain fundamental knowledge while by-passing the inherent difficulties linked with experiments. It can be achieved by establishing an equation predicting certain outputs of the process (analytical modelling) or one can use computational methods such as the finite element technique to predict the outputs.

2.5.1 Analytical modelling

Vairis and Frost are known as the first to have developed an analytical model capable of predicting the temperature evolution during the initial phase of the LFW process[33]. Inspired by the work of Carslaw and Jaeger[89], they assimilated the LFW setup to a solid delimitated by two parallel planes. One of these planes represents the rubbing interface where a heat flux is applied as a boundary condition. Consequently, the temperature T is given as a function of time t at a position x from the interface and is expressed by the equation 2-3:

$$T = \frac{2^{m+1} q_0 \sqrt{\alpha t}^{\frac{m+1}{2}} \Gamma(1/2\, m+1)}{\lambda} \sum_{n=0}^{\infty} \left\{ i^{m+1} erfc \frac{(2n+1)L_0 - x}{2\sqrt{\alpha t}} + i^{m+1} erfc \frac{(2n+1)L_0 + x}{2\sqrt{\alpha t}} \right\} \qquad 2\text{-}3$$

where m is a constant, q_0 the heat flux (power per unit area), α the thermal diffusivity, λ the thermal conductivity, Γ the gamma function, $erfc$ the complementary error function, L_0 the length of the specimen and $i^2 = -1$. However it is worth noting that if $m \neq 0$, the equation 2-3 appears to be dimensionally inconsistent.

Several hypotheses have been assumed to estimate the heat input q_0, notably: the true-contact area increases linearly from zero to the cross section area of the workpiece, no heat losses are considered due to the short duration of the process and the coefficient of friction increases with the time from 0.25 to 0.55 which affects the value of the heat flux.

Vairis and Frost computed equation 2-3 for the two cases where the material properties of Ti-6Al-4V were kept constant and also for temperature dependent properties. The temperature predictions were compared with data acquired by a thermocouple located 1.6 mm back from the interface prior welding. Figure 2-20 displays a reasonable agreement between the temperature history experimentally measured and the one predicted by the model with temperature dependent material properties. On the other hand, large discrepancies are exhibited by the model with constant material properties highlighting the need to account for temperature dependency.

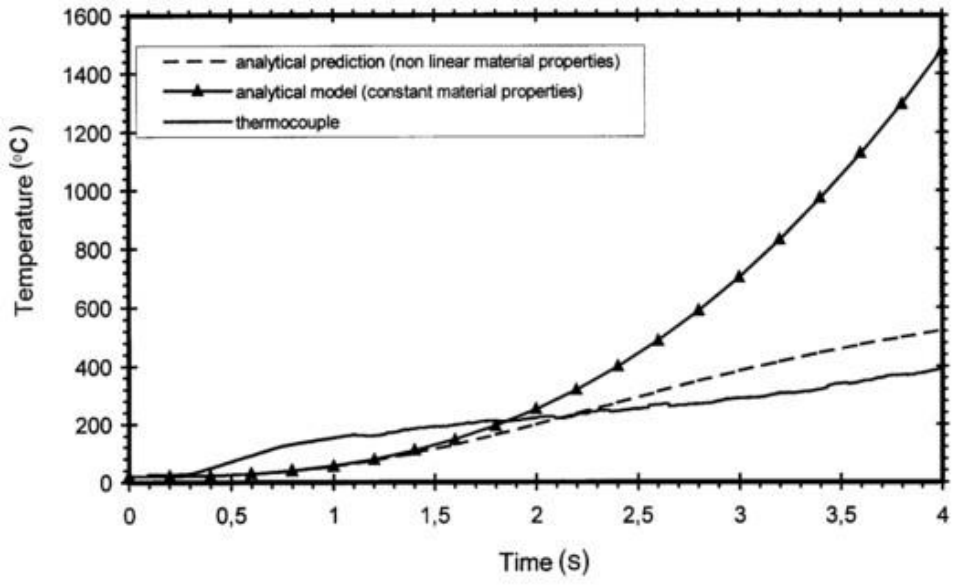

Figure 2-20: Comparison of the temperature history experimentally measured and analytically predicted[33]

Li et al.[90] also established an analytical model, based on a 1D transient-heat-conduction approach, able to predict the heating of a LFW part during the initial phase, see equation 2-4. The titanium alloy Ti17 was considered in the model,

the temperature predicted was shown to increase higher than 1000 °C in less than 0.3 s, capturing the fast heating process experienced by a LFW part.

$$T = T_0 + \frac{2q_0\sqrt{\frac{\alpha t}{\pi}}}{\lambda} \exp\left(-\frac{x^2}{4\alpha t}\right) - \frac{q_0 x}{\lambda}\left(1 - erf\left(\frac{x}{2\sqrt{\alpha t}}\right)\right) \quad \text{2-4}$$

where T_0 is the initial temperature, λ is the thermal conductivity and erf the error function.

None of the models above are capable of predicting the quasi-steady state of the temperature characteristic of the equilibrium phase where a balance between heat input and heat losses gets established. However, Turner et al.[10] developed an equation which estimates the thermal profile in the HAZ during the equilibrium phase:

$$T = T_0 + (T_{flash} - T_0) \exp\left(-\frac{vx}{\alpha}\right) \quad \text{2-5}$$

where T_{flash} is the temperature of the flash and v the burn-off rate. A good match was found between the predictions of the equation and Turner's numerical model. It is worth mentioning that the analytical model is retrospective since the flash temperature and the burn-off rate need to be known before solving.

Analytical modelling is a practical way to get an insight into the process. However it often requires significant simplifications limiting its predictive capability. When a problem becomes too complex to be accurately represented by an analytical equation, numerical modelling can be employed to get an improved prediction.

2.5.2 Numerical modelling

Finite element analysis

Almost exclusively, the finite element analysis (FEA) method is used to numerically model the LFW process. FEA involves discretizing the space

domain into a finite number of elements with nodes at the corners of the elements. After defining the interpolation functions (e.g Gauss integration), computation is carried out on each element to determine their stiffness matrix (i.e. characteristic forces and displacements), mathematically defined by:

$$[k]_e\{\delta\}_e = \{F\}_e \qquad 2\text{-}6$$

where $[k]_e$ is the element stiffness matrix, $\{\delta\}_e$ is the nodal displacement vector of the element and $\{F\}_e$ its force vector.

Finally, the element stiffness matrixes are assembled to form a global stiffness matrix[91,92] of the structure, and the boundary conditions are imposed in order to solve the system equations and get the nodal unknowns such as stress and strain.

Different FEA packages are used to model the LFW process, including: ABAQUS[5,12,14,32,34,37,46,52,58,59,86], ANSYS[36,93,94], DEFORM[9,49,95,96], FORGE[10,97] and ELFEN[33]. ABAQUS allows the user to have a fine control over the model, which has to be built "from scratch". Users can configure specific material properties, meshing strategies, element types and high level details can be implemented within the models. ABAQUS is considered as a robust tool[98] offering scripting capabilities (Fortran 90 and Python).

Flow modelling approaches

Using numerical modelling, authors in the literature have attempted to model the complex mechanical mixing of LFW at the weld interface between the two parts. Unlike most of the other friction welding processes[99–104], models in the literature are fully-coupled models. For example, most of the models simulating inertia friction welding do not model the rotational motion of the process[26].

As detailed by McAndrew et al.[7], three flow modelling approaches have been applied to LFW in the literature. The first approach developed by Vairis et al.[33] used a deformable body oscillated against a rigid body, see Figure 2-21 a). Computational time is reduced with this approach however a temperature

dependant friction coefficient needs to be defined to account for the heat generation. Furthermore, the mechanical mixing occurring at the interface to form the joint cannot be modelled since only one body is deformable. Similar to the first approach, the second involves two deformable bodies rubbed against each other, as presented Figure 2-21 b). Despite the use of two deformable bodies rather than one, the mechanical mixing is still not representative of the real process since the two interfaces do not merge. Turner et al.[10] solved the problem by considering a single body, conceptually representing the two original parts, where a thermal profile accounting for the initial phases has been mapped, allowing the material at the centre to deform during the oscillations (see Figure 2-21 c)). Using this approach Schroeder et al.[9] and McAndrew et al.[7] successfully modelled the flash morphology for several welding conditions. A comparison of flash morphologies for low, medium and high energy input rates obtained experimentally and numerically by Schroeder et al.[9] is presented in Figure 2-22. The energy input rate was calculated using the equation defined by[9]:

$$Energy\ input\ rate = 4 * \mu * f * P * A \qquad 2\text{-}7$$

where μ is the friction coefficient, f the frequency, P the applied force and A the amplitude. The exact values of frequency, amplitude and applied pressure are not disclosed by Schroeder et al.[9].

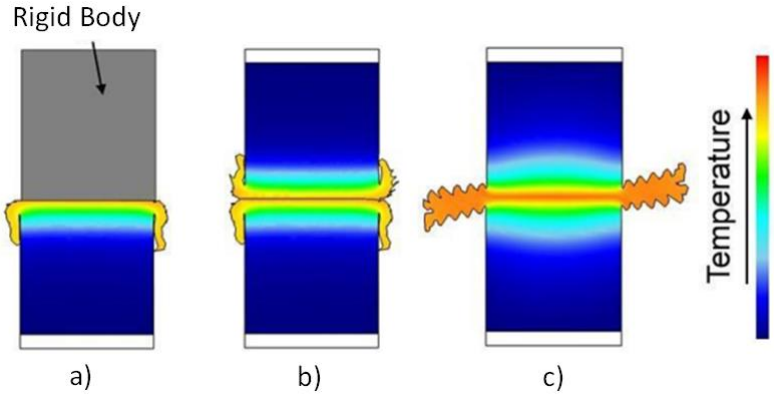

Figure 2-21: Flow modelling approaches: a) rigid body approach, b) two single bodies approach and c) single body approach[7]

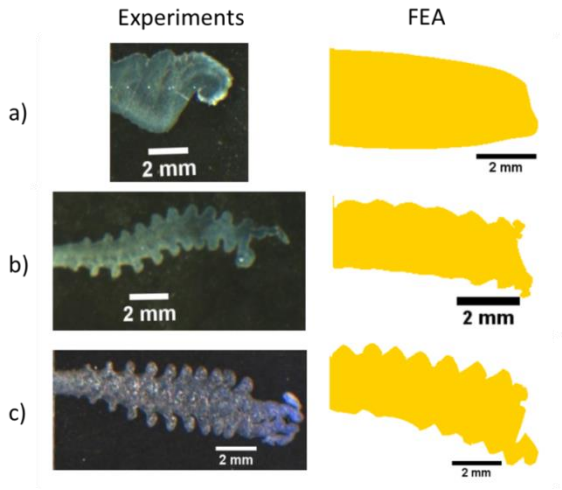

Figure 2-22: Experimental and numerically predicted flash morphologies for different welding conditions[9], a) low, b) medium and c) high energy input rate

Heat generation approaches

The literature presents two different approaches to account for the heat generated during the welding phases.

The first method uses a temperature dependent friction coefficient[5,12,33,36,37,95] with a fully-coupled model to generate the heat during all the welding phases. As pointed out by Blau[105], the number of factors which potentially influence the friction coefficient is large and includes among others: contact geometry, fluid and flow properties, relative motion, applied forces, temperature and stiffness and vibrations. As a consequence, one needs to apply extra care while using friction coefficient values.

The second method[7,8,11,49,106] post-processes the machine data recorded during welding to access the average heat flux over the conditioning phases. The heat flux is applied to a thermal model to predict the conditioning temperature distribution. Its retrospective nature offers a greater accuracy in terms of temperature prediction by being as close as possible to the experimental values; however it is also its main limitation. Once the conditioning phase temperature has been predicted, the single-body method previously defined (see Figure 2-21 c)) is used to model the equilibrium phase, where a plastic heat fraction is specified, typically in the range of 90 to 100%[8,10].

It is worth mentioning that Turner et al.[10] showed a certain insensitivity of the equilibrium temperature distribution regarding the conditioning temperature field used. To the best knowledge of the author, all the models presented in the literature which model the equilibrium phase include the burn-off and use a fully-coupled thermal-stress analysis. A fully-coupled thermal-stress analysis is required by the two approaches, previously described, since the thermal analysis is dependent on the stress solution. For the first approach, the mechanical energy dissipated by friction is converted into heat. For the second approach, a fraction of mechanical energy used to plasticise the material is converted into heat while the remainder of the energy is associated with phase transformations, changes in grain boundary generation and migration and stored in the form of crystalline defects[37,106].

Meshing

A fine mesh is used at the weld interface and its vicinity to capture the high deformations happening and it is coarsened further back where little deformation occurs. At the weld interface, mesh element lengths are found between 0.08 mm to 0.6 mm[7–9,13,34,36,52,96].

Triangular elements for 2D models[10,13,32,33] or tetrahedrons in 3D are often used since automated meshing can be done more easily. However, quadrilateral elements in 2D (hexahedrons in 3D) tend to be used at the weld interface[7,8,36,37,95] for more accuracy and for computational time reduction since more triangles are required than quadrilateral to cover the same mesh, at equivalent element length[16].

Properties of Ti-6Al-4V

Material properties play a key role in the accuracy of the predictions made by a numerical model[52] and since large temperature gradients are created during welding, it is important to consider them over an appropriate range of temperature. The material considered in this research is Ti-6Al-4V which is commonly considered as isotropic[37,88,107,108]. During LFW, the fusion temperature of Ti-6Al-4V is not reached therefore no fusion/solidification phase

transformation needs to be considered. This section describes the main material properties necessary to compute a thermal and mechanical analysis aiming to model the LFW process.

Thermal properties:

Heat transfer occurs following one of these three mechanisms: conduction, convection or radiation. In welding heat losses from convection and radiation are usually negligible, making conduction the primary transfer mechanism[109]. However with LFW, important convective heat losses occur due to the flash formation.

The thermal conductivity measures how easily heat flows within the material. Figure 2-23 displays thermal conductivity values from different sources where the thermal conductivity is shown to increase with the temperature. The thermal conductivity of Ti-6Al-4V is relatively low compared to other materials, making Ti-6Al-4V particularly suited to LFW since the heat will stay confined to the weld interface, allowing the interface temperature to rise rapidly[5,8,11,12,21,50,56].

The specific heat capacity is the amount of energy required to raise a unit mass of material by 1ºC. Specific heat capacity values from several sources are presented in Figure 2-24. Noticeable differences in specific heat capacity values arise above 800ºC. As stated by Boivineau et al.[110], the specific heat capacity is strongly affected by the thermal history of the material measured and the accuracy of the measurement method used. Also differences between data from Li et al.[5] and from Mills et al.[111] compared to the other sources could be a consequence of not having included the phase change effects in the specific heat capacity. Indeed, one could account separately for phase changes by defining a latent heat.

Overall, data from DEFORM's standard library are believed to be the most representative since they are near the average of the values presented in the literature and the values are available over an acceptable range of temperature.

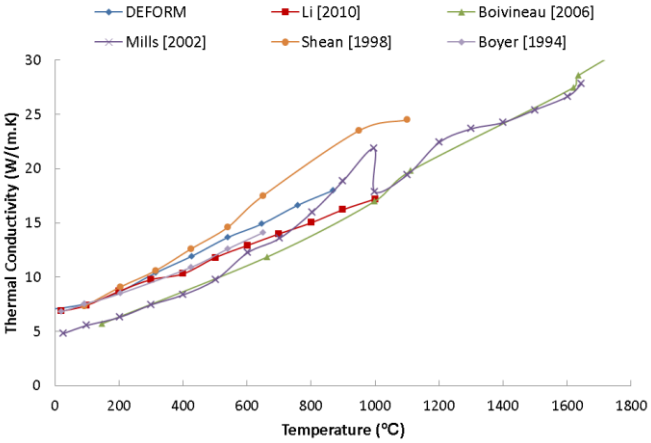

Figure 2-23: Comparison of Ti-6Al-4V thermal conductivity from different sources (DEFORM's standard library, Li et al.[5], Boivineau et al.[110], Mills[111], Shean et al.[112] and Boyer et al.[88])

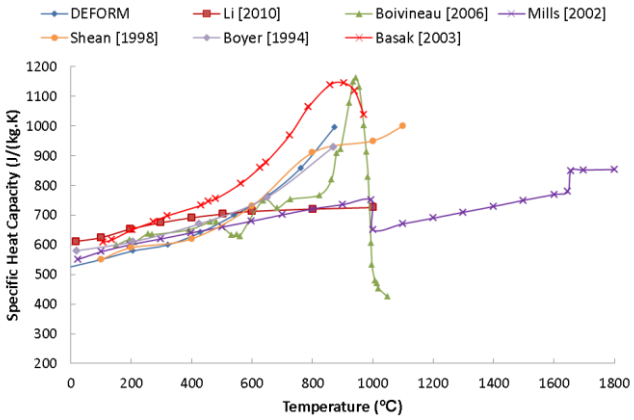

Figure 2-24: Comparison of Ti-6Al-4V specific heat capacity from different sources (DEFORM's standard library, Li et al.[5], Boivineau et al.[110], Mills[111], Shean et al.[112], Boyer et al.[88] and Basak et al.[113])

Mechanical properties:

Similar to its thermal counterpart, a mechanical analysis requires multiple material properties to model the thermal, elastic and plastic deformations occurring during LFW.

The linear thermal expansion coefficient describes the dimensional change of a material in one direction with rising or falling temperature. Little variations with the temperature are shown by the different sources of linear expansion coefficients of Ti-6Al-4V, see Figure 2-25.

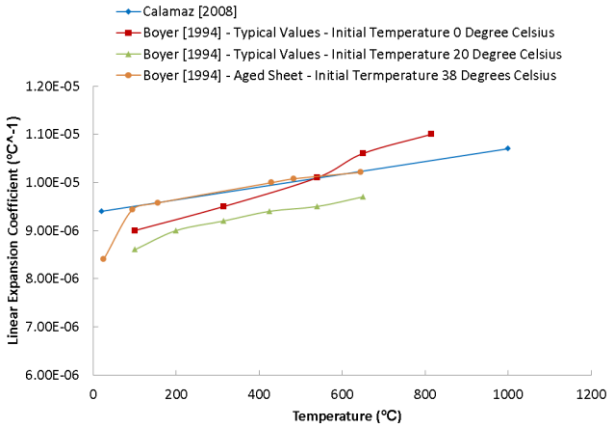

Figure 2-25: Comparison of Ti-6Al-4V linear expansion coefficients from different sources (Calamaz al.[97] and Boyer et al.[88])

Stresses are calculated by all models from elastic strains using Hooke's law. The elastic properties required are the Young's modulus and Poisson's ratio, respectively E and v, see Figure 2-26 for values from different sources. Young's modulus data from Turner et al.[13] and Boyer et al.[88] exhibit a good agreement. Data recorded by Peters et al.[62] show a steep drop in the magnitude of the Young's modulus above the temperature 500ºC. As mentioned by Peters et al.[62], mechanical properties are strongly influenced by the type of microstructure present in the material, i.e. fully lamellar, fully equiaxed or bi-modal.

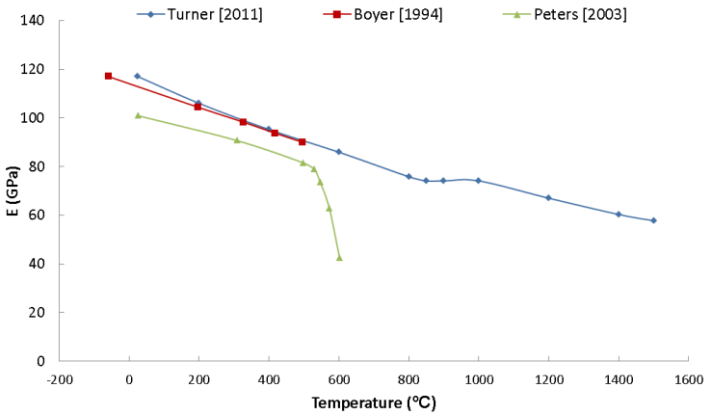

Figure 2-26: Comparison of Ti-6Al-4V Young's modulus values from different sources (Turner et al.[13], Boyer et al.[88] and Peters et al.[62])

The last material property required is the flow stress which represents the evolution of the stress against the strain at different temperatures. Obtaining

experimental flow stress data over a large range of temperatures is a difficult task, therefore many sources available in the literature usually display data over a limited range of experimental conditions. Typically, two approaches in numerical modelling are used to account for the flow stress of a material, either using a flow stress model such as the Johnson-Cook law[5,37,97] or using experimental tabular data[7,10,12], with both approaches accounting for strain-rate hardening effects. Tabular data are usually recognised as the most accurate[52].

As previously explained; some numerical models convert into heat the mechanical energy used to plasticise the material, therefore flow stress data at high strains and at high strain-rates are necessary. However, in this thesis the generated heat during welding is calculated separately and the prediction of residual stresses is of interest. Although high strain-rate[106] up to 2500 s^{-1} are reached during welding, residual stresses are believed to be created during cooling as a consequence of having a steep thermal gradient across the weld and therefore, flow stress data at low strains and low strain-rates, capturing the hardening behaviour of the material, are required. For example, for a 1000 ºC variation of the weld interface temperature during a 15 seconds cooling with a linear expansion coefficient of 1E-05 $ºC^{-1}$, a strain-rate of about 6E-04 s^{-1} will be expected. Consequently, the thesis focuses on quasi-static flow stress data which are presented in Figure 2-27 a) and b).

All the different sources on Figure 2-27 a) displays a decrease of the stress required to initiate the plasticisation of the material when the temperature increases. When the temperature increases, the material softens and as a result less mechanical energy is necessary to plasticise the material. Figure 2-27 a) records differences in flow stress values between authors. Flow stress data is influenced by the initial microstructure of the Ti-6Al-4V alloy used (i.e. fully lamellar, fully equiaxed or bi-modal). The method used to gather the experimental data is also likely to affect the flow stress data. Turner obtained the flow stress curves using the software JMatPro, while Chen, Seshacharyulu and Wang obtained their data by conducting experiments. Guo does not disclose the origin of the experimental data used in his work. Finally, the

different strain-rates used by the sources will also participate to the discrepancies observed in Figure 2-27 a).

A large drop in the stress value is recorded between 700ºC to 800ºC, see Figure 2-27 b). In this temperature range, the material begins to transform from an alpha-beta microstructure to single phase beta microstructure[114]. The beta microstructure is a body-centered cubic (BCC) which possesses 12 slip systems compared to 3 slip systems for the HCP structure of the alpha phase[62]. Although HCP has a higher packing density of atoms within its slip planes compared to the BCC lattice, which eases the gliding of the dislocations, HCP possesses a longer minimal slip path which increases the stress required to initiate plastic deformation[62]. As a consequence, the combination of high temperatures and increase in the volume fraction of beta phase results in the drop in the stress displayed on Figure 2-27 a) and b). It is worth noting that due to the lack of flow stress data available in the literature, between 700ºC and 800ºC, part of the work-hardening behaviour of Ti-6Al-4V is lost, which might influence subsequent residual stress calculation.

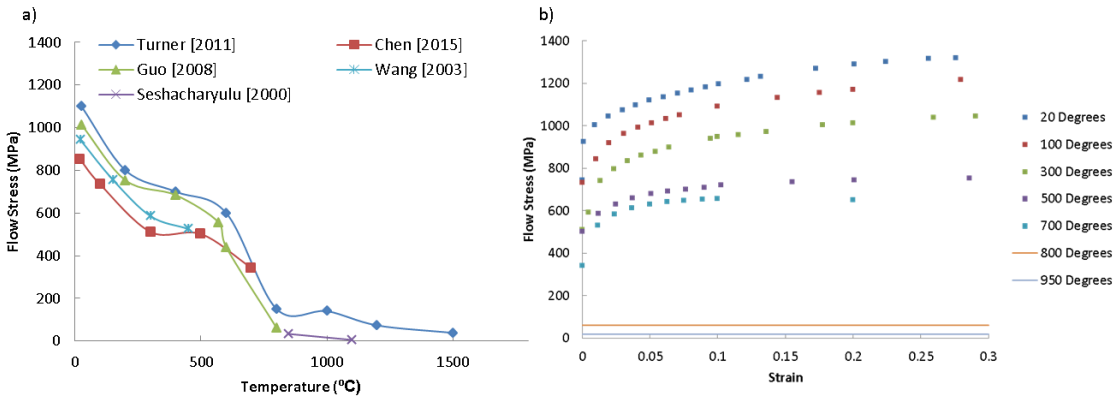

Figure 2-27: a) Comparison of Ti-6Al-4V flow stress data against temperature at first yield from different sources (Turner et al.[13] (strain-rate of 0.001 $\mathbf{s^{-1}}$), Chen et al.[115] (strain-rate of 0.01 $\mathbf{s^{-1}}$), Guo et al.[116] (strain-rate of 3.33*$\mathbf{10^{-5}s^{-1}}$), Wang et al.[117] (strain-rate of 6.6*$\mathbf{10^{-3}s^{-1}}$) and Seshacharyulu et al.[114] (strain-rate of 3*$\mathbf{10^{-4}s^{-1}}$)) and b) Ti-6Al-4V flow stress curves against strain, temperatures inferior and equal to 700ºC are taken from Chen et al.[115] at a strain-rate of 0.01 $\mathbf{s^{-1}}$. At 800ºC (strain-rate of 3.33*$\mathbf{10^{-5}}$ $\mathbf{s^{-1}}$) and 950 ºC (strain-rate of 0.001 $\mathbf{s^{-1}}$), flow stress curves are from Guo et al.[116].

2.5.3 Residual stress modelling in linear friction welding

Three authors in the literature developed a numerical model able to predict residual stresses within Ti-6Al-4V LFW structures, Turner et al.[13], Nikiforov et al.[93] and Fu et al.[14].

Turner et al.[13] conducted a fully coupled thermo-mechanical analysis using the single body modelling approach he developed (previously detailed in the section "Flow modelling approaches") while applying a plane-strain condition to his 2D model. Oscillations of the equilibrium phase were simulated and plastic heat produced to predict equilibrium temperature and stress fields before cooling the structure to ambient temperature and predicting the residual stress field. A 3D model was not considered since it would have led to a prohibitively large computational time. Turner's FEA model replicated numerically the welding conditions investigated by Romero et al.[50] who conducted synchrotron X-ray diffraction experiments. Figure 2-28 a) shows that numerically, a larger band of residual stress is predicted compared to experiments. It is difficult to judge if the peak value is correctly predicted by the FEA model due to the lack of experimental data at the weld interface and its vicinity. Overall, there is a qualitative agreement between experiments and simulations.

Nikiforov et al.[93] developed a numerical approach focused on the forging stage of the welding process. Nikiforov started his analysis by applying a forging pressure onto the 3D numerical model which was maintained at the ambient temperature. Then a temperature field previously predicted using a 1D analytical model (constant thermal properties were used) was mapped onto the model. Finally, maintaining the temperature field, the forging pressure was removed before cooling down the part and predicting the residual stress field. Despite applying a forging pressure of about 100 MPa, Nikiforov's model does not display any compressive stress above 23 MPa during the first phase of his analysis (i.e. when the ambient temperature is maintained). The reason for this discrepancy is unclear. Nikiforov experimentally calculated average values of residual stresses across the interface by measuring the interface dimensions before and after cutting the weld along its cross section. Estimations of the

internal forces as a function of elastic material properties and weld cross section dimensions are used to retrieve the residual stresses values. Overall, Nikiforov's numerical model tends to under-predict the residual stresses compared to the experimental values.

Fu et al.[14] also omitted the friction phases and computed a coupled thermo-mechanical analysis on a 3D model in three steps. An initial temperature field using a Gaussian distribution, representing the equilibrium temperature field is mapped onto the model, assuming a stress-free state. During the first step, the model is clamped and a forging pressure is applied for 10 s then released. The model cools for 100 s without forging pressure (second step) and finally during third step, the model is brought to room temperature before releasing the clamp to predict the final residual stress field. Fu et al.[14] replicated numerically the LFW geometry used by Frankel et al.[45] and compared his predictions against Frankel's experimental measurements of residual stress. Results from his numerical model tend to under-predict the residual stress peak of magnitude as well as predicting noticeably larger bands of tensile residual stress compared to those recorded by Frankel et al.[45].

Turner et al.[13] drew several important conclusions from his numerical analysis work. Firstly, he noticed that stresses created by the oscillations tend to disappear once the oscillations have ceased, implying that oscillations have a minimal impact on the stress field during welding. Secondly, the magnitude of the stresses developed during welding are significantly lower than those arising during cooling. Consequently, Turner concluded that the residual stress field is primarily driven by the cooling of the part after welding. Numerically a peak of residual stress is recorded by Nikiforov et al.[93] at 330 MPa which is noticeably lower than the residual stresses predicted by Turner et al.[13] which is above 900 MPa while Fu et al.[14] predicted a maximum of 500 MPa. The variance may be explained by the use of different welding conditions which are not disclosed by the authors and different material properties. Also the equilibrium temperature distributions used by Nikiforov and Fu were not validated experimentally unlike Turner who validated the temperature histories predicted by his model against

thermocouples[10]. Turner et al.[13] varied the applied pressure and studied its effect on the residual stress field, results are displayed in Figure 2-28 b). Only a large variation of applied pressure resulted in a decrease of the residual stress magnitude, bringing Turner et al. [13] to the conclusion that the applied pressure has only a minimal influence on the residual stress field. Similarly, Nikiforov et al.[93] and Fu et al.[14] recorded a decrease of the residual stress magnitude with large variations of applied pressure. Fu et al[14] conducted an interesting study where he varied the temperature distribution (see Figure 2-29 a)) while maintaining the peak temperature constant. As a result, increasing the temperature gradient of the profile increased the residual stresses, as shown Figure 2-29 b).

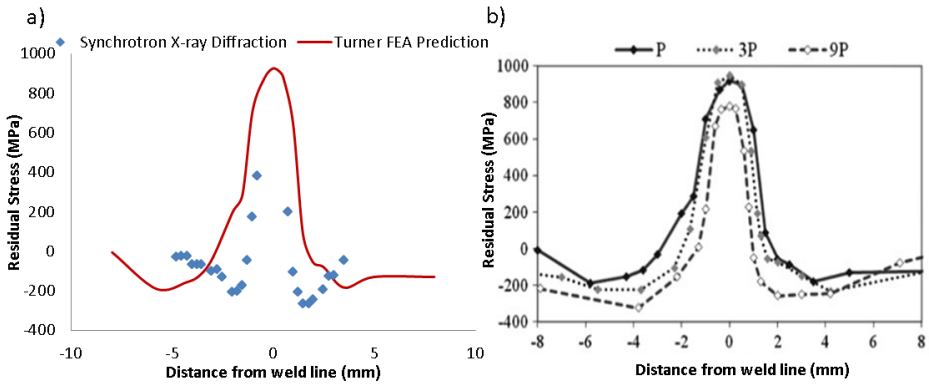

Figure 2-28: a) Comparison of the residual stress profile developed in the longest direction of the weld interface, predicted numerically by Turner et al.[13] and measured by Romero et al.[50] using synchrotron X-ray diffraction and b) variation of numerically predicted residual stresses with the applied pressure from Turner et al.[13]

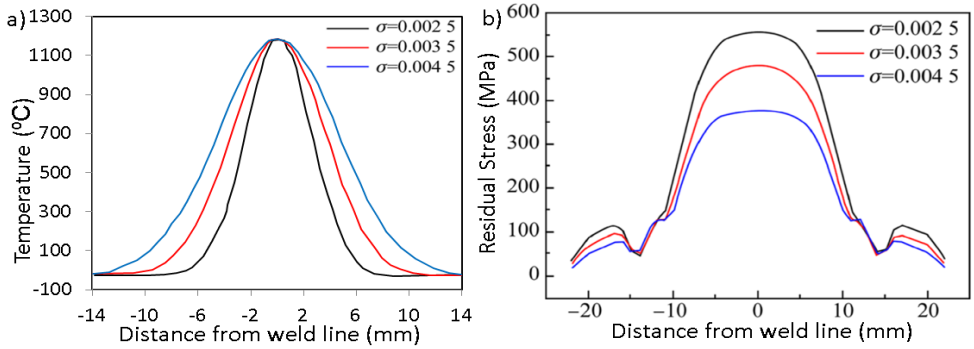

Figure 2-29: a) Gaussian distributions of the equilibrium temperature profile and b) the associated residual stress profiles predicted by Fu et al.[14]

2.6 Conclusions

The interest in LFW is increasing with industrial companies trying to extend the use of LFW outside the traditional application of blisk manufacturing. In order to increase the number of LFW applications, a more fundamental understanding of the process is necessary.

Numerous LFW numerical models are available in the literature; however these models have been developed to replicate the welding process by including the oscillation of the workpieces. These models typically focus on the prediction of temperature histories, material deformation, flash formation and expulsion of interface contaminants and mostly do not investigate the stress field during or after welding.

Because modelling the oscillations is seen as a requirement to obtain the temperature field during the equilibrium phase, most of the models have been confined to a 2D geometry to limit the computational time required. As a consequence, complex geometry cases such as keystone or bladed-disk welds are rarely considered.

Residual stresses can affect the structural integrity and are therefore an essential consideration for end users. Measurements of residual stress are difficult particularly for the titanium alloys which are the main application; therefore numerical simulations are seen as a practical alternative. Owing to the computational constraints inherent to the modelling approaches available in the literature, very few publications on modelling residual stress development within LFW structures are published. More work on understanding the effect of the process parameters on the residual stress development is needed.

To summarise, gaps in knowledge include:

- A modelling approach non-computationally prohibitive able to predict residual stresses in real engineering structures.
- An understanding of the fundamental features required in a model for the residual stress prediction.

- A clear understanding of how process parameters affect the residual stress.

This thesis aims to develop a LFW computationally efficient numerical approach focus on the residual stress prediction in real engineering components. In order to address the gaps in knowledge, the objectives of this thesis have been defined as follows:

- Develop a new computationally efficient modelling approach which will allow the modelling of 3D LFW structures by bypassing the modelling of the oscillations. Thermal and mechanical predictions will be validated against experimental data.
- Provide better understanding of the residual stress development and how it is affected by parameters such as applied pressure, clamping pressure, rubbing velocity, oscillation direction, weld interface geometry and equilibrium temperature field.
- Application of this methodology to real engineering components

Chapter 3: Development of a 3D LFW thermal model and effects of process parameters

This chapter is an edited version of the following article:

Bühr, C., Colegrove, P. A. & McAndrew, A. R. A computationally efficient thermal modelling approach of the linear friction welding process J. Mater. Process. Technol. (2017). doi:10.1016/j.jmatprotec.2017.09.013

3.1 Background

As shown in the literature review, getting an insight into LFW using experimental methods alone is difficult due to its rapid nature. Therefore many researchers developed numerical models to better understand the process [6,7,36,117]. Much of the modelling work to date involves modelling the oscillations to account for the heat generation as well as the flash formation [6,8,10,36]. These fully-coupled models are computationally expensive due to the complex thermo-mechanical behaviour happening at the weld interface. Turner et al. [13] suggested that the residual stresses arise primarily as a consequence of the cooling. As such, there is a need to develop a numerical model that avoids the dynamic oscillations while predicting realistic thermal and stress fields. This will dramatically reduce the computational time and facilitate further research on residual stress formation within LFW components. The aim of this chapter is to develop the thermal part of such a model for the LFW of Ti-6Al-4V.

3.2 Methodology

3.2.1 Experiments

Ti-6Al-4V linear friction welds were made in collaboration with TWI Cambridge using the Thompson E20 machine, see Figure 3-1, for the five intended welding parameters listed in Table 3-1. The author prepared the samples and placed the thermocouples, however the machine was operated by a TWI engineer. As shown in Table 3-1, some of the welding parameters were replicated to account

for experimental variability. These welding parameters cover most of the operating window of frequency, amplitude and applied force of the LFW machine used. The experiments used workpieces measuring 20 x 40 x 60 mm, which is illustrated in Figure 3-2. The Ti-6Al-4V parent material had a bimodal alpha-beta microstructure. Experimentally the workpiece was oscillated in the *x* direction (along the interface dimension 40 mm), except for weld 5 where it was oscillated transverse to this. Thermal histories were recorded during the welding process using k-type thermocouples. EDM was used to produce the holes shown in Figure 3-3 a). The thermocouples were inserted by the author, at depths of 0.3 mm, 1.2 mm, 2.7 mm, 4.2 mm and 5.2 mm from the weld interface and an epoxy resin was used to fix them in place. To get the thermocouple wires out of the clamping tool, a groove was machined on one workpiece, as shown in Figure 3-3 b).

The influence of the rubbing velocity was studied in the results section by comparing welds 1, 2 and 4. The average rubbing velocity, represents the average absolute velocity of the oscillating workpiece over a cycle, and is determined from the frequency, *f* and amplitude, *A* (Addison [44]) with:

$$v_r = 4Af \qquad 3\text{-}1$$

The effect of the applied force is examined using welds 3 and 4, while the oscillation direction is studied using welds 4 and 5.

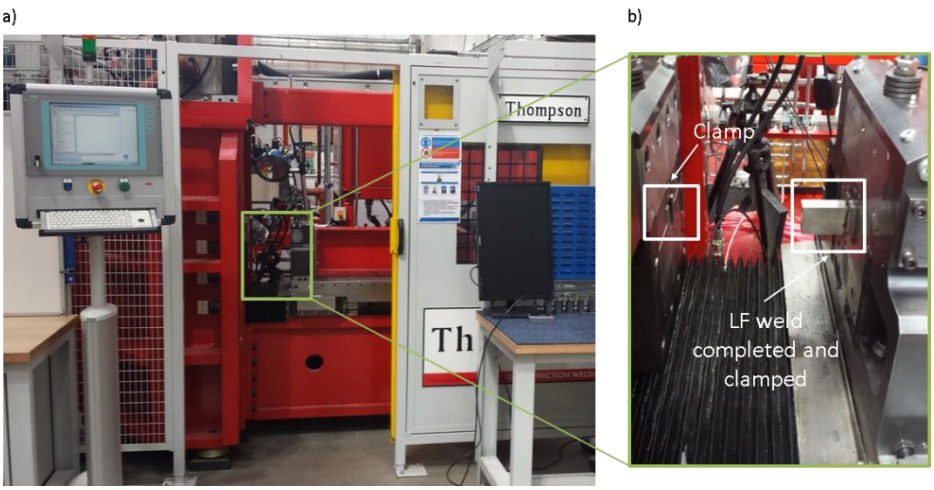

Figure 3-1: a) Thompson E20 LFW machine used at TWI and b) zoom on a linear friction weld completed

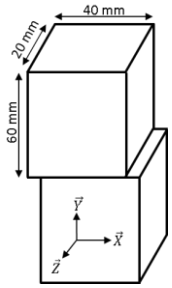

Figure 3-2: Workpiece dimensions and axes

Table 3-1: Welding parameters

Weld	Freq. (Hz)	Amp. (mm)	Applied Pressure (MPa)	Burn-off (mm)	Average Rubbing Velocity (mm/s)	Interface Dimension in Oscillation Direction:
1	20	1.5	90	3	120	40 mm
2;6	30	2	90	3	240	40 mm
3	50	2.7	40	3	540	40 mm
4;7;8	50	2.7	90	3	540	40 mm
5	50	2.7	90	3	540	20 mm

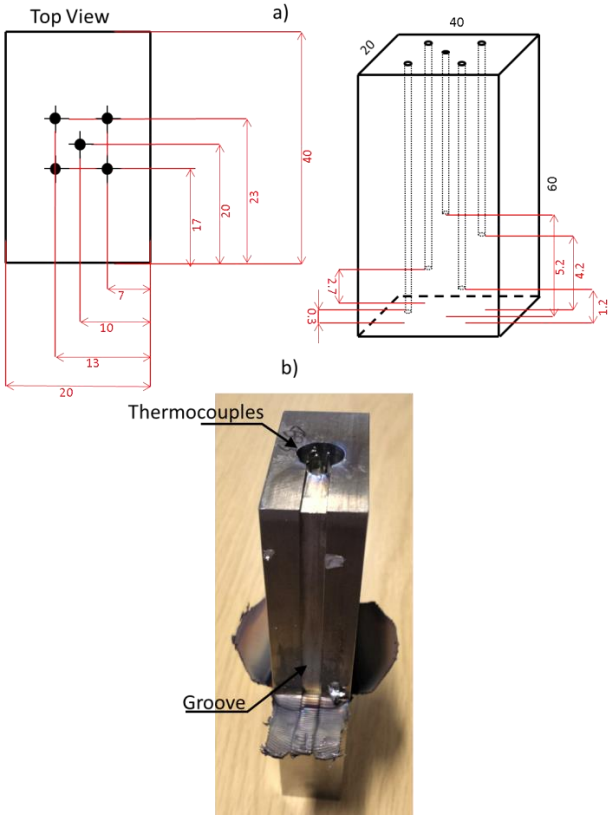

Figure 3-3: a) Positioning of the thermocouples and b) experimental sample showing the hole where the thermocouples were fitted and the groove

During linear friction welding, several parameters were monitored with high-speed data acquisition systems including the oscillator position x, the in-plane force F_{in}, the axial position representing the burn-off and the applied force F_a applied on the non-oscillating workpiece, as shown in Figure 3-4.

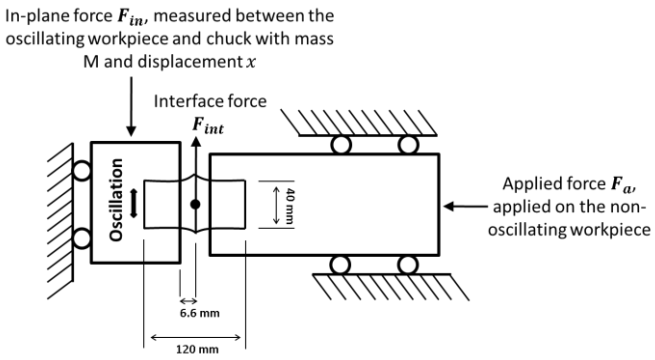

Figure 3-4: Schematic illustration of the linear friction machine

To calculate a realistic heat flux, the sampling rate of the machine data needs to be sufficiently high to capture the waveform. Two in-plane force signals during phase 3 are displayed in Figure 3-5 with signals 1 and 2 having the same sampling rate of 500 Hz however different welding frequencies, 30 Hz for signal 1 and 50 Hz for signal 2. Signals 1 and 2 exhibit periodic behaviours where maxima of the oscillations are perfectly recorded. Therefore, a sampling rate 10 times greater than the frequency of the machine is found adequate to capture the waveform of the in-plane force signal.

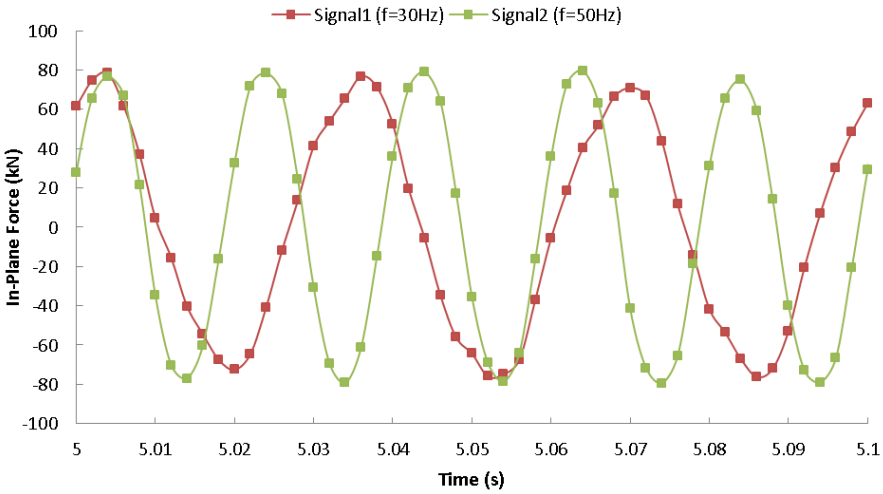

Figure 3-5: Two in-plane force signals for welds at two frequencies

A similar approach to that developed by Ofem et al. [4] and reemployed by McAndrew [8,11] was used for analysing the data. The machine data obtained during welding was post-processed and the average power (Watt) per phase (i.e during phase 1: initial phase or phase 2: transition phase or phase 3: equilibrium phase) was calculated with the following formula:

$$\dot{\boldsymbol{Q}}_{\boldsymbol{Phase}} = \frac{\int_{\mathbf{0}}^{\boldsymbol{t_{Phase}}} \boldsymbol{F_{int}} \boldsymbol{v} \boldsymbol{dt}}{\boldsymbol{t_{Phase}}} \qquad 3\text{-}2$$

where t_{Phase} is the duration of the phase being considered, F_{int} the force at the weld interface and v the instantaneous velocity of the oscillating workpiece. An example of calculated average power values per phase over the power history of a LFW is given in Figure 3-6 a).

The velocity v can be calculated using a finite difference method such as the central difference scheme:

$$v(t) = \frac{x(t + \Delta t) - x(t - \Delta t)}{2\Delta t} \qquad 3\text{-}3$$

where t is the time and x the displacement.

Since $\boldsymbol{F_{int}}$ cannot be directly recorded, it is necessary to express it as a combination of known parameters. Applying Newton's second law, projected on the vertical axis (see Figure 3-4), $\boldsymbol{F_{int}}$ can be decomposed as follow:

$$F_{int} = F_{in} - M.a \qquad 3\text{-}4$$

where $\boldsymbol{M}$ is the combined mass of the oscillating chuck and workpiece (approximately 280 kg) and $\boldsymbol{a}$ its acceleration. A sinusoidal displacement of the oscillating workpiece is used in the experiments therefore the acceleration can be calculated as follow:

$$a = \frac{d^2x}{d^2t} = \frac{d^2(Asin(\omega t))}{d^2t} = -\omega^2\big(Asin(\omega t)\big) = -\omega^2 x \qquad 3\text{-}5$$

where ω is the angular frequency.

An alternative method of calculating the acceleration is by numerically differentiating the displacement in a similar manner as for the velocity. However,

this method is subject to a large amount of noise, as shown by Ofem et al.[4], which is why equation 3-5 was used. An example of F_{int} and F_{in} histories is presented in Figure 3-6 b). It can be noted that before contact between the two workpieces (i.e. prior phase 1), when the interface force is known to be nil, the F_{int} signal approaches but does not equal zero. The non-zero values are believed to be a joint consequence of assuming a sinusoidal displacement and machine output accuracy.

Using the machine data for the five different sets of welding parameters in Table 3-1, five models were built.

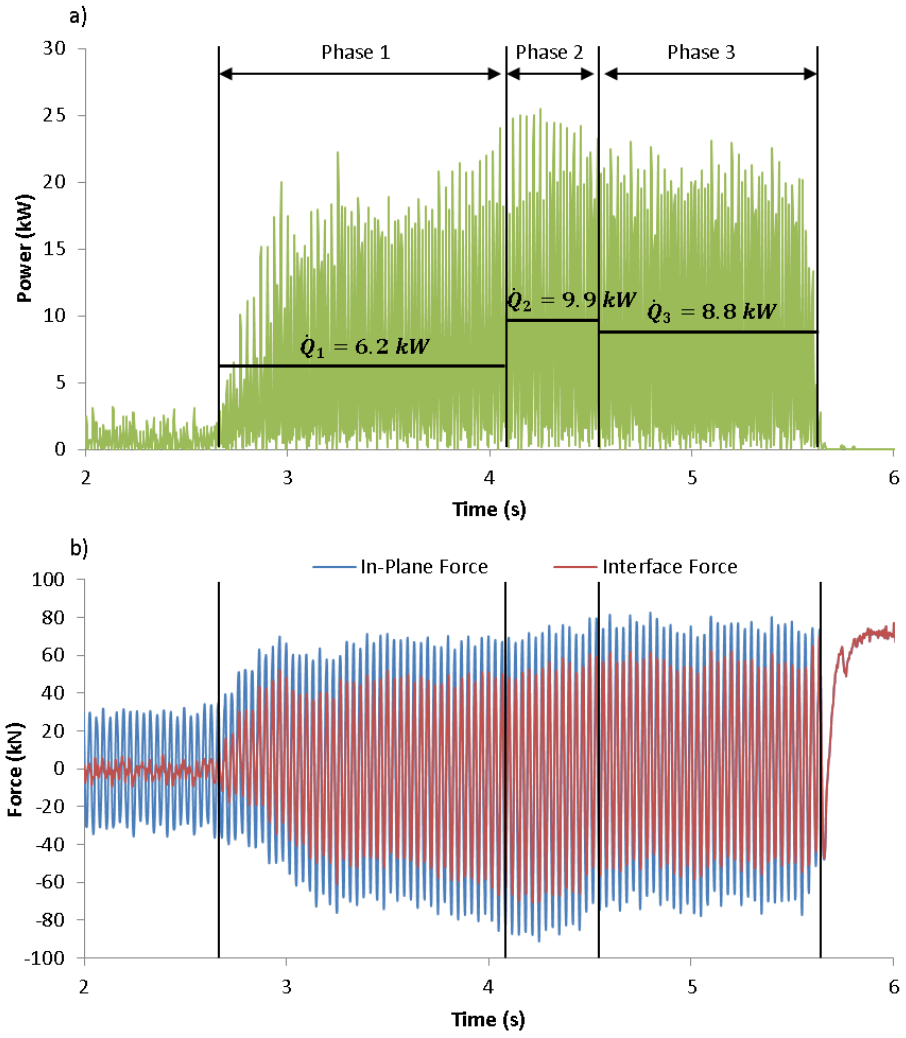

Figure 3-6: a) Power history of a LFW with average power values per phase and b) its in-plane and interface force histories

3.2.2 Modelling approach

To avoid modelling the oscillations an accurate heat flux must be applied to the weld region and elements iteratively removed from the interface to account for the burn-off. The following sections describe the four key areas of the transient heat transfer analysis conducted in this chapter.

3.2.2.1 Mesh and material properties

As shown in Figure 3-2 the real workpieces are 20x40x120 mm. Since the deformation and heat flow are approximately symmetric around the planes (P1), (P2) and (P3)[7,8,33], see Figure 3-7 a), only an eighth of the geometry was included. Therefore, a workpiece measuring 10x20x60 mm was modelled using the FEA software ABAQUS, see Figure 3-7 b).

The mesh is composed of eight-node linear heat transfer bricks. Fine elements are needed at the weld interface and its vicinity to ensure that steep thermal gradients are captured by the numerical model. To determine the level of discretisation needed, a mesh sensitivity study was conducted on weld 4 (welding conditions presented in Table 3-1), see Table 3-2. The mesh element lengths displayed in Table 3-2 refer to a band of material located within 6.6mm back from the weld interface. Further away from this, the mesh is coarsened to 1 mm. The predictions of the peak temperature in Table 3-2 indicate that a minimum size of 0.3 mm is required within the 6.6 mm band to capture an accurate thermal profile. Ti-6Al-4V temperature dependent specific heat and conductivity from the DEFORM's software library are used in the model (See Appendix A).

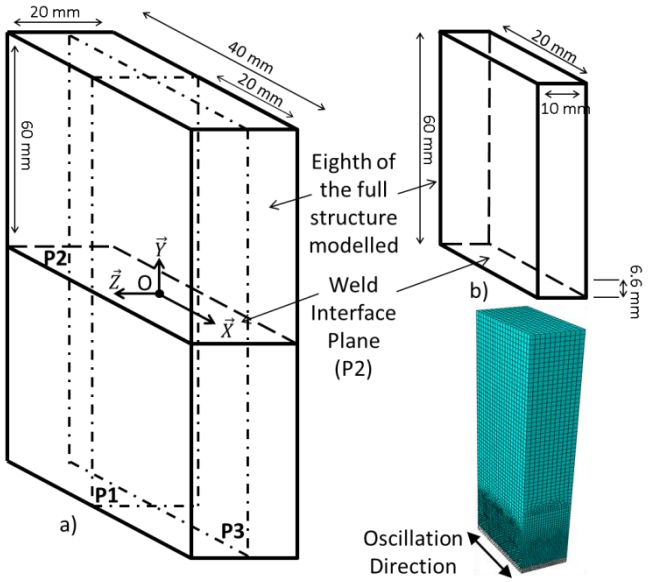

Figure 3-7: a) Schematic diagram of the full LFW structure with its planes of symmetry, P1, P2 and P3 and b) geometry showing how only an eighth of the sample was modelled with the corresponding mesh

Table 3-2: Mesh sensitivity results

Mesh Element Length (mm)	Total Number of Elements	Interface Temperature Prior Cooling (°C)
0.7	31350	983
0.5	43313	986
0.3	98165	994
0.2	234417	994

3.2.2.2 Application of the heat flux and modelling of the burn-off

Since the oscillations are not modelled, it is necessary to find an alternative way to account for the heat generation. To do so, the average power for each phase was estimated by post-processing the machine data obtained when making a linear friction weld, as previously described. Therefore, constant values of powers are used to calculate the heat fluxes applied on the model but in reality, the power varies with time, as shown in Figure 3-6 a). In accordance with the literature, 100 % of the mechanical energy is assumed to be transformed into heat[10]. A uniform surface heat flux ($W.m^{-2}$) was applied on the weld interface during phase 1 and 2. Indeed, during phase 1 only dry friction occurs while phase 2 is a much shorter phase in comparison with phases 1 and 3, where a transition between dry to sticking friction occurs. Therefore, application of the

heat flux to the surface is a reasonable assumption for the first two phases. However, the heat is generated by the plastic deformation within the material during phase 3 over the TMAZ (thermo-mechanically affected zone), implying a volumetric generation of heat. A study of the influence of the phase 3 volumetric heat distribution is performed on welds 1 and 4 from Table 3-1, by considering three different heat distributions, shown in Figure 3-8. As for phases 1 and 2, a surface heat flux was considered for phase 3, as well as two volumetric heat distributions, one is distributed over half the TMAZ and the second one was distributed over the whole TMAZ. TMAZ thicknesses were calculated using an equation from McAndrew et al.[8] (see Appendix B). As will be proved in the results, a surface heat flux was shown to be adequate and was used for the subsequent modelling work. Heat losses by radiation, convection with air and conduction with tooling were ignored due to the short welding time and high thermal gradient encountered.

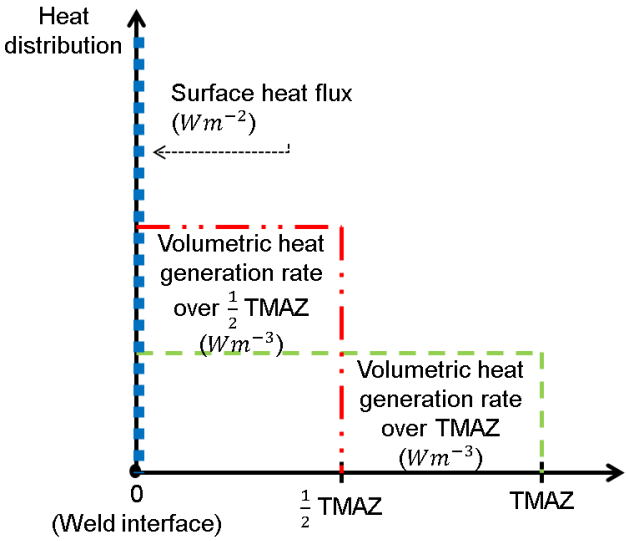

Figure 3-8: Three types of heat distributions investigated for phase 3

Modelling the burn-off during the process is important during phase 3 in particular, where it allows the temperature and the in-plane force distributions across the interface to reach a quasi-steady state. The burn-off is modelled in a step-wise approach where rows of elements are removed sequentially. Figure 3-9 illustrates this approach with the heat flux applied during step 1 then a row of elements is removed during step 2 and the heat flux is reapplied. At the end

of phase 2, the corresponding amount of burn-off (Bo Phase 2, shown in Figure 3-10) is removed from the model. However, during phase 3, the amount of burn-off (Bo Phase 3, see Figure 3-10) is removed in 10 steps at a pace which matches the experimental burn-off rate. Therefore, the time interval between layer removals is the thickness of the row of elements divided by the burn-off rate. The burn-off rate is calculated from the burn-off rate history and represents the slope of the burn-off as a function of time during phase 3 (dash line in Figure 3-10), where it is linear.

Note that the effect of the number of steps to remove the amount of burn-off happening during phase 3, on the thermal profile was investigated, where the material was removed in 1, 5, 10 and 20 steps.

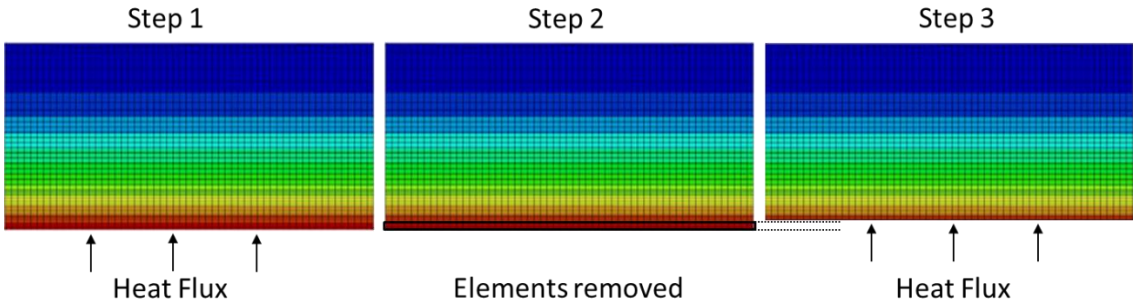

Figure 3-9: Step-wise removal approach

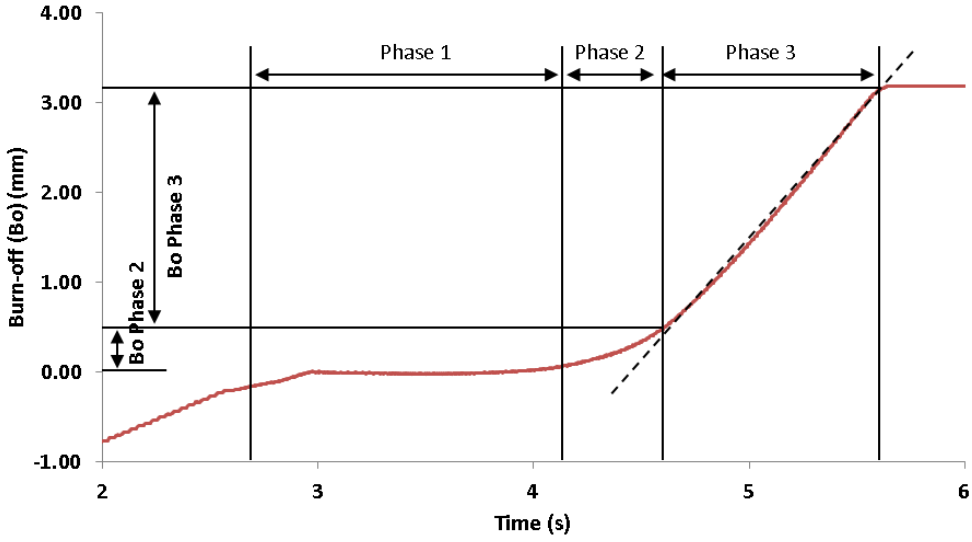

Figure 3-10: Burn-off history of a LFW where the slope of the dash line represents the burn-off rate

3.2.2.3 Additional data

The trend of the average phase 3 power and the weld interface temperature against the average phase 3 burn-off rate is analysed in the results section. In addition to the welds presented in Table 3-1, machine data from experimental trials conducted by McAndrew et al.[11], presented in Table 3-3, were post-processed and a simulation of each was created using the modelling approach presented in this chapter. The coupon dimensions used by McAndrew are the same as those used earlier, see Figure 3-2. Values of average phase 3 power and average phase 3 burn-off rate of the welds presented in Table 3-1 are given in Table 3-4. All the average phase 3 power, displayed in Table 3-3 and Table 3-4, were calculated using equation 3-2.

Table 3-3: Experimental conditions used by McAndrew et al.[11]

Weld	Freq. (Hz)	Amp. (mm)	Applied Pressure (MPa)	Burn-off (mm)	Average Phase 3 Power (kW)	Average Phase 3 Burn-off Rate (mm/s)
9	30	2	40	3	7.4	2.09
10	50	2.7	40	3	12	4.1
13	30	1	125	3	4.2	1.1
16	31.6	2.3	85.3	2.5	9.6	3.16
21	30	2	40	3	7.3	2
25	30	1	125	3	4.2	1.15

Table 3-4: Values of average phase 3 power and burn-off rate for the experimental conditions in Table 3-1

Weld	Average Phase 3 Power (kW)	Average Phase 3 Burn-off Rate (mm/s)
1	4.3	1.25
2	8.8	2.72
3	13	4.12
4	13	4.97
5	16	6.3
6	8.6	2.63
7	13	5.21
8	13	5.23

3.3 Results and discussion

3.3.1 Effects of the heat flux distribution and steps for element removal

Temperature profiles predicted at the end of phase 3 using the three heat flux distributions for the low rubbing velocity condition, weld 1, and the high rubbing velocity condition, weld 4, are displayed in Figure 3-11. The temperatures predicted are shown to be largely independent of the heat distribution with the greatest difference occurring at the weld interface. The volumetric heat distribution over the whole TMAZ resulted in a lower peak temperature. Moreover, the equation used to calculate the TMAZ thickness[8], which is based on results from FEA models, tends to over-predict their values compared to the experiments. Therefore having a larger predicted TMAZ, will enhance the small differences between thermal profiles predicted in Figure 3-11. Based on this study, a surface heat flux will be used for all subsequent modelling work since the size of the TMAZ is not required, simplifying the analysis.

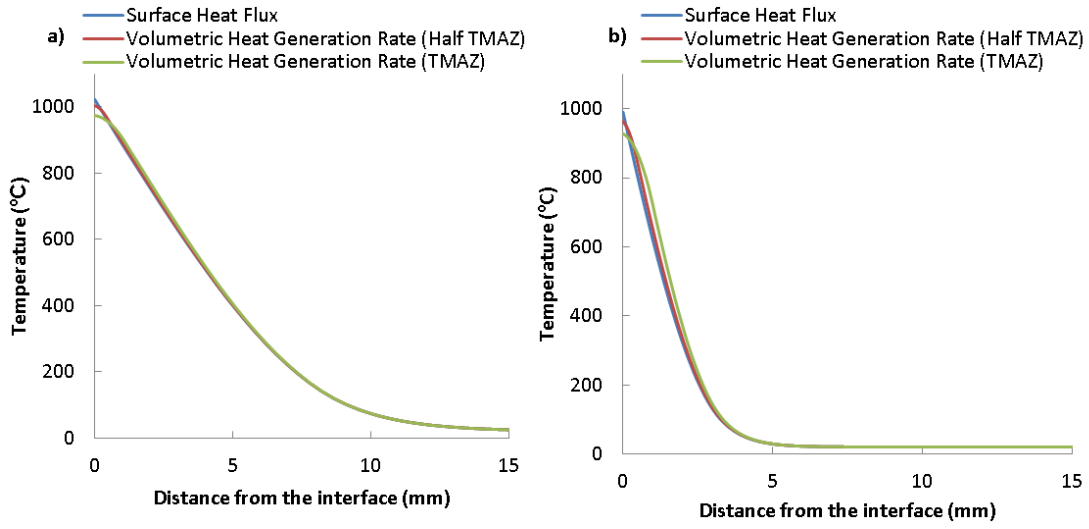

Figure 3-11: Comparison of the thermal profiles obtained at the end of phase 3 for different heat flux distributions: a) weld 1 (time elapsed: 8.14 s) and b) weld 4 (time elapsed: 1.36 s)

The influence of removing the burn-off of phase 3 in 1, 5, 10 and 20 steps on the final thermal profile, for welds 1 and 4 is displayed in Figure 3-12. The

number of steps has a greater effect for the high rubbing velocity weld 4 due to the steep thermal gradients created for this welding condition. It can be seen that deleting the 1.5 mm of burn-off in 1 step will under predict the interface temperature for both welds. Beyond 5 steps, all the thermal profiles converge toward the same distribution, so using 10 steps will be sufficiently large to have no impact on the temperature distribution.

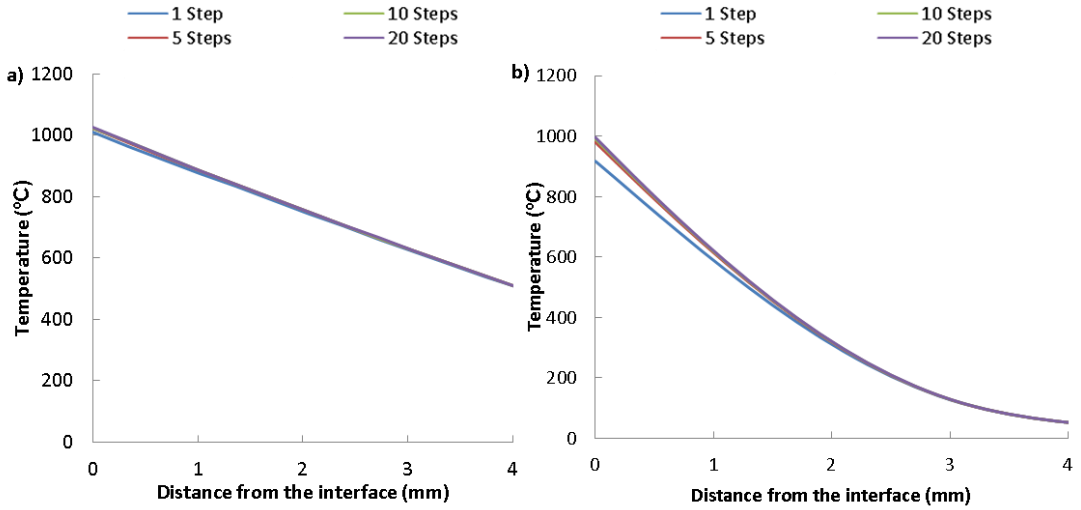

Figure 3-12: Influence of the number of steps to model the burn-off on temperature profile obtained at the end of phase 3 for: a) weld 1 (time elapsed: 8.14 s) and b) weld 4 (time elapsed: 1.36 s)

3.3.2 Effects of the LFW processing conditions

3.3.2.1 Influence of the rubbing velocity

Thermal histories experimentally recorded and predicted by the numerical model for three welding conditions are displayed in Figure 3-13. Despite the groove present to facilitate the passage of the wires, some of the thermocouples broke during welding. Consequently, some temperature histories are missing (i.e. 0.3 mm for weld 1 and 1.2 mm for weld 4; see Figure 3-13). Furthermore, once the thermocouples initially positioned 0.3 mm and 1.2 mm away from the weld interface, reached the interface during welding, they were destroyed by the process and consequently the data from these thermocouples was not usable. An applied pressure of 90 MPa is maintained for all the welds, while rubbing velocities of 120 $mm.s^{-1}$, 240 $mm.s^{-1}$ and 540 $mm.s^{-1}$ were

used for weld 1, weld 2 and weld 4. Figure 3-13 displays a reasonable agreement between experiments and simulations, demonstrating the ability of the modelling approach to capture actual thermal histories while bypassing the oscillating motion of the workpieces. Nevertheless, discrepancies in thermal gradients at the end of phase 3 between numerical predictions and experiments can be observed and is likely to affect subsequent residual stress calculation.

Figure 3-14 displays the temperature profiles obtained numerically and experimentally after 0.3 mm of burn-off (i.e. when the thermocouple initially positioned 0.3 mm away, reached the weld interface) for weld 2 and weld 4. Results for weld 1 are not shown since the thermocouple signals were lost before the first thermocouple reached the weld interface. Slopes of the temperature profiles were approximated from the gradients predicted numerically and measured experimentally, between 0 mm and 2.4 mm (an example is given in Figure 3-14 with the black dash line) and are presented in Table 3-5, along with the relative error between experimental and numerical slope values. A higher error is found for weld 4 with 16% compared to weld 2 with 7.6%. Discrepancies may have arisen from the positioning of the thermocouples since the thermal gradients generated during the LFW process are very high. In addition, uncertainties also arise from the measurement quality of the material properties used in the models. Finally, there is an oscillation in the temperature predicted 0.3 mm from the weld interface in the results presented in Figure 3-13. This is due to the approach used to account for the axial shortening with the step-wise removal of elements and is therefore a modelling artefact. However, it shows that this step-wise removal approach of material manages to capture the quasi-static state of the weld interface temperature.

The numerical end of phase 3 interface temperature of welds 1, 2 and 4 are 1022ºC, 1111ºC and 994ºC. Both, experiment and simulation demonstrate that increasing the rubbing velocity does not necessarily result in an increase of the interface temperature. This fact is in contrast with the results predicted by the numerical model of McAndrew et al.[8], where an increase in the rubbing velocity

resulted in an increase of the weld interface temperature, see Figure 3-15. Schroeder et al.[6] confirmed the effect of the rubbing velocity highlighted by McAndrew with his numerical model and thermocouple recordings. However, Li et al.[5] developed a 2D model where increasing the rubbing velocity did not affect the weld interface temperature. These peak temperature predictions are compared in Figure 3-15, which shows an increase of the weld interface temperature when increasing the rubbing velocity, for the rubbing velocities under 480 $mm.s^{-1}$. However, Turner's model predicted a similar weld interface temperature for the rubbing velocities above 480 $mm.s^{-1}$. Differences between the results may have arisen from the different modelling approaches used by the authors as well as the different workpiece geometries and material properties considered.

These divergent results highlight that the trend of the interface temperature cannot be predicted by looking only at the rubbing velocity. The behaviour of the process during the equilibrium phase is crucial to understanding these temperature differences. The interface temperature is determined by the balance between the heat input during this phase and the speed at which the hot material is removed from the interface, i.e. the burn-off rate.

In the case of weld 1, both the average power of phase 3 and the burn-off rate are low, as seen Table 3-4. This condition results in a slow heat up of the weld interface and more heat loss due to conduction into the surrounding cold material, creating a low thermal gradient, see Figure 3-16. Figure 3-16, shows that increasing the rubbing velocity at a constant applied pressure results in an increase of the thermal gradient. A similar trend can be observed in the works of McAndrew[8] and Turner[10]. In contrast to weld 1, weld 4 phase 3 power and burn-off rate are considerably higher. However, despite the high weld 4 power, the temperature cannot build-up at the weld interface since the hot material is removed at a high rate, creating a steep thermal gradient, see Figure 3-16. Weld 2 offers a compromise between weld 1 and 4 in terms of power and burn-off rate, which produced a higher temperature at the weld interface.

Table 3-5: Slope temperature distributions obtained after 0.3 mm burn-off

Weld	2 (model)	2 (experiment)	4 (model)	4 (experiment)
Slope (°C/mm)	-194	-210	-275	-327
Error (%)	7.6		16	

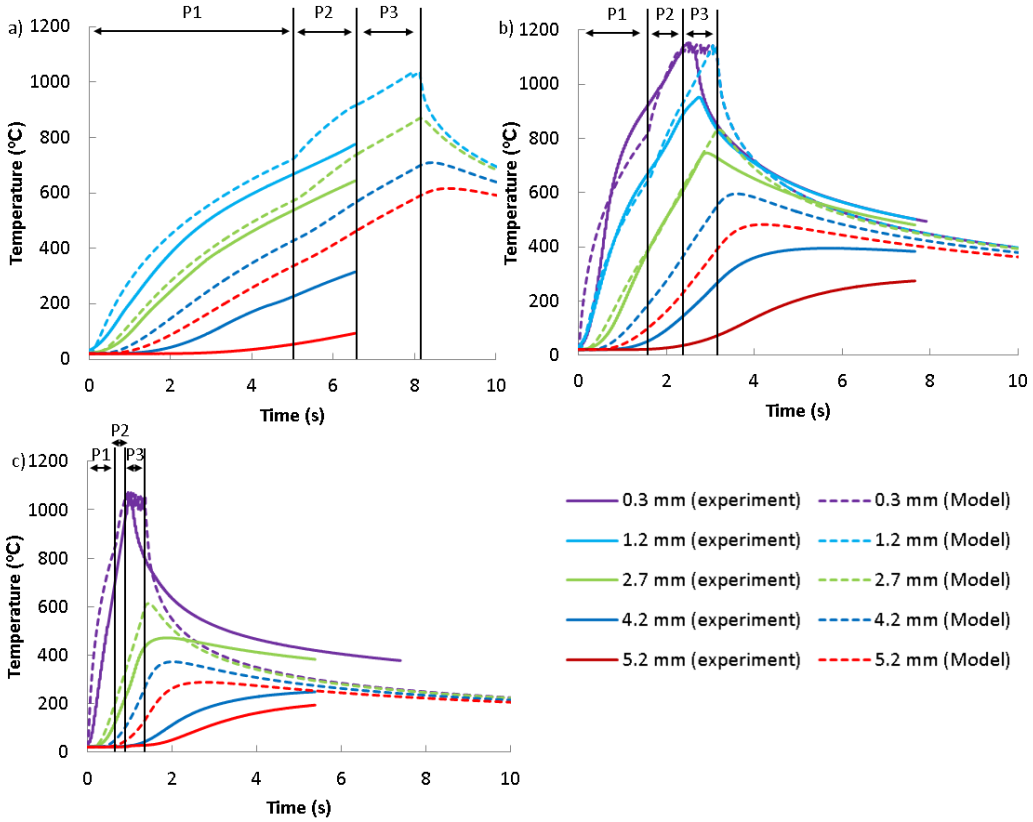

Figure 3-13: Comparison of thermal histories obtained from experiments and FEA simulations for three sets of welding conditions: a) weld 1 ($\boldsymbol{v_r = 120\ mm.s^{-1}}$), b) weld 2 ($\boldsymbol{v_r = 240\ mm.s^{-1}}$) and c) weld 4 ($\boldsymbol{v_r = 540\ mm.s^{-1}}$). P1, P2 and P3 correspond respectively to phases 1, 2 and 3 and the distances at which the temperature is recorded refer to the initial distances from the interface, prior any burn-off

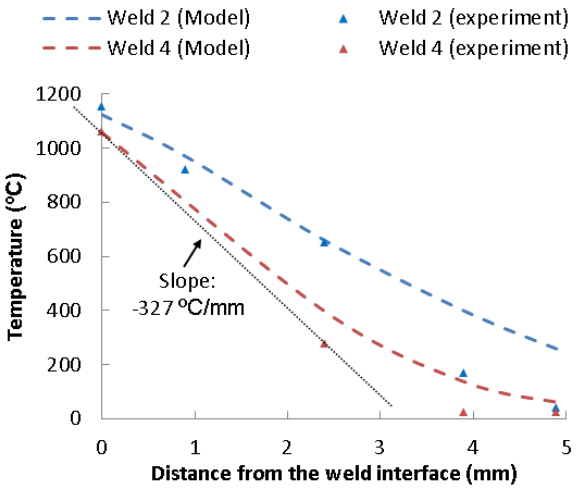

Figure 3-14: Comparison of temperature profiles obtained after 0.3 mm burn-off for weld 2 (time elapsed: 2.51 s) and weld 4 (time elapsed: 1 s)

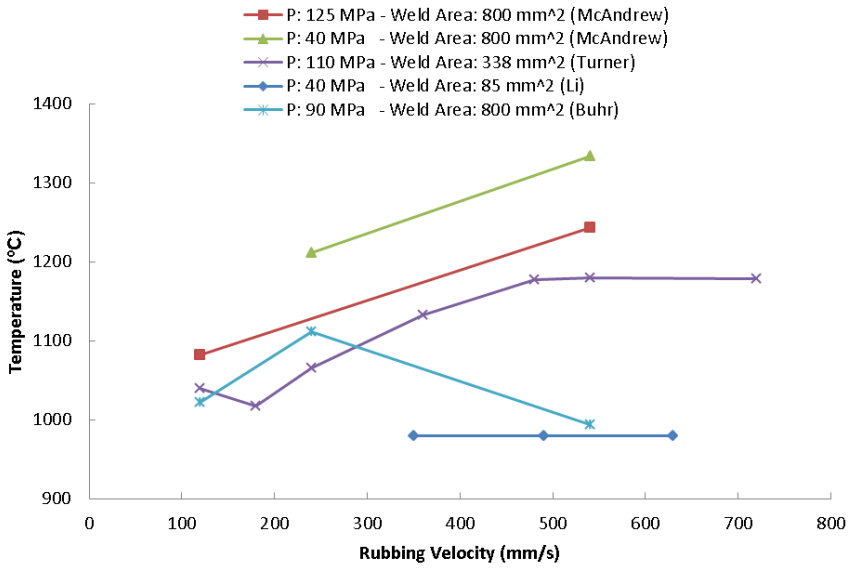

Figure 3-15: Evolution of the weld interface temperature during the equilibrium phase (i.e. phase 3 of the welding process) against the rubbing velocity predicted by: McAndrew et al.[8], Turner et al.[10] and Li et al.[5]

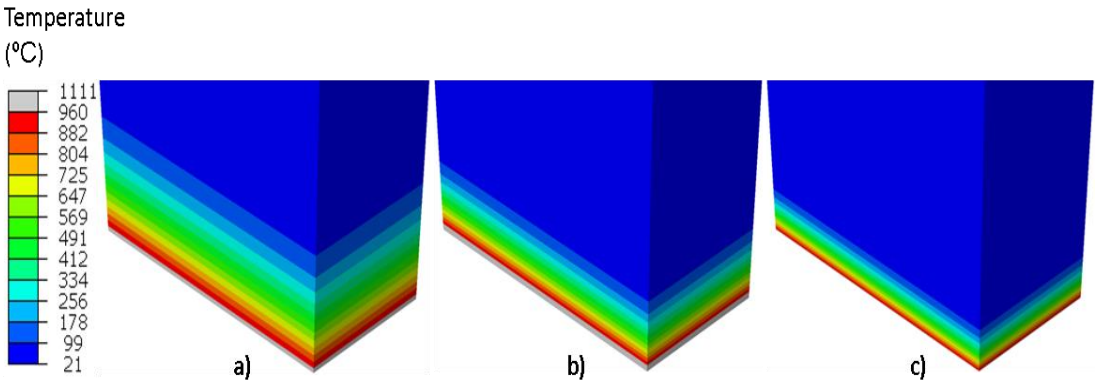

Figure 3-16: Thermal profiles, during phase 3 for: a) weld 1 ($v_r = 120\ mm.s^{-1}$), b) weld 2 ($v_r = 240\ mm.s^{-1}$) and c) weld 4 ($v_r = 540\ mm.s^{-1}$)

3.3.2.2 A method to estimate the weld interface temperature

To provide further evidence for the variation in peak temperature with rubbing velocity, models using the modelling approach developed in this chapter, were built for the experimental welding trials conducted by McAndrew et al.[11] displayed in Table 3-3. The burn-off rate is considered rather than the rubbing velocity so data from welds with different applied pressure can be integrated into the study.

The evolution of the average phase 3 power and the equilibrium phase 3 weld interface temperature against the burn-off rate are presented in Figure 3-17. For both plots, an equation of the trend with its R-squared (R^2) value is provided. It can be seen that the equilibrium power increases when increasing the burn-off rate. An increase in the burn-off rate can be achieved in three ways. It can be due to either an increase in rubbing velocity or applied pressure or oscillating in the short rather than long direction. In the first case, the power is linearly dependent on the velocity of the moving workpiece so an increase in the rubbing velocity results in an increase in the power magnitude. However, when oscillating in the shortest direction or increasing the applied pressure, the rubbing velocity is unchanged. In these cases the power increases because more cold material is introduced to the weld interface, therefore the interface force and consequently the power will increase accordingly.

As stated previously, the peak temperature is determined by a balance between equilibrium phase 3 power and the phase 3 burn-off rate. The highest interface temperature is reached for a burn-off rate between 2 and 3 mm/s while increasing or decreasing the burn-off rate outside this, results in a drop in temperature. This trend in the temperature confirms the results obtained in the previous section on the influence of the rubbing velocity. Based on Figure 3-17, it is possible to estimate the magnitude of the weld interface temperature obtained at the end of the welding process, without using thermocouples or a numerical model, from the experimental burn-off rate or the equilibrium power. It is worth mentioning that Figure 3-17 is only valid for the workpiece geometry used in this study.

To understand the contributions of heat lost by conduction and lost in the flash, a heat balance over a control volume around the weld interface can be developed:

$$\mathrm{Q}_{Total} = Q_{in} - Q_{conduction} - Q_{flash} \qquad 3\text{-}6$$

where $\mathbf{Q_{Total}}$ is the total energy contained in the control volume, $\boldsymbol{Q_{in}}$ is the energy brought in the control volume by sliding or plastic work, $\boldsymbol{Q_{conduction}}$ is the energy lost by conduction and $\boldsymbol{Q_{flash}}$ is the energy lost in the flash.

When the process is in steady-state, this equation simplifies to the following after differentiating with respect to time:

$$\dot{Q}_{conduction} = \dot{Q}_{in} - \dot{Q}_{flash} \qquad 3\text{-}7$$

Assuming that the temperature field reaches a quasi-steady state, with $\dot{Q}_{Total} = 0$. Furthermore, $\dot{Q}_{in}$ represents the average equilibrium power, previously calculated from the post-processing of the machine data, while $\dot{Q}_{flash}$ is given by:

$$\dot{Q}_{flash} = \rho . A . c_p . BoR . (T_{flash} - T_{init}) \qquad 3\text{-}8$$

where $\boldsymbol{\rho}$ is the density, $\boldsymbol{A}$ the area of the weld cross-section, $\boldsymbol{c_p}$ the specific heat capacity (an average value of 690 J/(Kg.K) is used) , $\boldsymbol{BoR}$ the burn-off rate,

$\boldsymbol{T_{flash}}$ the temperature of the flash (taken at 1000ºC) and $\boldsymbol{T_{init}}$ the temperature of the workpieces prior to welding.

Figure 3-18 a) displays the evolution of the magnitudes of the powers acting in and out of the control volume against the burn-off rate. The power responsible for heat losses in the flash increases linearly with the burn-off rate, and dominates $\dot{Q}_{in}$. However, the heat loss due to conduction is largely independent of the burn-off rate used. Figure 3-18 b) displays the magnitude of the powers lost in the flash and by conduction, expressed as a percentage of $\dot{Q}_{in}$. The objective of Figure 3-18 b) is to quantify the contribution of the two mechanisms responsible for heat losses in the control volume. It can be observed that for burn-off rates less than about 3 mm/s, the power lost by conduction represents about 30% of the total required to make the weld. Above a 3 mm/s burn-off rate, the contribution of conduction decreases to a value of about 6%. Therefore conduction has a much greater impact on the temperature field at low burn-off rates. If conduction is ignored, the power to make a weld can be estimated from the energy required to produce the flash (Equation 3-8).

As previously mentioned, an increase in the applied pressure is known to increase the burn-off rate (see Table 3-4 burn-off rate values, weld 3 versus weld 4 where the applied pressure increases from 40 MPa to 90 MPa). However it is possible to reduce the peak temperature by reducing the applied pressure and the burn-off rate according to the relationship in Figure 3-17. This would contradict findings in the literature[8,13]. McAndrew et al.[8] established that a decrease in the applied pressure has a small impact on the experimental phase 3 power. Furthermore, using McAndrew's equation[8] (see Appendix B) which predicts experimental burn-off rates, the evolution of the burn-off rate is plotted against the applied pressure for different rubbing velocity conditions in Figure 3-19 (the amplitude is kept constant at 3 mm while the frequency varies from 10 Hz to 50 Hz). This demonstrates that the burn-off rate is largely independent of the applied pressure for low rubbing velocities. Hence, low burn-off rates can only be achieved by reducing the rubbing velocity and not the applied pressure. Consequently, if the initial burn-off rate is 2 mm/s and the applied pressure is

decreased, it will not affect the burn-off rate or the phase 3 power; therefore the weld interface temperature will be unchanged.

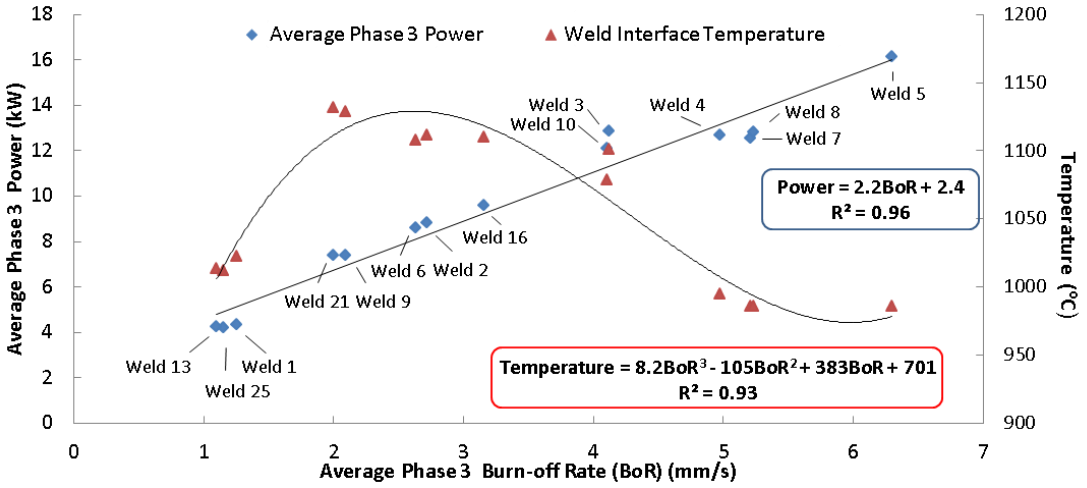

Figure 3-17: Evolution of the average phase 3 power and the equilibrium phase 3 weld interface temperature against the average phase 3 burn-off rate

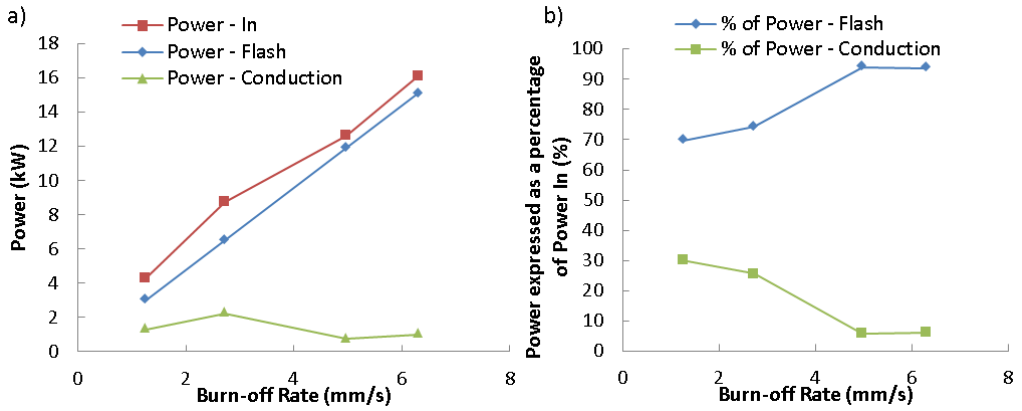

Figure 3-18: a) Evolution of the power magnitudes, acting in and out of a control volume, against the burn-off rate and b) contributions of the powers from the flash and conduction expressed as a percentage of the power in

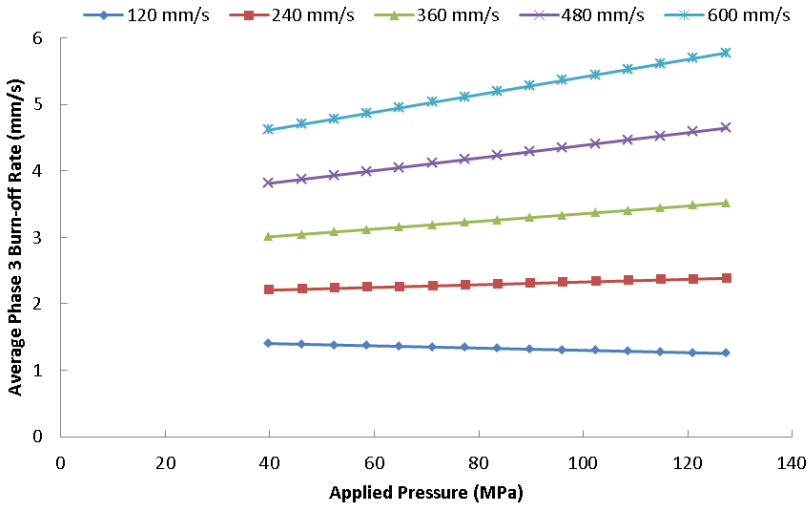

Figure 3-19: Evolution of the burn-off rate against the applied pressure for different rubbing velocities (obtained from McAndrew et al.'s equation[8], see Appendix B)

3.3.2.3 Influence of the applied pressure

Comparisons of thermal histories between experiments and simulations, for weld 3 and weld 4, are displayed in Figure 3-20. Both welds were made with a rubbing velocity of 540 $mm.s^{-1}$ while using an applied pressure of 40 MPa for weld 3 and 90 MPa for weld 4. Similar discrepancies to those previously observed in Figure 3-13 are present in Figure 3-20. Figure 3-21 displays the temperature profiles obtained numerically and experimentally after 0.3 mm of burn-off for weld 3 and weld 4. Slopes of the temperature profiles were approximated from the gradients predicted numerically and measured experimentally, between 0 mm and 2.4 mm, and are presented in Table 3-6, along with the relative error between experimental and numerical slope values. Differences in thermal gradients, at the end of phase 3, obtained numerically and experimentally are believed to be a result of sensitivity to the thermocouple locations in the experiments, combined with steep thermal gradients; the assumption of constant heat flux for each phase; uncertainty in power values when using machine data and the accuracy of the material properties used. A higher maximum temperature is reached for the lower applied pressure weld 3 compared to weld 4 reaching numerically 1170ºC and 994ºC respectively. The same trend was observed by McAndrew et al.[8] and Turner et al.[13]. Looking at

Table 3-4, the applied pressure of 40 MPa compared with 90 MPa had virtually no impact on the phase 3 power, with a variation of about 1 %, however it decreased the burn-off rate by about 17 %. Therefore, for an equivalent power, the hot material was left a longer time at the weld interface, allowing the temperature to build-up. It is worth noticing that even if the burn-off rate of weld 3 is lower than weld 4, it is still substantially higher than the burn-off rate of weld 1 (over three times higher) and the temperature at the interface does not have time to conduct back to the same extent.

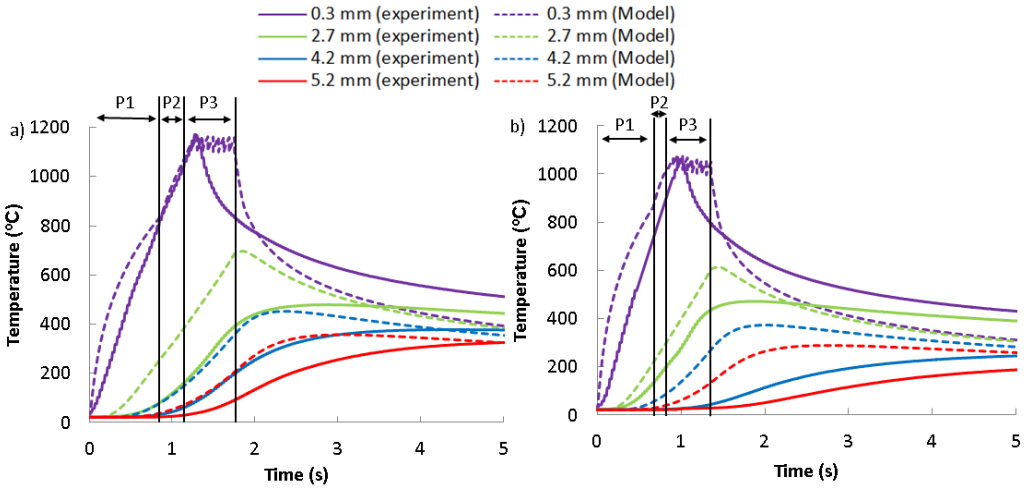

Figure 3-20: Thermal histories obtained from experiments and FEA for two sets of experimental conditions where only the applied pressure changes: a) weld 3 (P = 40 MPa) and b) weld 4 (P = 90 MPa)

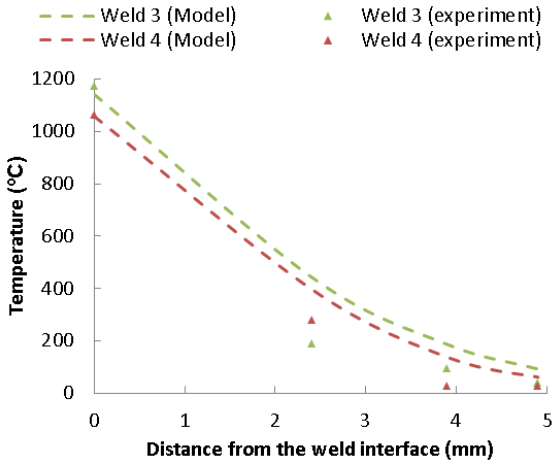

Figure 3-21: Comparison of temperature profiles obtained after 0.3 mm burn-off for weld 3 (time elapsed: 1.27 s) and weld 4 (time elapsed: 1 s)

Table 3-6: Slope temperature distributions obtained after 0.3 mm burn-off

Weld	3 (model)	3 (experiment)	4 (model)	4 (experiment)
Slope (^{o}C/mm)	-291	-410	-275	-327
Error (%)	29		16	

3.3.2.4 Influence of the oscillation direction

Temperature histories of weld 4 and 5 are displayed Figure 3-22, where the oscillating workpiece was oscillated respectively in the 40 mm and 20 mm directions of the workpiece. Figure 3-23 displays the temperature profiles obtained numerically and experimentally after 0.3 mm of burn-off for weld 3 and weld 4. Slopes of the temperature profiles were approximated from the gradients predicted numerically and measured experimentally, between 0 mm and 2.4 mm, and are presented in Table 3-7, along with the relative error between experimental and numerical slope values. The potential causes of the discrepancies observed between numerical predictions and experiments are the same than those discussed in previous sections. As shown in Figure 3-22, a slightly cooler weld is produced when oscillating in the 20 mm direction. As shown in Table 3-4, the sample that was oscillated in the 20 mm direction (i.e. weld 5) had a 27 % higher burn-off rate compared to weld 4 despite having the same rubbing velocity which is in agreement with McAndrew et al.[49]. Oscillating in the 20 mm direction facilitates the expulsion of the material since the material has less distance to travel to form the flash. In addition, the phase 3 power of weld 5 is 27 % higher compared to weld 4, which explains why weld 4 and weld 5 have similar weld interface temperatures.

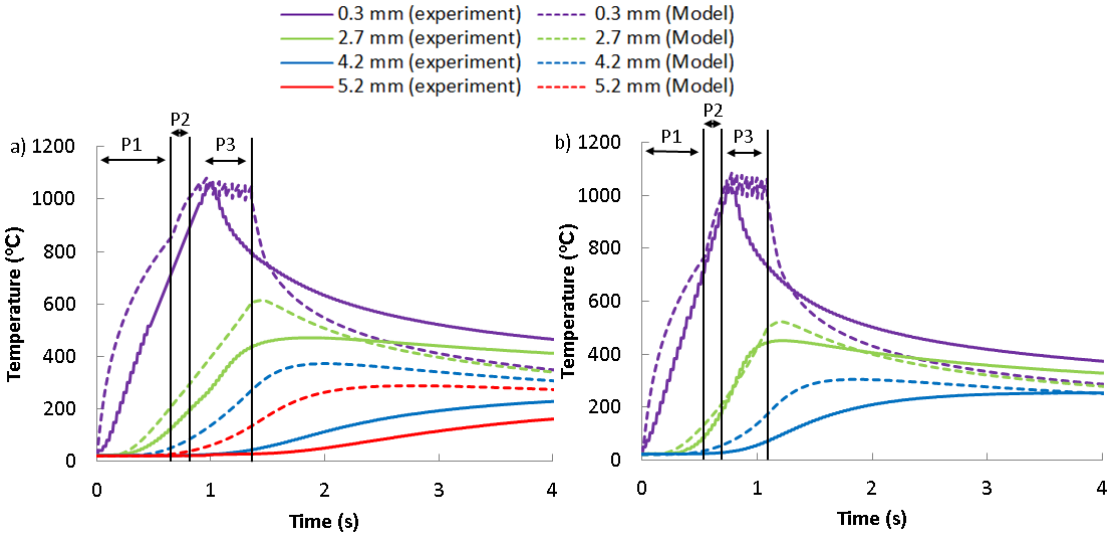

Figure 3-22: Thermal histories obtained from experiments and FEA for two sets of experimental conditions where only the oscillation direction changes: a) weld 4 (40 mm direction) and b) weld 5 (20 mm direction)

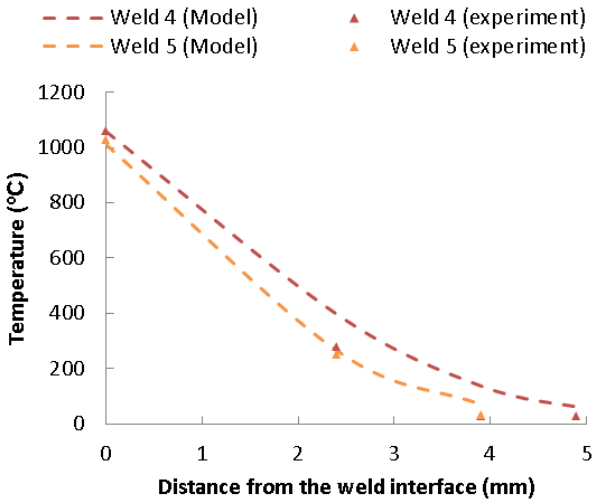

Figure 3-23: Comparison of temperature profiles obtained after 0.3 mm burn-off for weld 4 (time elapsed: 1 s) and weld 5 (time elapsed: 0.78 s)

Table 3-7: Slope temperature distributions obtained after 0.3 mm burn-off

Weld	4 (model)	4 (experiment)	5 (model)	5 (experiment)
Slope (°C/mm)	-275	-327	-311	-324
Error (%)	16		4	

3.4 Conclusions

The key findings from this work are:

1. A novel LFW process model that bypasses the need to dynamically model the oscillations was developed. The advantage of this modelling approach is that thermal profiles can be obtained quickly for subsequent residual stress modelling.

2. The overall trend of the thermal history measured by thermocouples is captured by the model. However, discrepancies in thermal gradients obtained at the end of phase 3 between numerical predictions and experiments were observed. Errors in thermal gradients obtained after 0.3 mm of burn-off between experiments and simulations ranged from 4% with weld 5 to 29% with weld 3.

3. According to the model, the weld interface temperature does not necessarily increase with the rubbing velocity. Moreover, applying a high pressure or oscillating the workpiece along the shorter of the two interface dimensions produces a cooler interface temperature. Overall, the interface temperature can be explained by a balance between heat generation and the heat lost as a consequence of the flash generation.

4. A maximum weld interface temperature is reached for burn-off rate values between 2 and 3 mm/s, for the workpiece geometry used in this study.

In the next chapter, the modelling approach developed in this one will be expanded to investigate the residual stresses formed during the post-oscillatory motion cool-down phase.

Chapter 4: Development of a 3D mechanical model and effects of process parameters on residual stress

This chapter is an edited version of the following articles:

Bühr, C., Bilal, A., Colegrove, P. A., McAndrew, A. R., Guo, H. & Zhang, X. Prediction of residual stress within linear friction welds using a computationally efficient modelling approach Materials & Design (2018). doi:10.1016/j.matdes.2017.11.013

4.1 Background

The combined effects of residual stress, external loading, poor microstructure and existing defects may dangerously lower the stress at which failure happens; therefore it is important to understand how residual stresses are created. Most LFW models developed in the literature have been used to study the process during the welding phases, such as flash morphology[6,7], expulsion of contaminants[8] and prediction of thermal histories[5,6,9,11]. However, only few authors develop numerical models capable of predicting residual stresses[13,14,16,93]. Previous authors addressed the effect of the applied pressure on the residual stress formation; however no studies are available on the rubbing velocity and oscillation direction. Following the approach presented in the previous chapter, the author aims to develop a 3D mechanical model for predicting the residual stress while bypassing the modelling of the oscillations. Furthermore, the effect of various process parameters on residual stress development will be investigated.

4.2 Methodology

4.2.1 Experiments

4.2.1.1 Contour method for measurement of residual stress

Four contour method measurements and the associated FE analysis were provided as an external service by Coventry University on selected welds made at TWI and described in the previous chapter, i.e. welds 1 – 4 in Table 4-1. An additional sacrificial sample was used to determine the appropriate EDM parameters to avoid rupture of the EDM wire during the cut. A weld is shown before being cut with the EDM in Figure 4-1 a) and after cutting in Figure 4-1 b). The same coordinate system used in chapter 3 is reused in this chapter to designate residual stresses. All the EDM cuts were conducted along the plane (y, z) at mid-width, however two cutting directions were used and are presented in Figure 4-2. Low power cutting parameters were used to conduct the cuts for the welds 1, 2 and 3. The settings were adjusted to get the best possible surface finish as well as to minimise cutting artefacts. A self-equilibrium cutting strategy was used for weld 4 where the cut simultaneously passed through the tensile and compressive stress regions[118]. The cut was possible with high power settings, however surface roughness increases with high power parameters, potentially resulting in an under-estimation of the tensile residual stress in the weld. The WEDM cut progressed smoothly with a little variation in the cutting speed and without wire breakage. Using a self-equilibrium cutting strategy, the author hoped to minimise cutting-induced plasticity. This was not the case for the other welds where the cut passed sequentially from a compressive to a tensile stress region and finally to a second tensile region. A coordinate measuring machine (CMM), shown in Figure 4-3 a), was used to measure the displacement profile[81] by probing the cut face of the weld using a ruby sphere tip with a 3 mm diameter and a 0.5 mm spacing between measurement points. The length measurement error of the CMM is about 1.5 µm. The surface displacement data of both cut halves of the sample was analysed for data aligning, cleaning, flattening and smoothing using a Matlab

analysis routine. The data smoothing was performed with cubic splines of knot spacing 5.5 mm in both *y* and *z* directions. An example of a displacement profile obtained with the CMM is given in Figure 4-3 b). Examples of spline fitting curves for different knot spacing (black spline curve: 5.5 mm knot spacing), at a fixed *z* position, are shown in Figure 4-4 a).The displacement from the splines is applied to a FEA linear elastic model, representing half of the welded sample (see Figure 4-5). The mesh of the FE model was composed of 8-node brick elements with a uniform length of 0.5 mm along the sample thickness. A fine element length of 0.1 mm was used at the weld interface, which then coarsen to 2 mm. Additional boundary conditions were imposed to restrain rigid-body motion, as shown in Figure 4-5, before calculating the residual stress field. Finally, the solution of the FEA model gives the residual stress in the x direction across the plane of the cut (y, z)[75], as presented in Figure 4-4 b) using a Young's modulus of 117 GPa and Poisson's ratio of 0.33.

Table 4-1: Welding parameters for welds measured experimentally (1-4) and numerically modelled (1-5)

Weld	Freq. (Hz)	Amp. (mm)	Applied Pressure (MPa)	Burn-off (mm)	Rubbing Velocity (mm/s)	Oscillation Direction Along the Interface Dimension	Measurement Method: Neutron Diffraction (ND) Contour Method (CM)
1	20	1.5	90	3	120	40 mm	ND & CM
2	30	2	90	3	240	40 mm	CM
3	50	2.7	40	3	540	40 mm	CM
4	50	2.7	90	3	540	40 mm	CM
5	50	2.7	90	3	540	20 mm	-

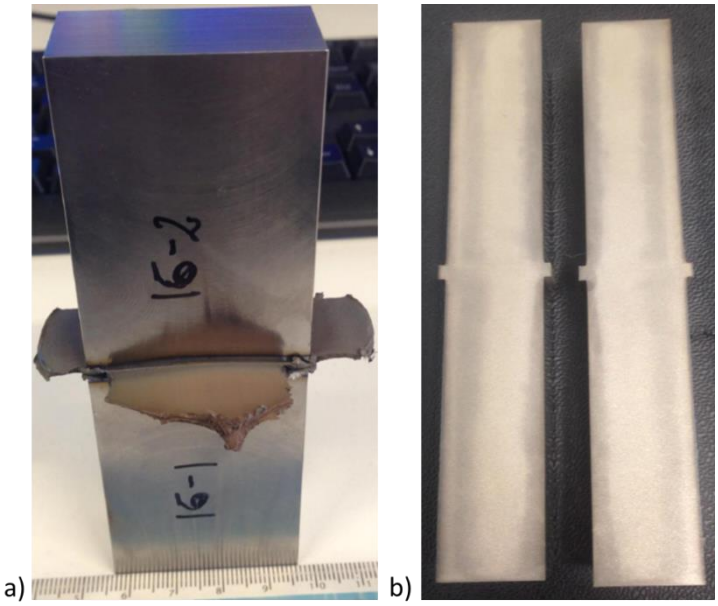

Figure 4-1: Ti-6Al-4V linear friction weld a) before EDM cut and b) after EDM cut

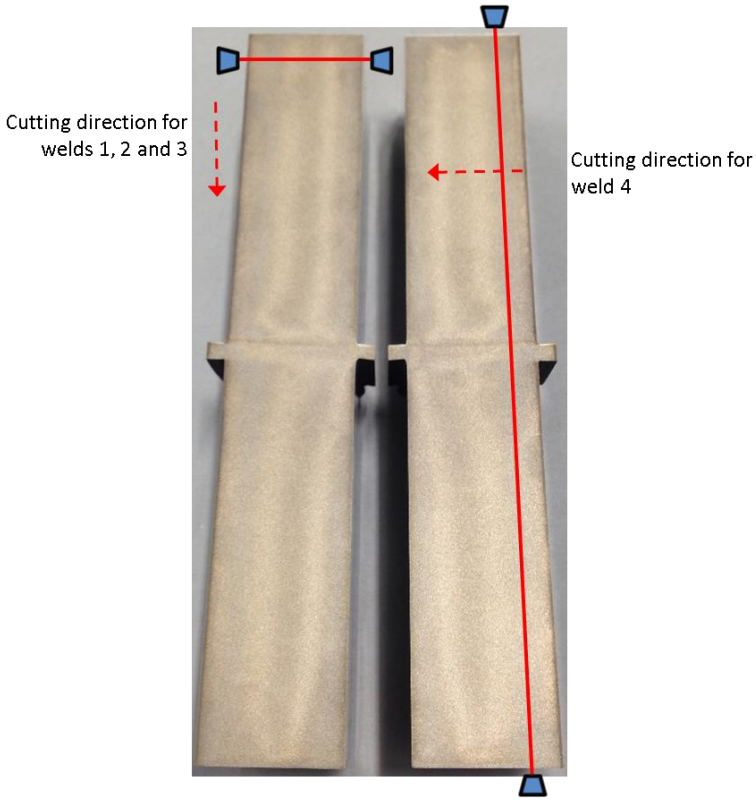

Figure 4-2: EDM cut directions for the welds 1, 2, 3 and 4

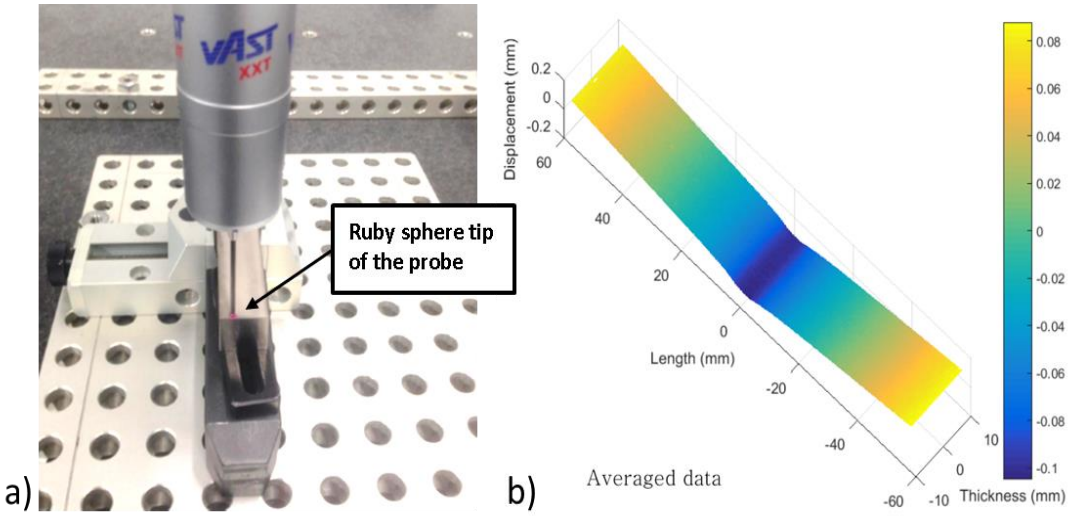

Figure 4-3: a) CMM machine and b) Displacement profile of weld 1 measured by the CMM machine

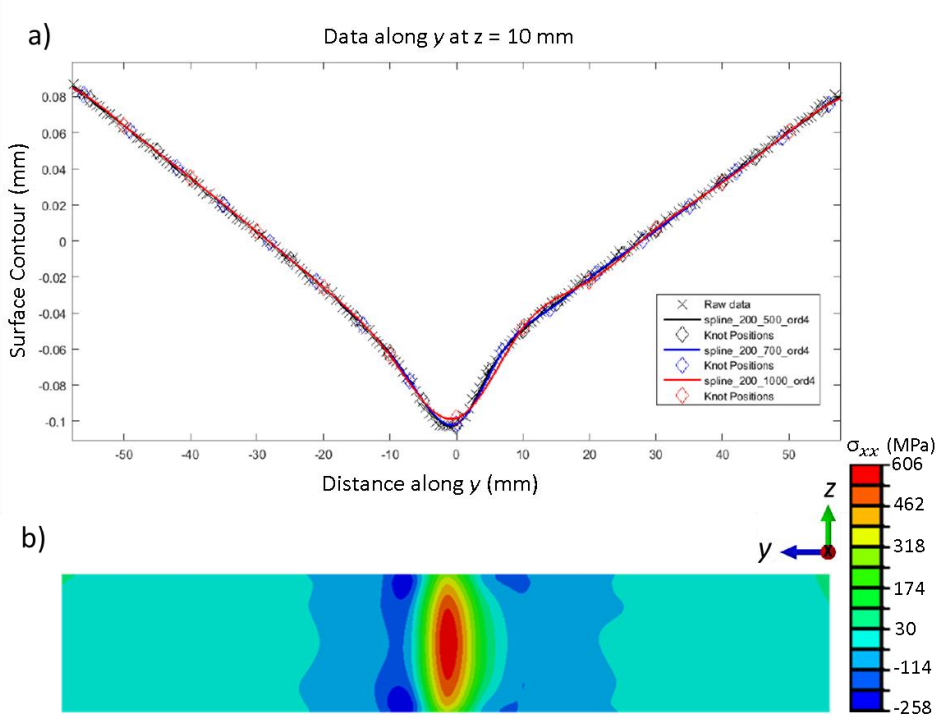

Figure 4-4: a) Spline fitting of the displacement profile of weld 1 and b) Residual stress predicted by the FEA model for weld 1 in the *x* direction

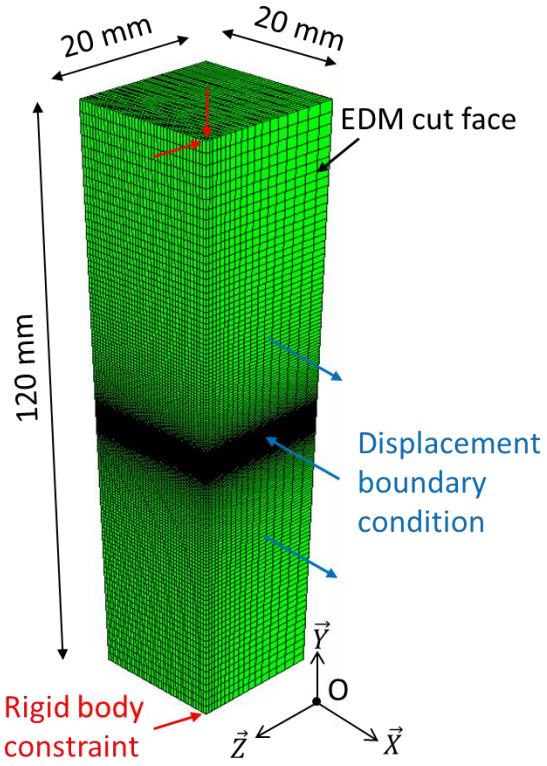

Figure 4-5: FEA model used in the contour method

4.2.1.2 Neutron diffraction for measurement of residual stress

Neutron diffraction experiments on weld 1 were conducted at the ISIS facility of the Rutherford Appleton Laboratory in the UK by the author. To reduce the path length of the neutrons within the material and improve the quality of the signal measured as well as reducing measurement times, the LFW was EDM cut through the thickness to achieve dimensions of 8 x 40 x 120 mm (originally 20 x 40 x 120 mm). A specimen 5 x 6 x 120 mm was also EDM cut from the LFW weld to measure the stress-free lattice parameters. The dimensions 6 mm and 5 mm assured a stress free state in the x and z directions while residual stresses in the y direction have to balance along the plane P2, see Figure 4-7, with the reduced area of 6 mm x 5 mm. Therefore, no stress is expected in the y direction.

The neutron diffractometer ENGIN-X was used to measure the elastic strains located in the weld at several positions. ENGIN-X is a time of flight (TOF)

diffractometer using a neutron spallation source. Neutrons are produced as a result of periodic collisions of high energy protons with a target, previously accelerated in a synchrotron[119]. Neutrons with different wavelengths are produced allowing multiple crystallographic planes to be measured at once at a fixed angle. Since two measurements are made simultaneously using the two detector banks positioned at a Bragg's angle of ± 90 degrees (Figure 4-6), the LFW had to be repositioned once to measure the third direction. Consequently, the elastic strains in the *z* direction were measured twice allowing the repeatability of the measurements to be determined. Cuboid gauge volumes, defined by the slit dimensions and the position of the bank collimators, of 3 x 2 x 3 mm were used for measuring the *x* and *z* directions and 4 x 2 x 3 mm for the *y* and *z* directions. Five positions were measured in total with the first position being at the weld interface with the next three measurements being 1 mm apart and the final one 2 mm apart. Due to the limited time available at the ISIS facility, elastic strains on only one side of the weld interface were measured; however results from the literature have shown that residual stresses distributed within Ti-6Al-4V LFW are approximately symmetrical around the weld interface[18,45,50,51]. Stress-free lattice parameters were measured for each position from the stress-free specimen. Finally assuming isotropic elastic properties, Hooke's law was used to calculate the residual stresses σ_{ii} from the elastic strains ε_{ii} as follows:

$$\sigma_{ii} = \frac{E}{(1+\nu)(1-2\nu)}\left[(1-\nu)\varepsilon_{ii} + \nu\left(\varepsilon_{jj} + \varepsilon_{kk}\right)\right], \qquad i,j,k \in x,y,z \tag{4-1}$$

where $\boldsymbol{E}$ is the Young's modulus and $\boldsymbol{\nu}$ the Poisson's ratio.

Neutron diffraction spectra measured simultaneously in the direction *x* and *z* of the LFW are presented in Appendix C. The quality of the diffraction peaks was more consistent for the crystallographic plane $\{\mathbf{10\bar{1}1}\}$ and fitting errors were minimal. Consequently, lattice distances from this plane were used to calculate elastic strains and subsequently residual stresses using a Young's modulus of 98 GPa[120] specific to this crystallographic plane $\{\mathbf{10\bar{1}1}\}$ and a Poisson's ratio of 0.33. This Young's modulus value was only used for the neutron diffraction

measurements and a temperature dependent isotropic value was used for the numerical simulations. Calculated error bars display fitting errors for the measured diffraction peaks, correctly propagated through the calculations of residual stresses (see Appendix D for an example of calculus).

A comparison between residual stress measured using neutron diffraction and those predicted numerically is provided in the results section. To numerically account for the EDM cut, an equivalent amount of material was removed from the model allowing the redistribution of the residual stress field. Apart from this comparison, the EDM cut was not considered within the numerical models.

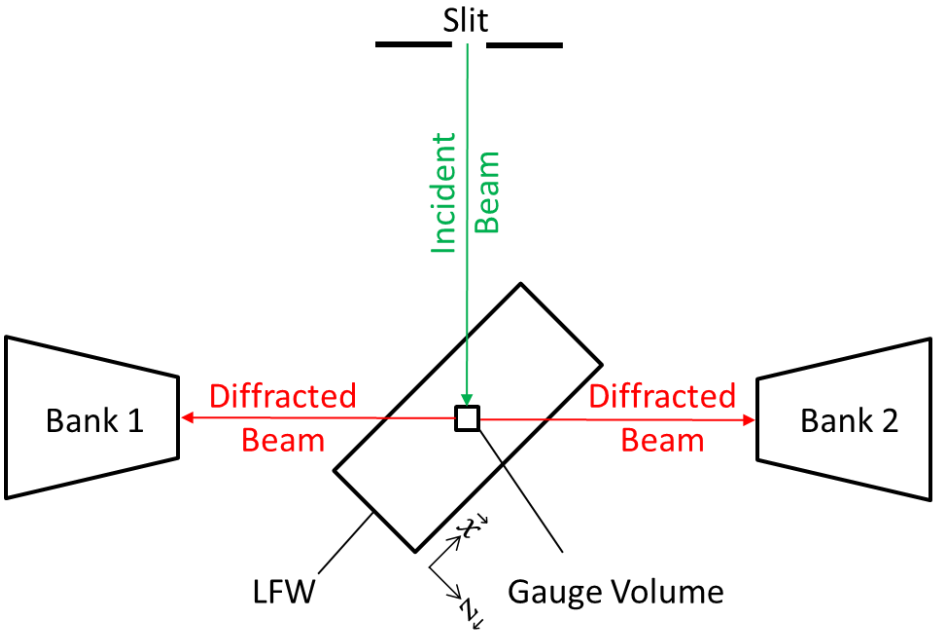

Figure 4-6: Experimental set-up used with ENGIN-X diffractometer

4.2.2 Modelling approach

The previous chapter details the modelling approach developed to bypass the modelling of the oscillations inherent to the LFW process. The approach has been successfully implemented to predict thermal histories and is now expanded to the prediction of the stress field during welding and the residual stress field after weld completion. Numerical models were created with ABAQUS for welds 1 – 5 in Table 4-1 (Average phase 3 power and average

phase 3 burn-off rate values for welds 1 – 5 are given in Table 3-4). This modelling approach reduces the calculation time for 3D models from weeks[8] to 15 hours. The following sections describe the sequentially coupled thermal-stress analysis conducted in this chapter.

4.2.2.1 Mesh and material properties

As in section 3.2.2.1, a workpiece measuring 10 x20 x 60 mm was modelled, representing an eighth of the full structure, as shown in Figure 4-7. A mesh composed of eight-node linear brick elements with reduced integration and hourglass control of type C3D8R was used. A fine element length of 0.3 mm was used at the weld interface and its vicinity, which then coarsened to 1 mm.

Temperature dependent Ti-6Al-4V material properties were used for the models (see Figure 2-27). Flow stress data for temperatures less than and equal to 700ºC are taken from Chen et al.[115] at a quasi-static strain rate. From 800ºC and beyond, flow stress data from Guo et al.[116] are used; the material exhibits a drop in strength and a perfectly plastic behaviour[10]. Flow stress values between 700ºC and 800ºC are interpolated linearly by ABAQUS and might not represent accurately the evolution of the work hardening of the material in this temperature range. An annealing temperature of 800ºC is defined in ABAQUS to simulate the relaxation of the accumulated stresses and strains above this temperature. Above 800ºC, Ti-6Al-4V has a reduced strength due to the high temperature experienced and becomes a single phase material when reaching the beta-transus temperature at approximately 1000ºC[110,114] where its strength significantly reduces. Above 800ºC, Ti-6Al-4V also experiences dynamic recrystallization due to the deformation and high temperature[114,121]. Young's modulus was taken from Turner et al.[13] while thermal expansion coefficient values are from Boyer et al.[88], see Appendix A for further details on the material properties. It is worth mentioning that the thermal expansion coefficient does not include the change in density of the material when the initial alpha-beta microstructure forms a single beta-phase microstructure, when the welding temperature reaches the beta-transus temperature.

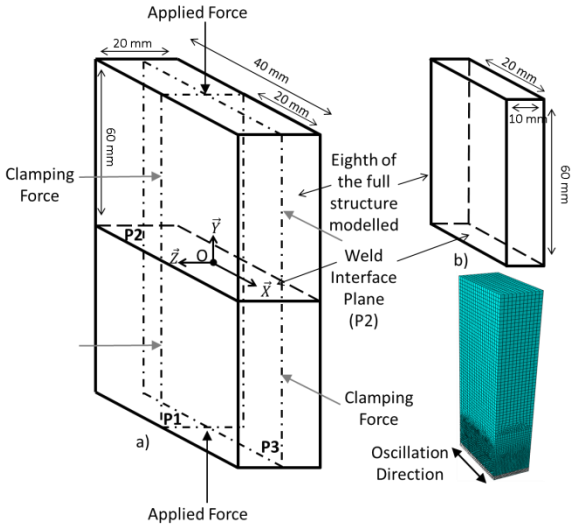

Figure 4-7: a) Schematic diagram of the full LFW structure with the applied and clamping forces and its planes of symmetry, P1, P2 and P3 and b) eight of the full structure modelled

4.2.2.2 Loading, boundary conditions and modelling of the burn-off

To account for the effect of the heat on the stress field, the temperature history previously predicted in chapter 3, through phases 1 to 3 and cooling, using the thermal model is mapped on the mechanical model. Therefore, the effect of thermally-induced expansion and contraction of the material on the stress field is accounted for. At the end, an extra cooling step is added to bring the model to room temperature. The elastic-plastic mechanical model, neglects the oscillations and the expulsion of material due to the forging force. The forging force is taken equal to the applied force, as for the experiments, and will be referred as applied force (i.e. the forging force is the applied force during the cooling period). The applied force (expressed as a pressure in Table 4-1) and the clamping force are both applied as pressures on the model. The clamping force represents the force applied by the clamping tool on the sides of the workpiece (Figure 4-8) and is equal to the applied force, as for the experiments. The clamping force is not applied to a band 6.6 mm from the interface as is the case with the experiments. The applied force is applied on the top surface of the workpiece. Applied force and clamping force are applied during the welding phases and for the first 15 s of cooling before being released. Three symmetry

boundary conditions are applied to the model to account for the planes of symmetry P1, P2 and P3, see Figure 4-7 a). Finally, the burn-off is accounted in the same way as in the previous chapter, i.e. by removing iteratively a row of elements at a pace which matches the experimental burn-off rate. As a consequence of removing rows of elements, the load applied on those elements is discarded, along with the heat. Since the material contained in those rows is at high temperature, it has very low flow strength so the impact of the stress on the rest of the structure is minimal.

Similar to the previous chapter, the influence of the rubbing velocity was studied in the result section by comparing welds 1, 2 and 4. The effect of the applied force, during welding and cooling (i.e. the forging and applied forces were the same), is examined using welds 3 and 4, while the oscillation direction is studied using welds 4 and 5. Although the oscillations are not simulated, the effects of the rubbing velocity and oscillation direction are accounted for in the average power values, durations of the phases and average phase 3 burn-off rates calculated from the machine data recorded during the welding trials. Stress and temperature profile plots were extracted at mid-thickness of the weld (i.e. along a line located along plane P1, see Figure 4-7, and going through the point O).

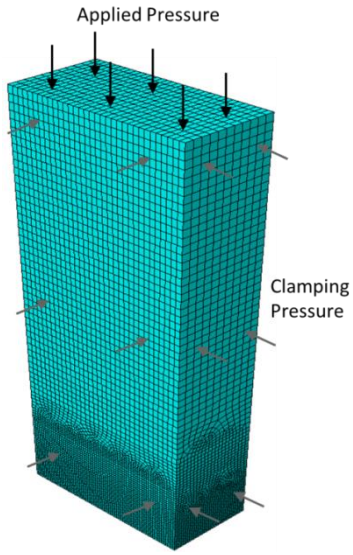

Figure 4-8: Applied and clamping forces applied and referred as pressures on the model

4.3 Results and discussion

4.3.1 Comparison of residual stresses predicted numerically against neutron diffraction and contour method measurements

Since lattice parameters were measured using neutron diffraction, twice independently in the direction *z*, it provides valuable information on the repeatability of the measurements. Lattice and stress-free lattice parameters in the direction *z* for weld 1 are presented in Figure 4-9 for both orientations and demonstrates the good repeatability of the measurements made.

Residual stresses in weld 1, in the three directions of space calculated from the lattice parameters along with those measured using the contour method and predicted numerically after accounting for the EDM cut, are displayed in Figure 4-10. Residual stresses from the contour method were predicted for the full thickness LFW. The FEA model only recorded a small variation in the residual stress magnitudes (25 MPa at the weld interface) when accounting for the EDM cut. Therefore, contour method predictions from the full thickness weld can be compared with the neutron diffraction and FEA results. Residual stresses resulting from the model and contour method were averaged over similar gauge volumes to those used for neutron diffraction to facilitate the comparison. Tensile residual stresses are located in the directions *x* and *y* while the *z* direction is virtually stress-free, as shown in Figure 4-10. According to the literature[18,45,50,51], the residual stress in the *z* direction is not expected to be stress-free. However, as previously mentioned, the original LFW was EDM cut to reduce the neutron path length. As a consequence, the weld interface dimension in the *z* direction was reduced to 8 mm compared to the original 20 mm. Figure 4-10 shows that a plane stress condition is reached in the *z* direction with a sample thickness of 8 mm. In agreement with the literature[18,45,50], lower tensile residual stresses are expected in the direction of the applied pressure (y axis) compared to the longest direction of the weld interface (*x* axis). Interestingly a decrease in the residual stress magnitude is recorded at the weld interface compared to the gauge volume positioned one

millimetre away. A similar pattern is shown by Dewald et al.'s[18] neutron diffraction measurements. Positioning the gauge volume at the weld interface is a difficult task and combined with the effect of fitting errors are believed to be at the origin of the trend observed.

Overall, discrepancies are found between residual stress values measured by neutron diffraction and contour method and modelling predictions. The discrepancies recorded between FEA and contour method values range from 20 MPa (2 mm from the weld interface) to 114 MPa (3 mm from the weld interface). The discrepancies recorded between FEA and neutron diffraction values range from 57 MPa (2 mm from the weld interface) to 217 MPa (at the weld interface).The plane stress condition in the *z* direction as a result of the EDM cut, is captured by both neutron diffraction and model values. Modelling results tend to predict a higher peak of residual stress magnitude and a steeper distribution. This could be a result of the lack of flow stress values between 700ºC and 800ºC, not representing accurately the evolution of the work hardening of the material in this temperature range. Furthermore, EDM cuts may have introduced inaccuracies in the contour method measurements, which is discussed in the following section.

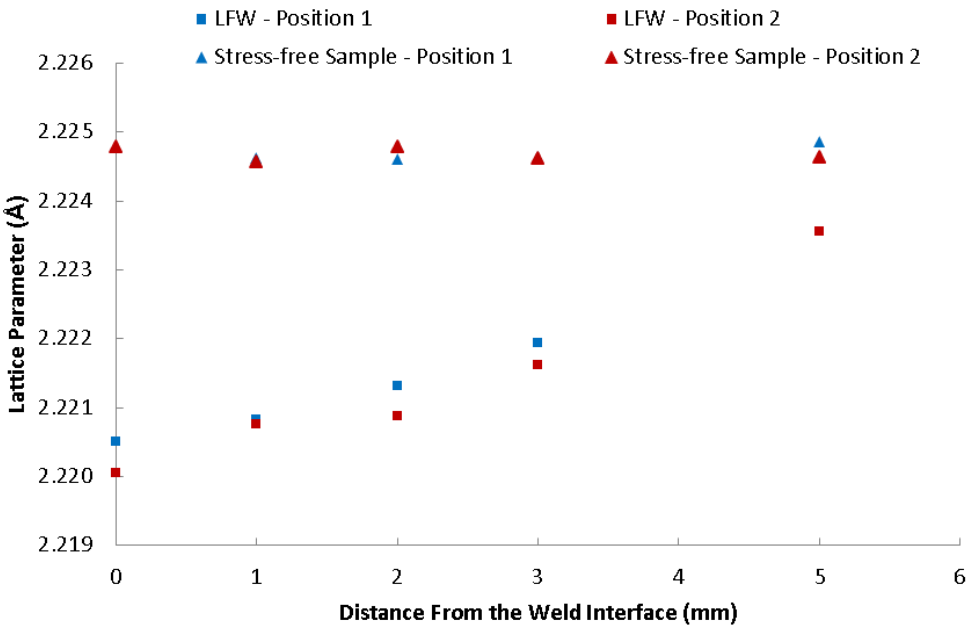

Figure 4-9: Lattice and stress-free lattice parameters measured in the *z* direction for two different sample positions for the LFW weld 1 and stress-free samples

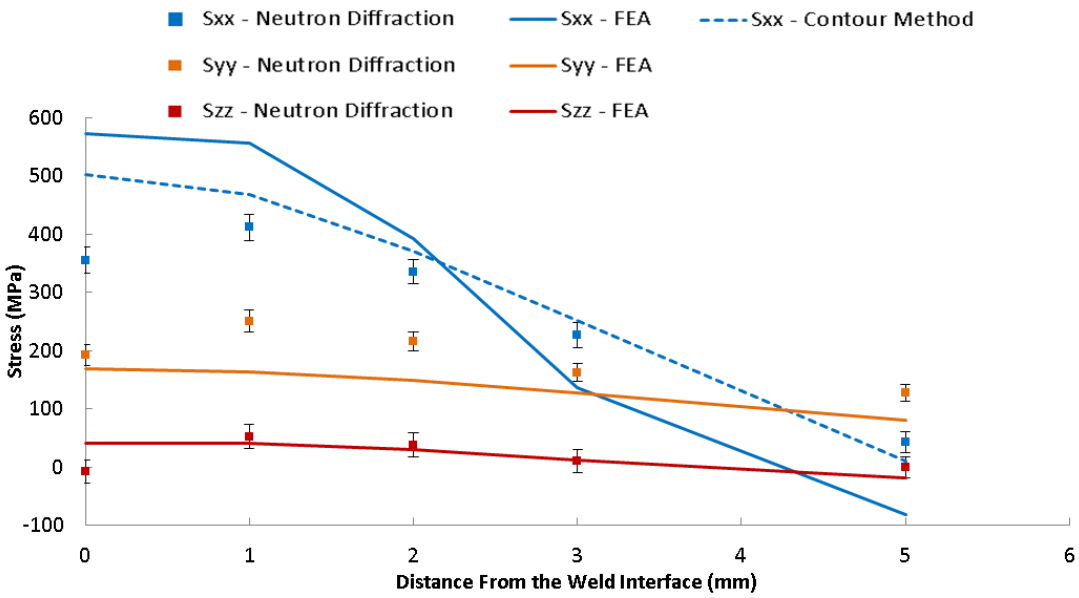

Figure 4-10: Comparison of residual stresses in weld 1, measured by neutron diffraction (after EDM cut to reduce the neutron path length), contour method and predicted numerically

4.3.2 Influence of the rubbing velocity

Numerically predicted residual stress distributions across the interface, in the three directions of space for three welding conditions, welds 1, 2 and 4 (see Table 4-1), are presented in Figure 4-11. In each case, a band of tensile residual stress can be observed at the weld interface which becomes compressive further away and then zero at the edge of the part. This stress distribution arises as a result of the thermal contraction of the band of hot material at the weld interface while being constrained by the surrounding cold material. It is worth noticing that the highest residual stress magnitude is always located in the x direction which represents both the oscillation direction and the longest direction of the weld interface. The second highest magnitude is usually found in the second direction of the weld interface *z* while the magnitude in the direction of the applied force *y* is lower. In the case of weld 1, similar residual stress peak magnitudes are obtained in the *y* and *z* directions and is believed to be a result of the combination of shallow thermal gradient and high applied pressure. The effect of the thermal gradient and applied pressure on residual stresses will be discussed in the result section.

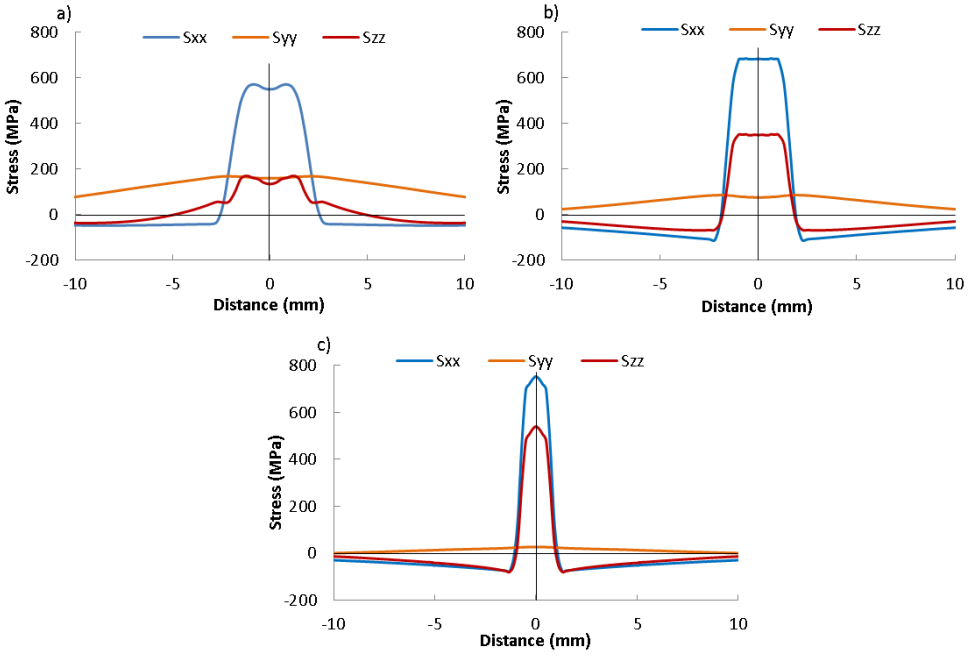

Figure 4-11: Predicted residual stress distributions in the three directions of space for: a) weld 1, b) weld 2 and c) weld 4

Contour plots of residual stress in the *x* direction obtained by numerical analysis and the contour method for the three welding conditions are displayed in Figure 4-12. Residual stress distributions are reasonably consistent between numerical model and contour method. However, the contour plots clearly show that higher residual stress magnitudes and a smaller band of tensile residual stress are numerically predicted. Although the EDM cut performed for the purpose of the contour method is supposedly purely elastic, cutting-induced plasticity could have been created[76,77] altering the original residual stress distribution and it is difficult to control. Plastic deformations are more likely to get created where residual stresses have high magnitudes, however owing to the localised stress concentration at the cutting front, plastic strains can also be induced in the far-field residual stress[76]. As a result, the contour method tends to under-predict the peak of residual stress and creates a wider distribution[45,77]. The contour method is also known to smooth out features associated with high stress gradients as a result of the filtering process used to eliminate surface roughness effects[18]. Furthermore, as investigated by Johnson[81], using variable knot spacing across the weld with the CMM, as opposed to the fixed 0.5 mm spacing used in this thesis, could improve significantly the prediction of the steep stress gradients present in LFW. As an additional way to assess the validity of the numerically predicted residual stress distributions, a comparison with experimental measurements from the literature[18,45,50,51] performed on Ti-6Al-4V LFW is provided Figure 4-13. It is worth noting that the welding conditions used to make the LFW are not revealed by the authors and are likely to influence the final residual stress field. Those experimental measurements display a good match (residual stress magnitudes and distributions) with the numerical predictions, building confidence in this modelling approach.

Figure 4-14 shows the same numerical results as Figure 4-12, however the scale was adjusted to visualise the positions of the residual stress peaks. Interestingly, both contour method and numerical model predict homogeneous residual stress over the weld interface for weld 1 condition while for weld 2 and weld 4 the areas of highest intensity are located closer the edges with a reduction at the centre. Similar residual stress distributions were reported by

Turner et al.[13] but were not discussed. To understand these distributions, it is necessary to look at the respective stress fields reached during the equilibrium phase (i.e. phase 3), when the interface force, temperature profile across the weld, burn-off rate and therefore the stress field, reach a quasi-steady state. The equilibrium stress fields, defined as the stress fields reached during the equilibrium phase, are displayed in Figure 4-15 and can be divided into three areas: the centre with low magnitude stresses because of the loss of strength of Ti-6Al-4V at high temperature; further away there is an area of highly compressive stresses where reduced temperature occurs, this area expands but is constrained by the surrounding cold material which puts it into compression and finally in the far field, an area of tensile stresses to balance the stress field in the workpiece. Overall, magnitudes of stresses in the weld zone are close to the applied pressure while a condition close to plane stress can be observed at the edges of the weld zone. Owing to shallower temperature gradient (see Figure 4-16 c)) in weld 1, lower magnitude compressive stress developed further away from the interface compared to weld 2 and weld 4, see Figure 4-15 a), b) and c). As a consequence, the equilibrium stress field at the weld interface is homogeneous resulting in a homogenous residual stress field. However, in weld 2 and weld 4 highly compressive areas are located closer to the weld interface due to their steeper temperature gradients which affect the stress field at the interface and result in higher compressive stresses at the centre of the weld compared to the edges, explaining the residual stress distributions observed in Figure 4-14.

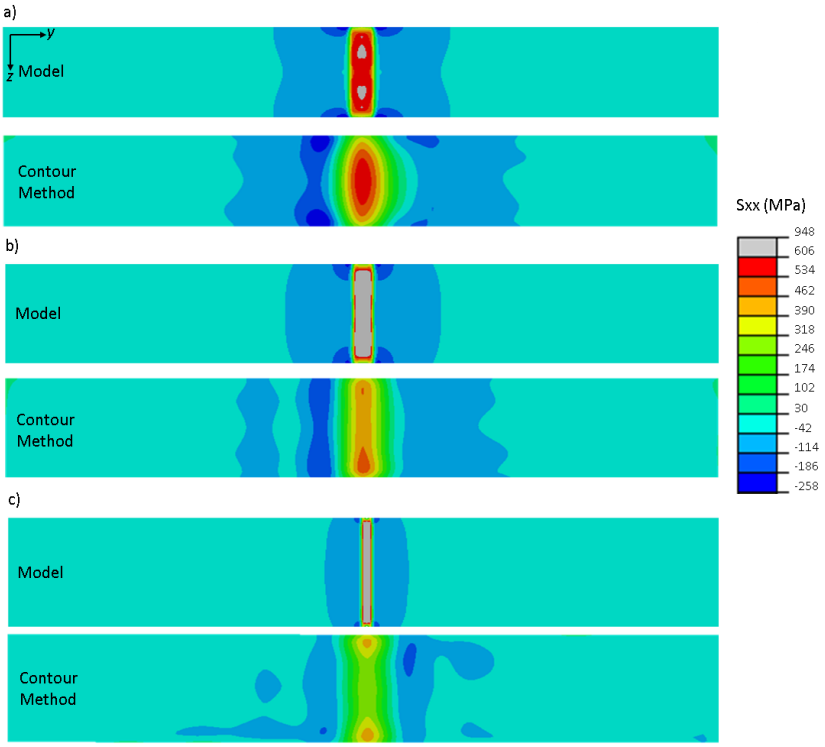

Figure 4-12: Residual stress contour plots in the x direction predicted numerically and obtained by contour method: a) weld 1 (maximum value: 625 MPa), b) weld 2 (maximum value: 804 MPa) and c) weld 4 (maximum value: 948 MPa)

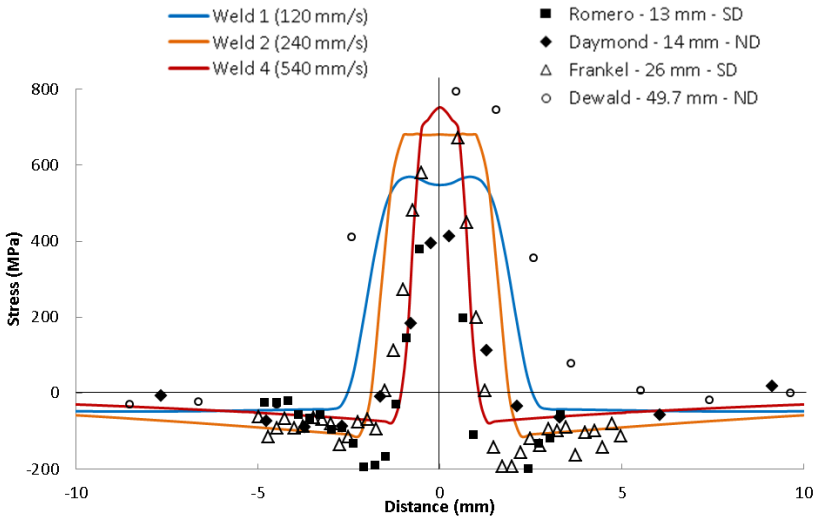

Figure 4-13: Comparison of numerically predicted residual stress in the *x* direction and data from Romero et al.[50] , Daymond et al.[51] , Frankel et al.[45] and Dewald et al.[18] measured in the longest direction of the weld interface (indicated by their respective length) within Ti-6Al-4V LFW with different techniques (ND: neutron diffraction, SD: synchrotron X-ray diffraction)

Figure 4-14: Contour plots of numerically predicted residual stress in the *x* direction: a) weld 1, b) weld 2 and c) weld 4

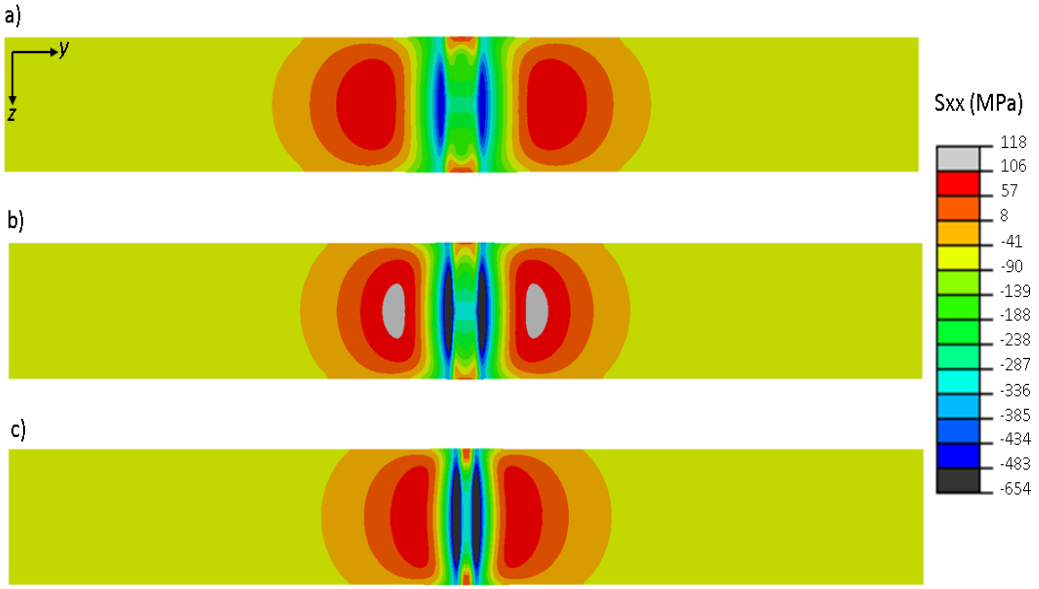

Figure 4-15: Contour plots of numerically predicted stress fields at the end of the equilibrium phase 3 in the *x* direction: a) weld 1(time elapsed: 8.14s; maximum value: 106 MPa; minimum value: -483 MPa), b) weld 2 (time elapsed: 3.15s; maximum value: 118 MPa; minimum value: -613 MPa) and c) weld 4 (time elapsed: 1.36s; maximum value: 107 MPa; minimum value: -654 MPa)

Residual stress distributions in the *x* direction extracted at mid-thickness from numerical models (Figure 4-16 a)) and contour method (Figure 4-16 b)) are plotted for comparison. Numerically, an increase in the rubbing velocity resulted in an increase in the peak of residual stress magnitude and a decrease of the size of the band of tensile residual stress. Although the increase in magnitude is not captured by the contour method measurements, the trend of the width of the band of tensile residual stress is, as shown in Figure 4-16 b). Contour method predictions of the magnitude of residual stress also contradict the trends observed by Fu et al.[14].

The effect of the rubbing velocity can be correlated with the thermal profiles obtained during the equilibrium phase 3, defined as equilibrium thermal profiles. The slopes of the equilibrium temperature profiles (shown in Figure 4-16 c)) were approximated from the gradient predicted between 0 mm and 1 mm, and are presented in Table 4-2. Weld 1 ($v_{rubbing} = 120\, mm/s$) and weld 4 ($v_{rubbing} = 540\, mm/s$) have a similar weld interface temperature (see Figure 4-16 c)) however weld 4 has a significantly steeper thermal gradient, as shown in Table 4-2. Due to the uneven heating of the structure, plastic strains are created in the weld and surrounding material. As a result of the misfit of the plastic strains, between the weld and surrounding material, elastic strains and therefore residual stresses are created[66,122]. Owing to the steep thermal gradient created with weld 4, the plastic strain misfit was enhanced and increased the peak of residual stress magnitude as well as creating a narrower band of tensile residual stress compared to a shallow thermal gradient. On the other hand, weld 4 displays a significantly cooler weld interface temperature with a steeper thermal gradient than weld 2 ($v_{rubbing} = 240\, mm/s$). Despite having a higher weld interface temperature, weld 2 developed a lower residual stress peak, implying that the residual stress peak magnitude is primarily driven by the thermal gradient. A larger band of tensile residual stress is observed for weld 2 since more heat has conducted into the workpieces due to the higher temperature and the shallower thermal gradient. As a result, more material experienced thermal contraction during the cooling.

Table 4-2: Slope of the equilibrium temperature distribution for different weld conditions

Weld	1	2	4
Slope (ºC/mm)	-127	-231	-330

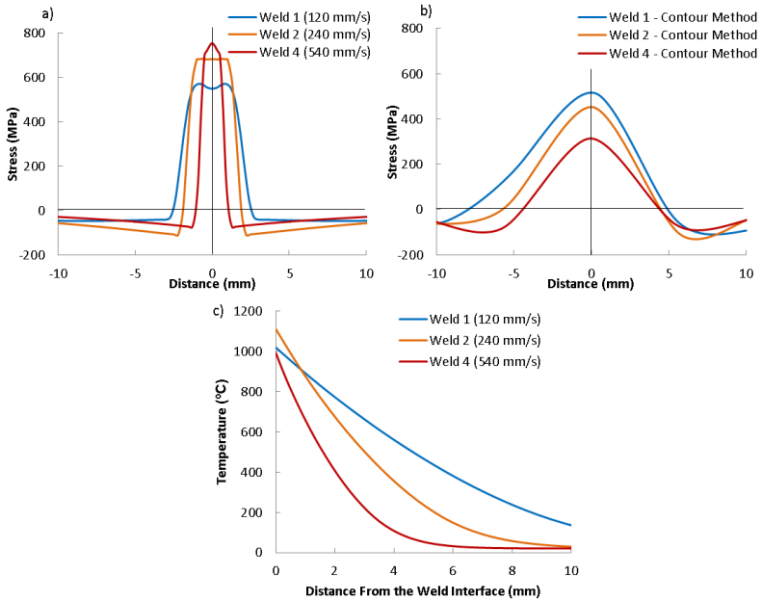

Figure 4-16: Residual stresses in the *x* direction (40 mm length of the interface) obtained after cooling by a) FEA, b) contour method and c) equilibrium temperature distributions obtained at the end of phase 3 for weld 1 (time elapsed: 8.14s), weld 2 (time elapsed: 3.15s) and weld 4 (time elapsed: 1.36s)

4.3.3 Influence of the applied force

Contour plots of residual stress in the *x* direction obtained numerically and by the contour method for the welding conditions in weld 3 and weld 4 are displayed in Figure 4-17. Figure 4-17 a) shows a similar pattern to the previous section: a higher residual stress magnitude and smaller band of tensile residual stress are numerically predicted compared to those measured using contour method. Figure 4-17 c) shows the same numerical results than Figure 4-17 a), however the original scale was kept to visualise the positions of the residual stress peaks. Figure 4-17 a) and Figure 4-17 c) display a good match when looking at the position of the peak of residual stress intensity between numerical model and contour method for weld 3. The reasons explaining the

discrepancies between numerical predictions and contour method are the same than those mentioned in the previous section.

Using an applied pressure of 90 MPa instead of 40 MPa, left the peak of residual stress magnitude unchanged and created a smaller band of tensile residual stress, as presented in Figure 4-18 a). The reduction in the size of the band of tensile residual stress was also captured by the contour method, see Figure 4-18 b). These results are consistent with those observed by Turner et al.[13] and Frankel et al.[45]. Using a higher applied pressure caused the peak temperature to reduce (see Figure 4-18 c)) for the reasons explained in the previous chapter and the thermal gradient was similar, as displayed in Table 4-3. As a result of having a similar thermal gradient, a similar peak of residual stress is created for both welding conditions. Furthermore, due to weld 4's lower interface temperature, less material experienced thermal contraction resulting in a smaller band of tensile residual stress. These findings show that similar results to the fully-coupled numerical model developed by Turner et al.[13] are achieved using this sequentially-coupled modelling approach.

Table 4-3: Slope of the equilibrium temperature distribution for different weld conditions

Weld	3	4
Slope (ºC/mm)	-329	-330

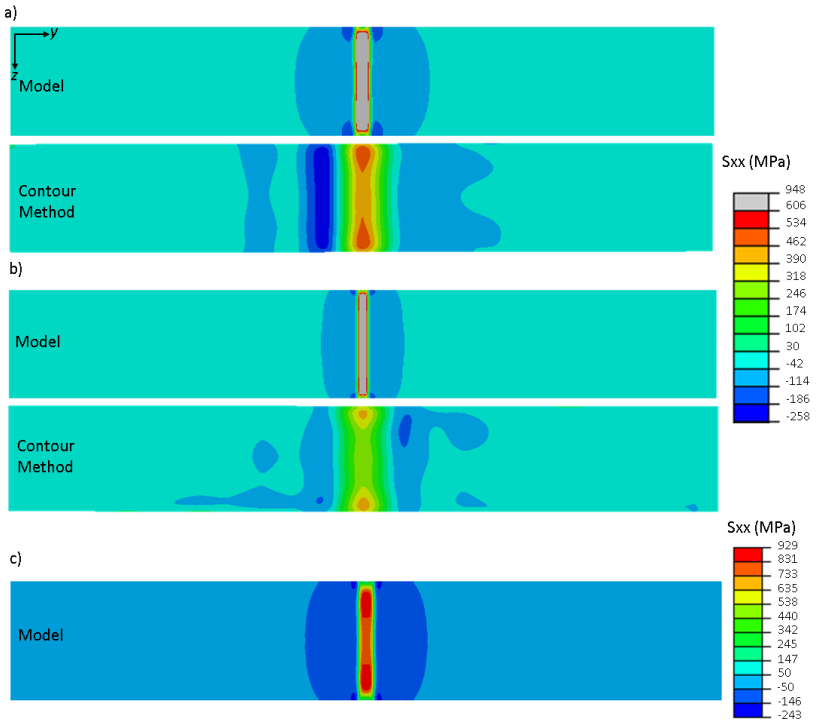

Figure 4-17: Residual stress contour plots in the x direction predicted numerically and obtained by contour method for: a) weld 3 (maximum value: 929 MPa), b) weld 4 (maximum value: 948 MPa) and c) numerically predicted contour plot of weld 3 with original scale

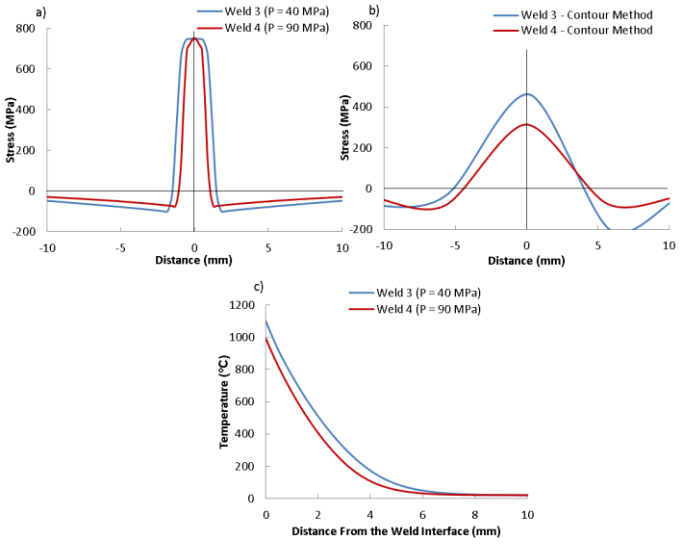

Figure 4-18: Residual stresses in the *x* direction (40 mm length of the interface) obtained by a) FEA, b) contour method and c) equilibrium temperature distributions obtained at the end of phase 3 for weld 3 (time elapsed: 1.75s) and weld 4 (time elapsed: 1.36s)

4.3.4 Influence of the oscillation direction

The residual stress distributions in the three directions of space predicted numerically for weld 5 are presented in Figure 4-19. Despite oscillating in the 20 mm weld interface direction (i.e. *z* direction) rather than the 40 mm (i.e. *x* direction), the highest residual stresses are located in the *x* direction. It can be concluded that the highest residual stress are developed in the longest direction of the weld interface irrespective of the oscillation direction.

The residual stress distributions in the *x* direction obtained for welds 4 and 5 and their associated equilibrium temperature profiles are displayed in Figure 4-20. Oscillating in the 40 mm weld interface direction with weld 4 rather than the 20 mm direction with weld 5 resulted in an equivalent peak temperature at the end of phase 3 (see Figure 4-20 b)) and a steeper thermal gradient for weld 5, see Table 4-4. Despite a higher equilibrium temperature slope value, the residual stress profile created by weld 5 is similar to weld 4. Therefore, the peak of residual stress does not increase proportionally with the magnitude of the thermal gradient in this case; more work is necessary to fully understand the development of residual stresses and their interactions with their associated equilibrium temperature profile.

Table 4-4: Slope of the equilibrium temperature distribution for different weld conditions

Weld	4	5
Slope (°C/mm)	-330	-389

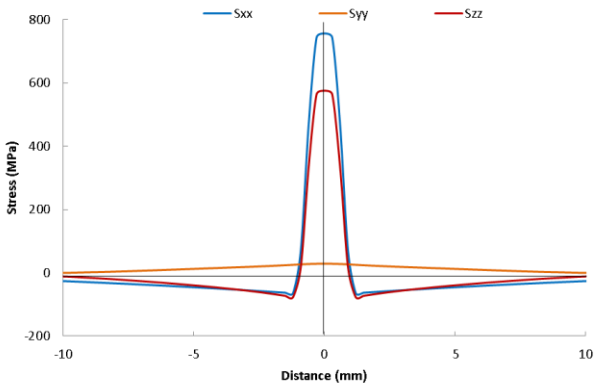

Figure 4-19: Residual stress distributions in the three directions of space predicted numerically for weld 5

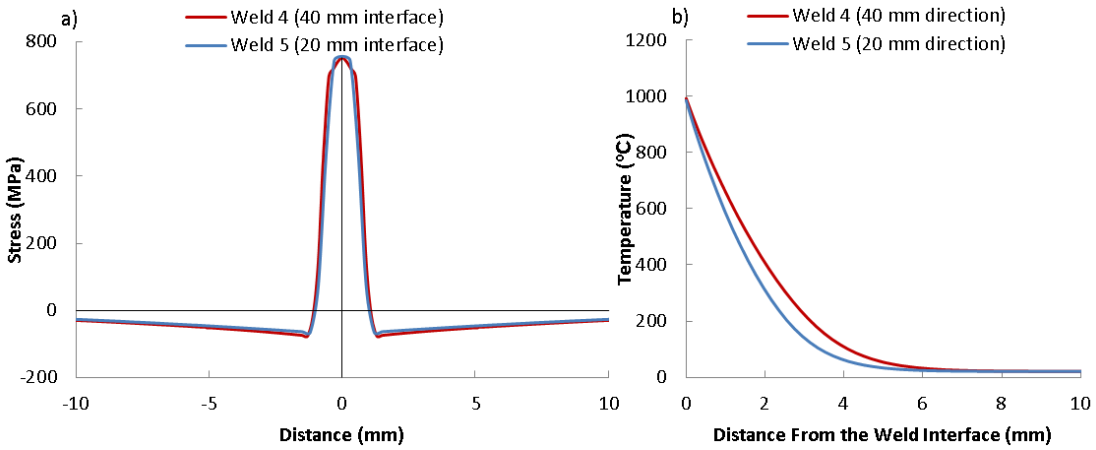

Figure 4-20: a) Residual stress in the *x* direction of welds 4 and 5 and b) equilibrium temperature distribution across the weld of welds 4 (time elapsed: 1.36s) and weld 5 (time elapsed: 1.08s) obtained at the end of phase 3

4.4 Conclusions

The key findings from this work are:

1. A reasonnable agreement was found between residual stresses numerically predicted for weld 1 and those measured using neutron diffraction and the contour method. It is worth noting that weld 1 exhibited the lowest peak and the widest residual stress distribution, making it the easiest welding condition to be experimentally measured.

2. Numerical models predicted higher peaks and narrower distributions of residual stress compared to the contour method for the other welding conditions. These discrepancies are believed to have been enhanced by cutting-induced plasticity and increased surface roughness owing to the EDM cut. Magnitudes and distributions of numerically predicted residual stresses were found to be in the same range as experimental measurements of residual stress available in the literature. Numerically, the minimum and maximum values predicted at the weld interface, are 552 MPa for weld 1 and 753 MPa for weld 4 compared to 414 MPa (Romero et al.[50]) and 794 MPa (Dewald et al.[18]), measured experimentally at the vicinity of the weld interface.

3. Numerically, increasing the rubbing velocity resulted in an increase of the peak of residual stress for the model and a narrower band of tensile residual stress. The trend of the effect of the rubbing velocity on the residual stress distribution was also captured by the contour method results. Numerically, an increase in the applied pressure did not change the peak of residual stress while narrowing the residual stress distribution; while oscillating in the 20 mm direction of the interface rather than the 40 mm direction was found to have no influence on the residual stress profile.

4. A strong correlation between the thermal profiles obtained during the equilibrium phase 3 and the residual stress field has been established. The numerical residual stress distribution was shown to be dominated by the thermal gradient of the equilibrium phase 3 temperature field. Steep thermal gradients lead to high peak values of residual stress while narrowing the band of tensile residual stress. As a secondary influence, high weld interface temperature tends to enlarge the band of tensile residual stress as a result of conducting more heat from the weld interface.

In the next chapter, an analysis of variance is conducted to determine which inputs and input interactions are statistically significant for modelling the development of residual stress.

Chapter 5: Modelling residual stress using response surface methodology

5.1 Background

Only a few authors have developed numerical models for predicting residual stresses[13,14,16,93] from LFW due to the significant computational time required to simulate the mechanical mixing occurring at the interface. Using the computationally efficient modelling approach developed in the previous chapters, which bypasses the modelling of the oscillations to predict the residual stresses, the author uses an extensive parametric study to identify those variables having the most effect on the development of residual stresses. In addition, the model will enable the development of guidelines to mitigate residual stress development.

5.2 Methodology

5.2.1 Response surface methodology

To mathematically model the relationship between the development of residual stress and different input variables, an analysis of variance (ANOVA) using response surface methodology[123,124] (RSM) was conducted with a D-optimal design using Design Expert V.7. A D-optimal design is particularly suitable when the design region is irregular[123]. Statistically insignificant input variables were removed from the regression models based on the symmetry in the results expected in the *x* and *z* directions and the following statistical criteria:

- R-Squared (R^2): A measure of the amount of variation around the mean explained by the regression model. Values greater than 90% are desirable.
- Adjusted R-Squared (Adj R^2): A measure of the amount of variation around the mean explained by the regression model, adjusted for the number of terms in the model. The adjusted R-Squared decreases as the

number of terms in the model increases if those additional terms do not add value to the model. Values greater than 90% are desirable.

- Predicted R-Squared (Prd R^2): A measure of the amount of variation in new data explained by the regression model. Prd R^2 and Adj R^2 should be within 20% of each other.
- Adequate Precision (Ad. Pr.): This is a signal to noise ratio comparing the range of the predicted values at the design points to the average prediction error. Values greater than 4 are desirable. This measure indicates if the regression model can be used to navigate the design space.
- P-Values (P-V): Each input factor has an associated P-V value which helps the user to quantify its significance where the lower the value, the better. Values equal to or lower than 0.05 are considered statistically significant.

The outputs of interest in this study are the magnitudes of the residual stresses in the three directions of space and the widths of the band of tensile residual stress in the directions of the weld interface. The author chose to define the width of the band of tensile residual stress as the distance between the points where the stress is half that predicted at the interface. The raw data used for the analysis of variance are provided in Appendix E.

5.2.2 Modelling approach

A sequentially-coupled modelling approach using the finite element code ABAQUS was used. A total of one hundred and one numerical models were created and run to complete the ANOVA conducted with Design Expert V.7. The D-optimal criteria selected a minimum number of forty one design points (i.e. forty one models), in a way that minimises the variance associated with the estimates of specified regression model coefficients. An additional sixty design points were added to the ANOVA to refine the regression models. The additional design points were also used to compare predictions made by the regression models against the FEA values, after including the FEA values to the

ANOVA. It is worth mentioning that having a large number of design points may result in over-fitting the regression models. This could have been controlled by using a subset of design points and comparing the predictions made by the regression models against the FEA predictions without including the FEA values to the ANOVA. A python script was used with ABAQUS to generate the input file for each model and a UNIX script was written to automate the computation of the one hundred and one analyses. The inputs and their range of values used to create the numerical models are given in Table 5-1 and a schematic illustration of a LFW is presented in Figure 5-1. Similar mesh and material properties to those presented in chapter 4 are used.

In previous chapters, the heat flux was applied at the interface, the workpiece was allowed to heat while material was removed to simulate axial shortening. In this work a key assumption was made, which is justified in the results section, that the development of residual stresses is determined by the thermal profile at the end of phase 3, just prior to cooling. The parametric study assumed the thermal profile has the following form at the end of phase 3:

$$T = \alpha \qquad 5\text{-}1$$

where T (ºC) is the phase 3 temperature and d (m) the distance across the weld. This equation was determined by curve-fitting the temperature profiles, at the end of the equilibrium phase 3, predicted in welds 1,2 and 4 in chapter 3.

Figure 5-2 a) demonstrates the fit between equation 5-1 and the phase 3 temperature profiles previously predicted for these welds. Equation 5-1 was used to represent various temperature distributions by varying the peak temperature coefficient α and the slope temperature coefficient β from the row data (see Appendix E). Low value of β simulate a shallow temperature gradient while increasing β steepens it. The variations of α and β are limited to the operating window presented in Figure 5-2 b) to avoid unrealistic temperature distributions and deformations, notably when large pressures are applied.

Similar to chapter 4, the hundred and one elastic-plastic mechanical models computed for the need of the ANOVA, neglect the oscillations and the expulsion of material due to the forging force. Unlike in chapter 4, the heating of the

sample from a stress free condition (at ambient temperature) was done in a single step by mapping the assumed temperature profile obtained at the end of phase 3, using equation 5-1, hence no heat flux is used. Therefore, the effect of thermally-induced expansion and contraction of the material on the stress field at the end of welding, prior to cooling, is accounted for. The sample was then allowed to cool for 100 s. After the heating step and 15 s of cooling, applied and clamping pressures were released. Finally, the model was brought to atmospheric temperature, subsequently creating the residual stress field. Hence, removal of material during processing is not modelled in this section.

Table 5-1: Input parameters

Inputs	Range
Peak Temperature Coefficient: α (°C)	879 – 1379
Slope Temperature Coefficient: β ($m^{0.8}$)	300 – 4000
Applied Pressure: P (Pa)	0 – 125 x 10^6
Interface Dimension in *x* direction: Lxx (m)	20 x 10^{-3}– 200 x 10^{-3}
Interface Dimension in *z* direction: Lzz (m)	20 x 10^{-3} – 200 x 10^{-3}
Clamping Pressure in *x* direction: Clp_Px (Pa)	0 – 125 x 10^6
Clamping Pressure in *z* direction: Clp_Pz (Pa)	0 – 125 x 10^6

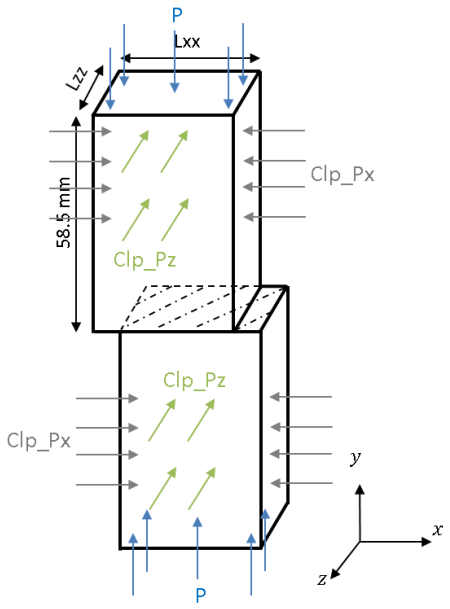

Figure 5-1: Schematic illustration of a LFW

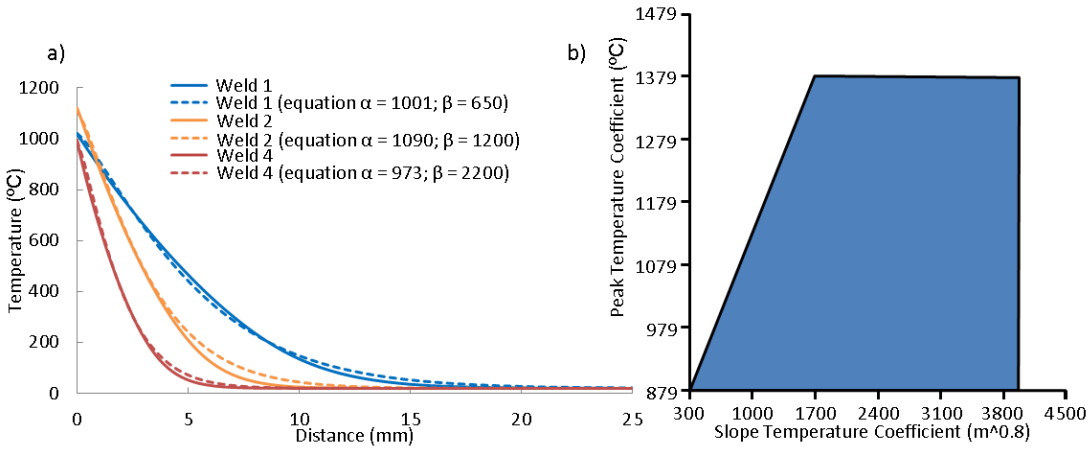

Figure 5-2: a) Comparison of phase 3 temperature profiles of welds 1, 2 and 4, predicted using the modelling approach developed in chapter 3 and their approximations with equation 5-1 with their associated coefficients and b) process input operating window

5.2.3 Modelling of shearing

The modelling approach presented in this chapter bypasses the modelling of the burn-off for the mechanical model and is a very efficient way to predict the stress field in large structures with reasonable computational times. Therefore, this approach is used to investigate the effect of shearing and assess its effect on the residual stress field. However, a small amount of movement at the end of welding, prior to cooling, is simulated to capture the effect of the shear stress on the stress field. Applied and clamping forces are included in the model.

The three previously mentioned welding conditions, weld 1, weld 2 and weld 4 are considered for the investigation. The full workpieces had to be modelled (unlike the standard model where only an eighth is considered) to simulate an oscillation. Two mechanical models were built per welding condition. For the first model, a complete oscillation using the amplitudes associated with the welding conditions (i.e. 1.5 mm for weld 1, 2 mm for weld 2 and 2.7 mm for weld 4) was simulated. It will be shown in the results section for weld 1, which has the smallest amplitude, that completing a full amplitude oscillation is not necessary, and using a 0.55 mm amplitude is sufficient to capture the effect of shearing on the stress field. Consequently, a second model was computed

using a 0.55 mm amplitude oscillation. Reduced amplitudes limit the mesh distortion and avoid re-meshing. Apart from this study, shearing is not considered in the subsequent models.

5.3 Results and discussion

5.3.1 Validation of the residual stress fields

Residual stress profiles in the *x* direction obtained using the modelling approaches presented in chapters 4 and 5 for welds 1, 2 and 4, are presented in Figure 5-3. Overall, there is a good match between the stress profiles predicted from the two modelling approaches, demonstrating that once the equilibrium temperature profile is known, modelling the burn-off on the mechanical model can be avoided, saving computational time. The small discrepancies are a result of the approximation made on the phase 3 temperature profile using equation 5-1**.**

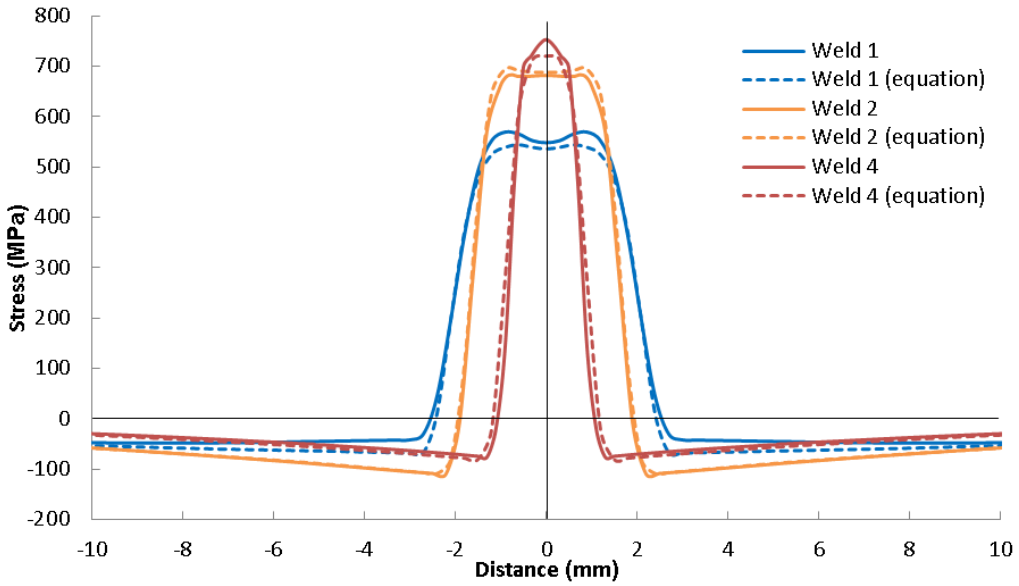

Figure 5-3: Comparison of residual stress in the *x* direction predicted using chapter 4 modelling approach (plain curves) against those obtained using the approach developed in this chapter, using equation 5-1 (dash curves)

5.3.2 Effects of shearing on the residual stress field

The maximum shear stress magnitude, normal to the z direction and along the x direction (Szx), predicted by the FEA model at mid-thickness of the weld is low (see Figure 5-4) compared to the stress in the x direction (Sxx). Therefore, the effect of shearing on the stress field is investigated in Sxx. The evolution of weld 1 stress profile in the *x* direction when different amplitude values are reached during the oscillation is presented in Figure 5-5. Shearing the hot material at the weld interface relaxes the compressive stresses by a maximum of 100 MPa for weld 1. Above an amplitude of 0.1 mm, the stress profile is not affected by the shearing. Therefore, simulating an oscillation with a maximum amplitude of 0.55 mm is sufficient to capture the effect of this on the stress field.

Residual stress profiles in the *x* direction predicted when a 0.55 mm oscillation is simulated are presented in Figure 5-6 a) and those obtained using the modelling approach presented in this chapter with no oscillation is shown in Figure 5-6 b). Accounting for the shearing has no significant effect on the width of the band of tensile residual stress however it increases the peak magnitude of the tensile residual stress by 100 MPa to 150 MPa. The increase in the peak magnitudes is due to the relaxation of the compressive stress state at the interface when shearing the hot material, as can be seen in Figure 5-7 which shows the stress profile prior to cooling for models where shearing is and is not included. Overall, the trends in the distribution and magnitude of the residual stress profiles is the same irrespective of whether the shearing is included or not.

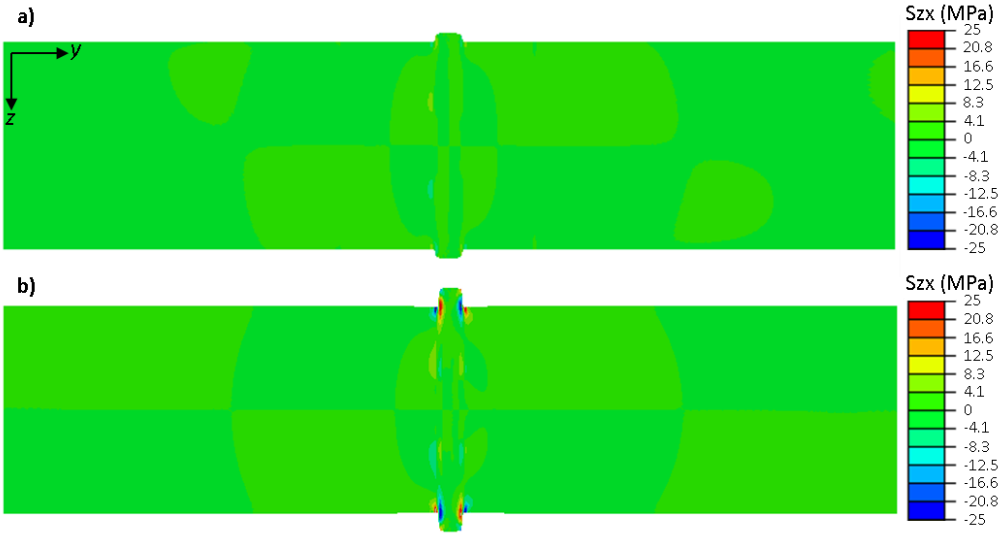

Figure 5-4: Contour plots at mid-thickness of the shear stress Szx at the end of welding (time elapsed: 8.14s), prior to cooling, after simulating an oscillation of: a) 0.55 mm and b) 1.5 mm amplitude

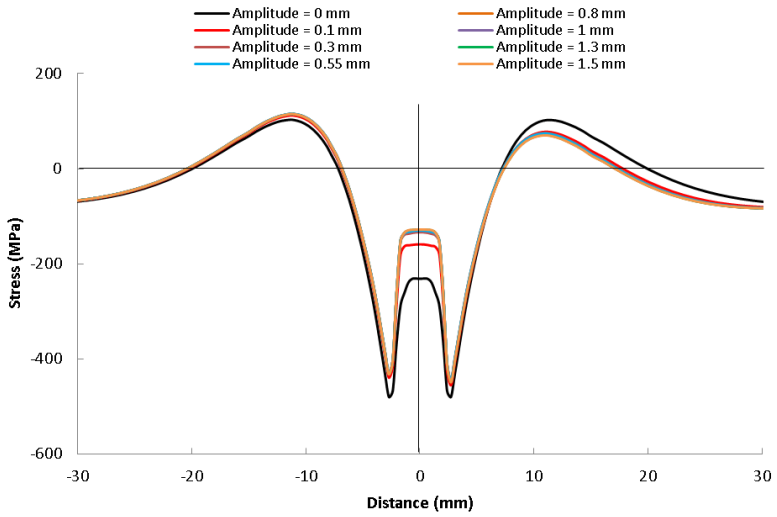

Figure 5-5: Evolution of weld 1 stress profile, extracted in the middle of the weld, in the *x* direction when different amplitude oscillations are simulated (time elapsed: 8.14s). When the amplitude is equal to 0 mm, both workpieces are aligned and at 1.5 mm, the oscillating workpiece has reached its furthest position. The stress profile relates to where the oscillating workpiece is left at its maximum displacement

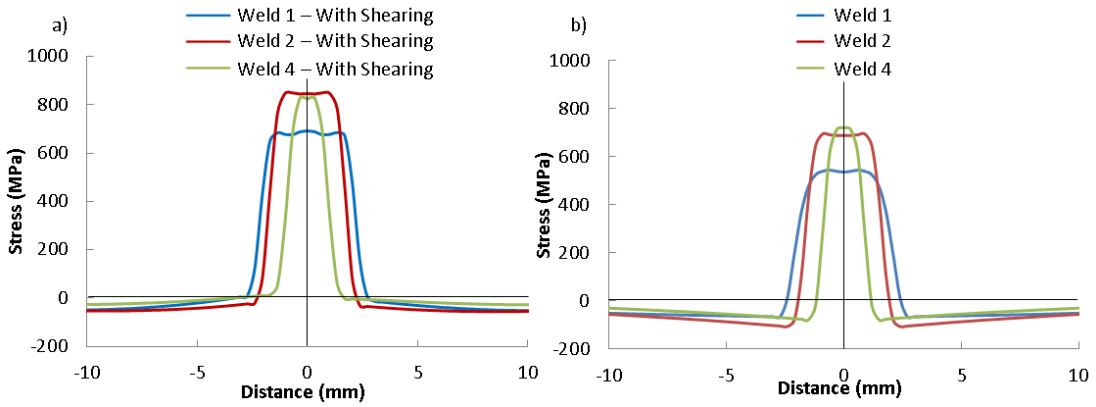

Figure 5-6: Residual stress predicted in the *x* direction for welds 1, 2 and 4 when a) a 0.55 mm shearing oscillation is simulated and b) no shearing is modelled

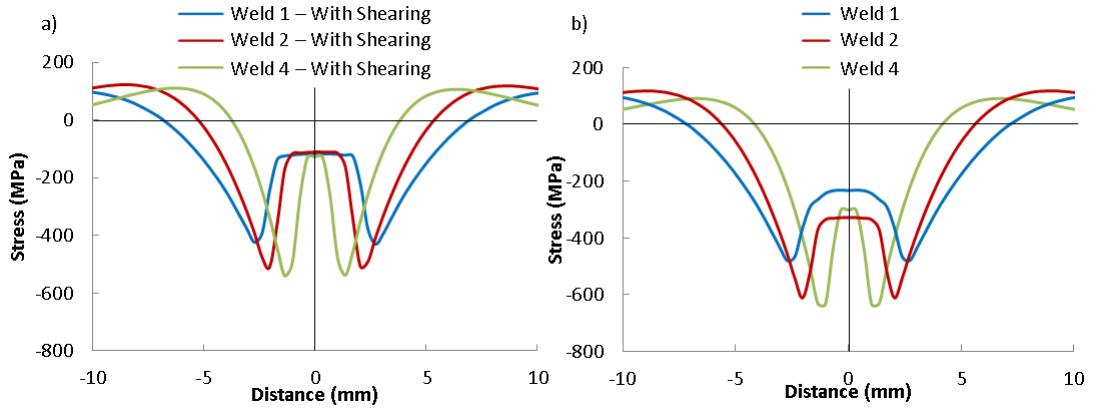

Figure 5-7: Stress profiles before cooling predicted in the *x* direction for welds 1, 2 and 4 when a) a 0.55 mm shearing oscillation is simulated and b) no shearing is modelled

5.3.3 Effects of the input parameters on the residual stress magnitude

The results of the ANOVA on the magnitude of residual stresses are given in Table 5-2. The statistical criteria shown in Table 5-2, suggest that the equations of the regression models capture the process behaviour well with lower values reached for Syy, which is due to its relative insensitivity to the input parameters. The regression models can be used to navigate the design space since the statistical criterial, Ad. Pr., indicates an adequate signal; i.e. the models are also valid in areas where no design points are present for a particular set of input values. The equations of the regression models are provided in equations 5-2 to

5-4. It is worth noting, that the regression models of the residual stress magnitudes in the three directions were found independent of the clamping pressures in the *x* and *z* directions. Because of the symmetry between Sxx and Szz, only Sxx results are presented.

Table 5-2: Statistical criteria of the ANOVA

Regression Model Equation	Equation Units	R^2 (%)	Adj. R^2 (%)	Prd. R^2 (%)	Ad. Pr.	P-V
Residual stress in the *x* direction (Sxx)	[Pa]	97	96.6	95.9	57.7	<0.0001
Residual stress in the *y* direction (Syy)	[Pa]	80.7	78.1	73.8	27.9	<0.0001
Residual stress in the *z* direction (Szz)	[Pa]	96.8	96.4	95.7	58	<0.0001

$$\boldsymbol{Sxx} = -4.08 * 10^8 + 3.29 * 10^5 * \alpha + 4.22 * 10^5 * \beta - 1.56 * \mathrm{P} + 8.4 * 10^9 * Lxx + 8.54 * 10^8 * Lzz - 91.7 * \alpha * \beta - 8.73 * 10^5 * \alpha * \mathrm{Lzz} - 7.67 * 10^5 * \beta * \mathrm{Lxx} + 5.86 * \mathrm{P} * \mathrm{Lxx} - 36.5 * \beta^2 - 2.05 * 10^{10} * Lxx^2 \quad \text{5-2}$$

$$\boldsymbol{Syy} = -4.57 * 10^8 + 6.55 * 10^5 * \alpha + 25367 * \beta - 0.218 * \mathrm{P} + 6.8 * 10^8 * Lxx + 7.12 * 10^8 * Lzz - 119 * \alpha * \beta - 8.3 * 10^5 * \alpha * \mathrm{Lxx} - 9.07 * 10^5 * \alpha * \mathrm{Lzz} + 67125 * \beta * \mathrm{Lxx} + 81933 * \beta * \mathrm{Lzz} - 1.3 * \mathrm{Lxx} * \mathrm{Lzz} + 12.7 * \beta^2 \quad \text{5-3}$$

$$\boldsymbol{Szz} = -4.25 * 10^8 + 3.76 * 10^5 * \alpha + 4.09 * 10^5 * \beta - 1.62 * \mathrm{P} + 1.11 * 10^9 * Lxx + 8.28 * 10^9 * Lzz - 99 * \alpha * \beta - 1.14 * 10^6 * \alpha * \mathrm{Lxx} - 7.43 * 10^5 * \beta * \mathrm{Lzz} + 5.78 * \mathrm{P} * \mathrm{Lzz} - 33.2 * \beta^2 - 2.02 * 10^{10} * Lzz^2 \quad \text{5-4}$$

Interaction between the equilibrium temperature slope and the peak temperature

The influence of the peak and slope temperature coefficients on Sxx is presented in Figure 5-8 a) and suggests that the slope coefficient β has a dominant effect on Sxx compared to the peak coefficient α. For β less than 3000 $m^{0.8}$, an increase in β, increases Sxx, meaning that steep phase 3 temperature profiles create high magnitude residual stress by enhancing the non-uniformity of the plastic strain distribution across the weld. Above 3000 $m^{0.8}$, the residual stress magnitude becomes largely independent of β.

For β less than 2600 $m^{0.8}$, an increase in α also increases Sxx magnitude slightly. However, when β is greater than 2600 $m^{0.8}$, increasing α tends to decrease the residual stress magnitude by a maximum of 60 MPa (reached for β = 4000 $m^{0.8}$). For very steep phase 3 temperature profiles (β > 2600), increasing the temperature will reduce the plastic strain misfit across the weld by conducting more temperature back from the weld interface and therefore reducing the magnitude of the residual stresses. To minimise the magnitude of the residual stress in the direction of the weld interface, a shallow equilibrium temperature profile is essential, while reaching low interface temperature will also help to a lesser extent. The regression model confirms the correlations between the equilibrium temperature distribution and the residual stress field observed in the previous chapter.

The influence of the peak and slope temperature coefficients on Syy is presented in Figure 5-8 b). The maximum residual stress magnitude which can be created in the direction of the applied pressure *y* is significantly lower (294 MPa) than in the direction of the weld interface (1080 MPa for Sxx). Increasing α tends to increase the magnitude of Syy while increasing the slope coefficient β results in a decrease of Syy. Unlike Sxx and Szz, steeper phase 3 temperature profiles reduce the residual stress magnitude in the direction of the applied pressure. Having a steep temperature gradient localizes the plastic deformations at the weld interface. Although this localization increases the residual stress magnitude in the direction of the weld interface, it reduces the amount of plastic misfit in the *y* direction and therefore decreases the magnitude of Syy. When high temperature slope values are reached, Figure 5-8 b) suggests that a stress-free state can be reached in the applied pressure direction.

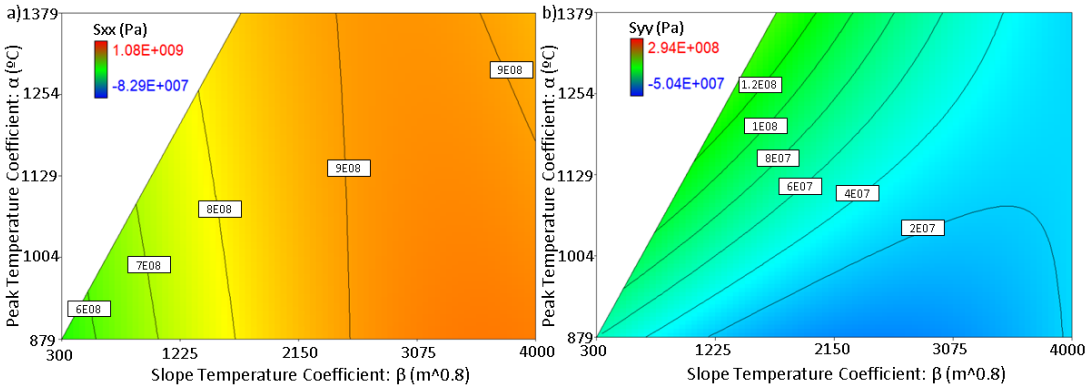

Figure 5-8: Influence of the peak and slope temperature coefficients (with P = 65E06 Pa and Lxx = Lzz = 100E-03 m) on a) Sxx and b) Syy

Interaction between the equilibrium temperature slope and the lengths of the weld interface

The interaction between the slope temperature coefficient β and the weld interface dimension Lxx on the residual stress Sxx is presented in Figure 5-9 a). Overall, an increase in Lxx results in an increase in Sxx as a consequence of having the hot material constrained by the cold material along the x direction. Therefore, larger values of Lxx produce a more restrained geometry, creating more plastic deformation misfit and producing higher residual stresses.

An artefact from the regression model caused by its polynomial formulation trying to capture the relative insensitivity of Sxx above a certain value of Lxx is visible (see FEA and regression model predictions) on Figure 5-9 a) for high value of β. Despite this statistical artefact, it can be noticed that the relative error, defined in equation 5-5, is relatively low and that the general trend predicted by the ANOVA can be trusted. Furthermore, it is interesting to see in Figure 5-9 a) that a stress free state, in the directions of the weld interface can be achieved for small dimension welds when shallow phase 3 temperature gradient are reached. This stress free state, at the centre of the weld, was also predicted numerically; i.e. design points are located in this region of Figure 5-9 a) but are not shown because different input fixed values were used for the need ot the ANOVA. It is worth noting that a long welding time would be necessary to achieve such shallow thermal gradient and LFW are often limited

to 10 s. Furthermore, long welding time are achieved with low frequency and amplitude values which increases the risk of producing a weld with defects and poor mechanical properties, according to Wanjara and Jahazi[2].

$$Relative\ error\ (\%) = \frac{(Regression\ value - FEA\ value) * 100}{FEA\ value} \qquad 5\text{-}5$$

The effects of β and the interface dimensions Lxx and Lzz on Syy are respectively presented in Figure 5-9 b) and Figure 5-9 c). Unlike the residual stresses in the direction of the weld interface, Syy is found largely independent of Lxx and Lzz since this stress is acting along the *y* direction.

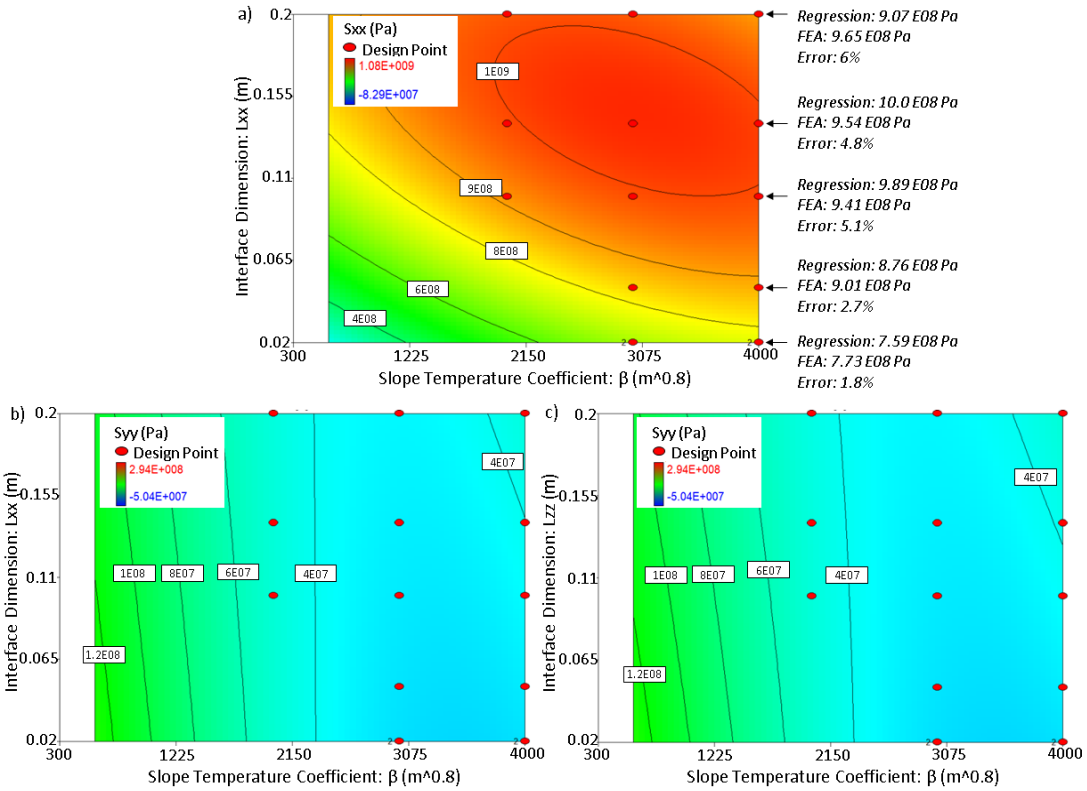

Figure 5-9: Influence of the interface dimension Lxx and slope temperature coefficients β on a) Sxx, b) Syy and influence of Lzz and β on Syy (with α = 979, P = 0 Pa and when fixed Lxx = Lzz = 20E-03 m)

Effect of the applied pressure

The evolution of Sxx's magnitude against the applied pressure for different values of Lxx is presented in Figure 5-10. Increasing the applied pressure

slightly decreases the magnitude of the residual stress. Small dimension workpieces are more affected by P with a maximum variation of Sxx of 180 MPa for Lxx equal 20 mm compared to 49 MPa for Lxx equal 200 mm.

A large magnitude applied pressure is required to significantly reduce the peak of residual stress which correlates well with Turner et al.'s[13] conclusion. When the hot material located at the interface tries to expand, it is put under compression, constrained by the cold material. Using a high applied pressure will force more material to expand laterally, in the direction of the weld interface, because of the Poisson effect and therefore will act against the thermal contraction during cooling and result in a reduction of the residual stresses subsequently created.

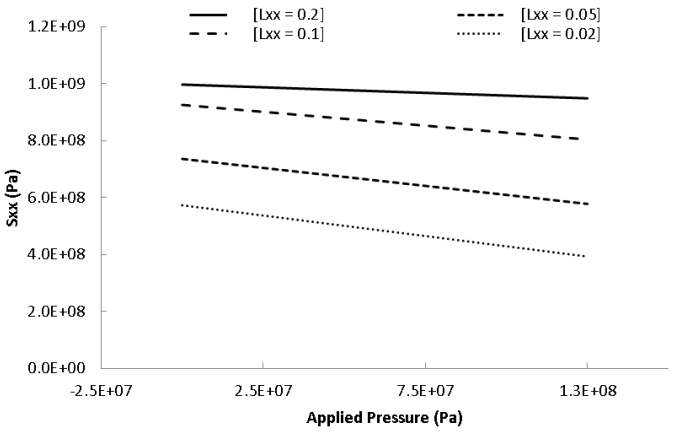

Figure 5-10: Effect of the applied pressure P (with α = 1179, β = 2000, Lzz = 100E-03 m) on Sxx

5.3.4 Effects of the input parameters on the residual stress distribution in the direction of the weld interface

The results of the ANOVA on the width of the band of tensile residual stress in the *x* and *z* directions, respectively Bdxx and Bdzz, are given in Table 5-3. The statistical criteria shown in Table 5-3 suggest that the equations of the regression models capture the process behaviour well, the regression models can be used to navigate the design space, and the equations of the regression models are listed below. Bdxx and Bdzz regression models were found

independent of the clamping pressure acting in the transverse direction to residual stress direction considered. Because of the symmetry between Bdxx and Bdzz, only Bdxx results are presented.

Table 5-3: Statistical criteria of the ANOVA

Regression Model Equation	Equation Units	R^2 (%)	Adj. R^2 (%)	Prd. R^2 (%)	Ad. Pr.	P-V
Tensile residual stress band width in the *x* direction (Bdxx)	[m]	97.1	96.7	96	54.7	<0.0001
Tensile residual stress band width in the *z* direction (Bdzz)	[m]	97.1	96.7	96.1	54.2	<0.0001

$$\boldsymbol{Bdxx} = -2.37 * 10^{-4} + 5.69 * 10^{-6} * \alpha - 1.98 * 10^{-6} * \beta - 2.32 * 10^{-12} * \mathrm{P} + 7.15 * 10^{-3} * Lxx + 5.04 * 10^{-3} * Lzz + 1.36 * 10^{-12} * Clp\_Px - 8.22 * 10^{-10} * \alpha * \beta - 1.62 * 10^{-6} * \beta * \mathrm{Lxx} - 1.17 * 10^{-6} * \beta * \mathrm{Lzz} + 4.4 * 10^{-10} * \beta^2 \quad \text{5-6}$$

$$\boldsymbol{Bdzz} = -1.75 * 10^{-4} + 5.48 * 10^{-6} * \alpha - 1.92 * 10^{-6} * \beta - 2.38 * 10^{-12} * \mathrm{P} + 3.99 * 10^{-3} * Lxx + 8.43 * 10^{-3} * Lzz + 1.65 * 10^{-12} * Clp\_Pz - 7.56 * 10^{-10} * \alpha * \beta - 8.75 * 10^{-7} * \beta * \mathrm{Lxx} - 2.02 * 10^{-6} * \beta * \mathrm{Lzz} + 4.18 * 10^{-10} * \beta^2 \quad \text{5-7}$$

Interaction between the equilibrium temperature slope and the peak temperature

The influence of the peak and slope temperature coefficients on the width of the band of tensile residual stress developed in the *x* direction Bdxx, is presented in Figure 5-11. When increasing β, i.e. having a steeper phase 3 temperature profile, Bdxx can decrease under a millimetre wide while increasing α tends to increase Bdxx. Having a steep phase 3 thermal gradient constrains the heat and therefore the plastic deformation close to the weld interface, resulting in narrow band of tensile residual stress. On the other hand, high peak temperature conducts more heat back from the interface, therefore creating plastic strains further away from the weld interface and expanding Bdxx. When the coefficient β is under about 1800 $m^{0.8}$, it has a dominant influence on Bdxx, however above 2800 $m^{0.8}$, very little change is recorded in Bdxx value when increasing β and α plays a more significant role on Bdxx value.

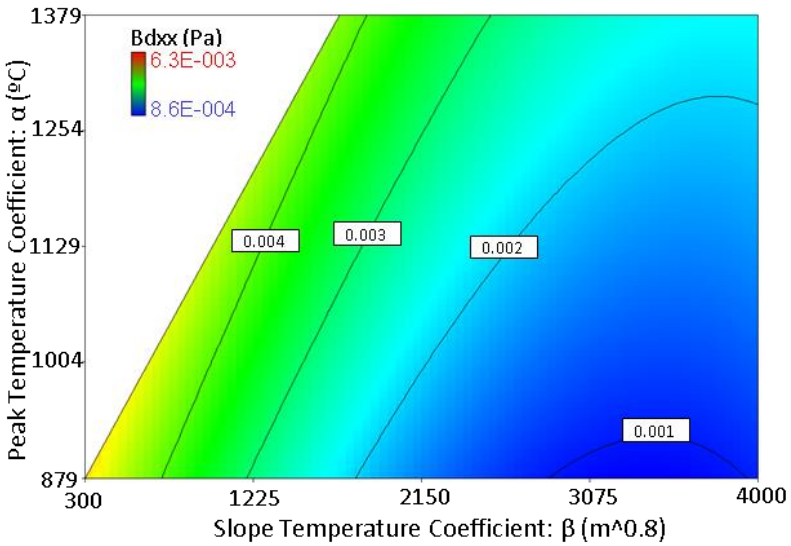

Figure 5-11: Influence of the peak and slope temperature coefficients on Bdxx (with P = 65E06 Pa and Lxx = Lzz = 100E-03 m)

Interaction between the equilibrium temperature slope and the lengths of the weld interface

The effects of the weld interface dimensions Lxx and Lzz on Bdxx are presented in Figure 5-12 a) and b) respectively. Unlike the residual stress magnitude Sxx, the interface dimensions have a small influence on Bdxx compared to β. Increasing either Lxx or Lzz results in an increase in Bdxx because larger values of interface dimensions produce a more restrained geometry, creating more plastic deformationmisfit. It is worth noticing that even for a large structure, a narrow band of tensile residual stress can be achieved with the appropriate phase 3 temperature distribution. Above β values of 2800 $m^{0.8}$, the model suggests that Bdxx becomes insensitive to β and the weld interface dimensions.

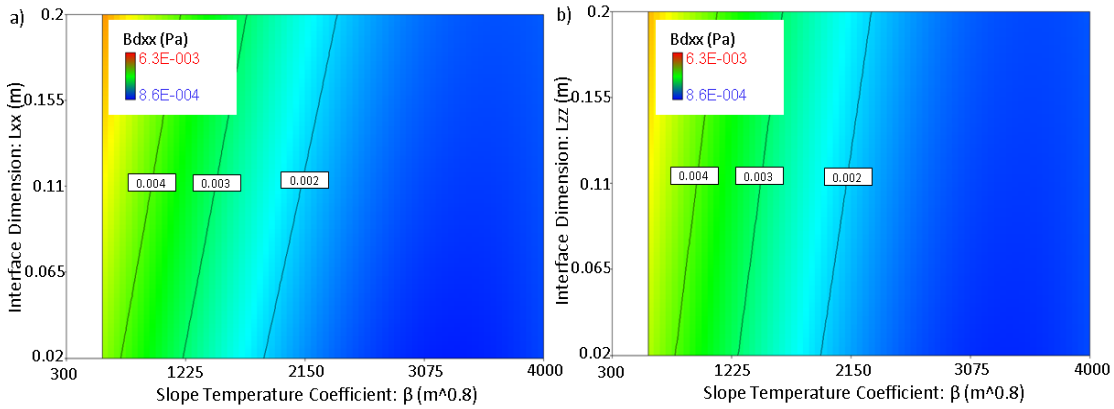

Figure 5-12: Influence of the slope temperature coefficient and interface dimension a) Lxx and b) Lzz on Bdxx (with P = 65E06 Pa and Lxx = Lzz = 100E-03 m)

Effect of the applied pressure and clamping pressure

The evolution of the band of tensile residual stress Bdxx against the applied pressure and the clamping pressure is presented in Figure 5-13. An increase in the applied pressure results in a decrease of Bdxx while increasing the clamping pressure has the opposite effect. Overall, applied and clamping pressures have a small influence on Bdxx with a respective maximum variation of 0.29 mm and 0.17 mm. As previously explained, the applied pressure acts against the thermal contraction occurring during the cooling phase. In contrast, the clamping pressure will act along with the thermal contraction in the direction of the weld interface, enhancing the plastic deformation misfit between the hot and cold material and therefore increasing the distribution of residual stresses. Therefore, to minimize the residual stress, it is preferable to use a high magnitude applied pressure with a minimal clamping pressure. However, it is worth noting that the clamping pressure needs to be adequate to hold the workpieces in position while welding to prevent them from wobbling inside the chucks.

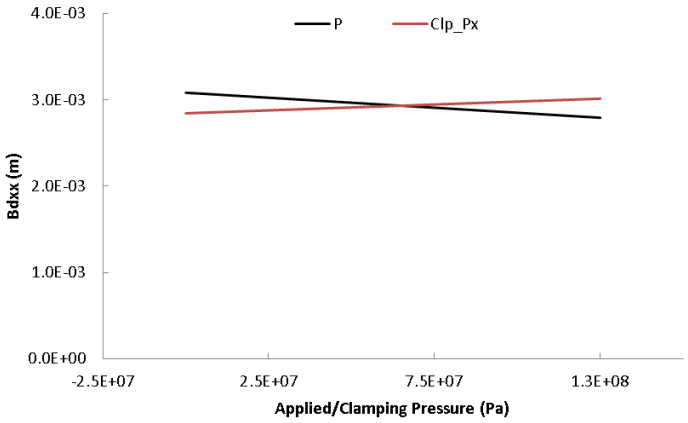

Figure 5-13: Effect of the applied pressure P and clamping pressure Clp_Px (with α = 1179, β = 2000, Lxx = Lzz = 100E-03 m and when fixed P = Clp_Px = 65E06 Pa) on Bdxx

5.4 Conclusions

The key findings from this work are:

1. Models based on the peak temperature provide an accurate prediction of the calculated as-welded residual stress without modelling the removal of material; with a maximum discrepancy of 33 MPa found for weld 4, at the weld interface, between the two modelling methods. Furthermore, ignoring the shearing that occurred during processing resulted in a small under prediction of the as-welded residual stress.

2. The clamping pressure was found to have no significant effect on the residual stress magnitude or on the width of the band of tensile residual stress. On the other hand, the applied pressure slightly reduced the magnitude of the residual stresses and narrowed its distribution.

3. The thermal gradient of the phase 3 temperature profile and the length of the weld interface were the most influential parameters that affected the residual stress magnitude in the direction of the weld interface. The phase 3 interface peak temperature played a minor role. Finally, the width of the band of tensile residual stress was mainly affected by the thermal gradient.

4. To minimise the residual stress magnitude developed in the weld interface direction, the phase 3 temperature distribution should have a low interface peak temperature with a shallow gradient and small weld interface dimensions. A shallow thermal gradient is associated with long, slow welds and will create a large band of tensile residual stress. If the appropriate conditions are used, the regression model suggests that is possible to create a stress-free LFW.

5. The residual stress magnitude developed in the direction of the applied pressure is strongly influenced by the peak and slope of the phase 3 temperature profile while it was found largely independent of the weld interface dimensions. Unlike the residual stress developed in the direction of the weld interface, having a steep thermal gradient reduced the magnitude of the residual stress in the direction of the applied pressure. Therefore, trying to reduce the magnitude of the residual stress Sxx and Szz by having a shallower thermal gradient will increase Syy. However, the maximum magnitude of Syy was significantly lower than either Sxx or Szz.

In the next chapter, the modelling approach developed in this thesis is applied to a linear friction weld with a bladed-disk joint geometry. The distribution and magnitude of the residual stress developed are analysed.

Chapter 6: Modelling of a blisk like linear friction weld and experiments

6.1 Background

The current main industrial application of LFW is the bladed-disk. To the best knowledge of the author, only Sorina-Müller et al.[36] modelled a titanium alloy blisk LFW, using a friction coefficient to account for the heat generation. Numerically, temperatures as low as 200ºC were calculated at the weld interface once the desired upset was reached (prior to cooling) and no residual stresses were predicted. These results are not consistent with most numerical models and experimental measurements that predict temperature history on rectangular LFW[5,9,13,106]. Consequently, more research is needed to understand the development of residual stresses in real engineering structures. Using the computationally efficient modelling approach developed in the previous chapters, which bypasses the modelling of the oscillations, the author aims to investigate the development of residual stress within a blisk LFW and its mitigation by post-weld heat treatment.

6.2 Methodology

6.2.1 Experiments

Ti-6Al-4V linear friction welds were made in collaboration with KUKA Systems Birmingham using the E130 machine for the two sets of welding parameters listed in Table 6-1. The welding trial was conducted by a KUKA Systems engineer; under the guidance of the author. Each set of parameters were replicated twice to account for experimental variability. Photos of the workpiece held in the tooling of the LFW machine, before and after welding are presented in Figure 6-1. The geometry and the position of the weld interface of the workpiece used for the experiments are illustrated in Figure 6-2 a). The Ti-6Al-4V parent material had a bimodal alpha-beta microstructure. Experimentally the workpiece was oscillated in the *x* direction. Finally, contour measurements were

provided as an external service by HILL Engineering on welds 1 and 3 to measure the residual stress in the *x* direction at the middle of the weld and to investigate the effect of both sets of welding parameters.

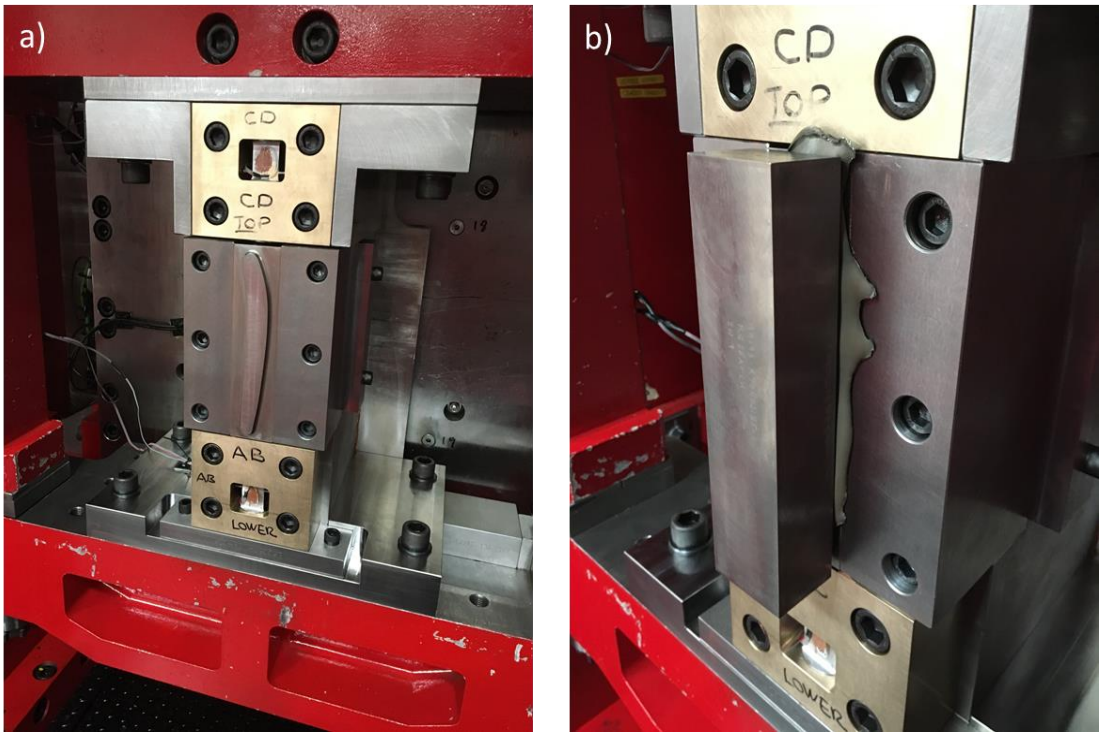

Figure 6-1: Workpiece inside the tooling of the LFW machine a) before and b) after welding

Table 6-1: Welding parameters

Weld	Freq. (Hz)	Amp. (mm)	Applied Pressure (MPa)	Burn-off (mm)	Rubbing Velocity (mm/s)
1;2	35	2.5	106	3.6	350
3;4	20	2.5	106	3.6	200

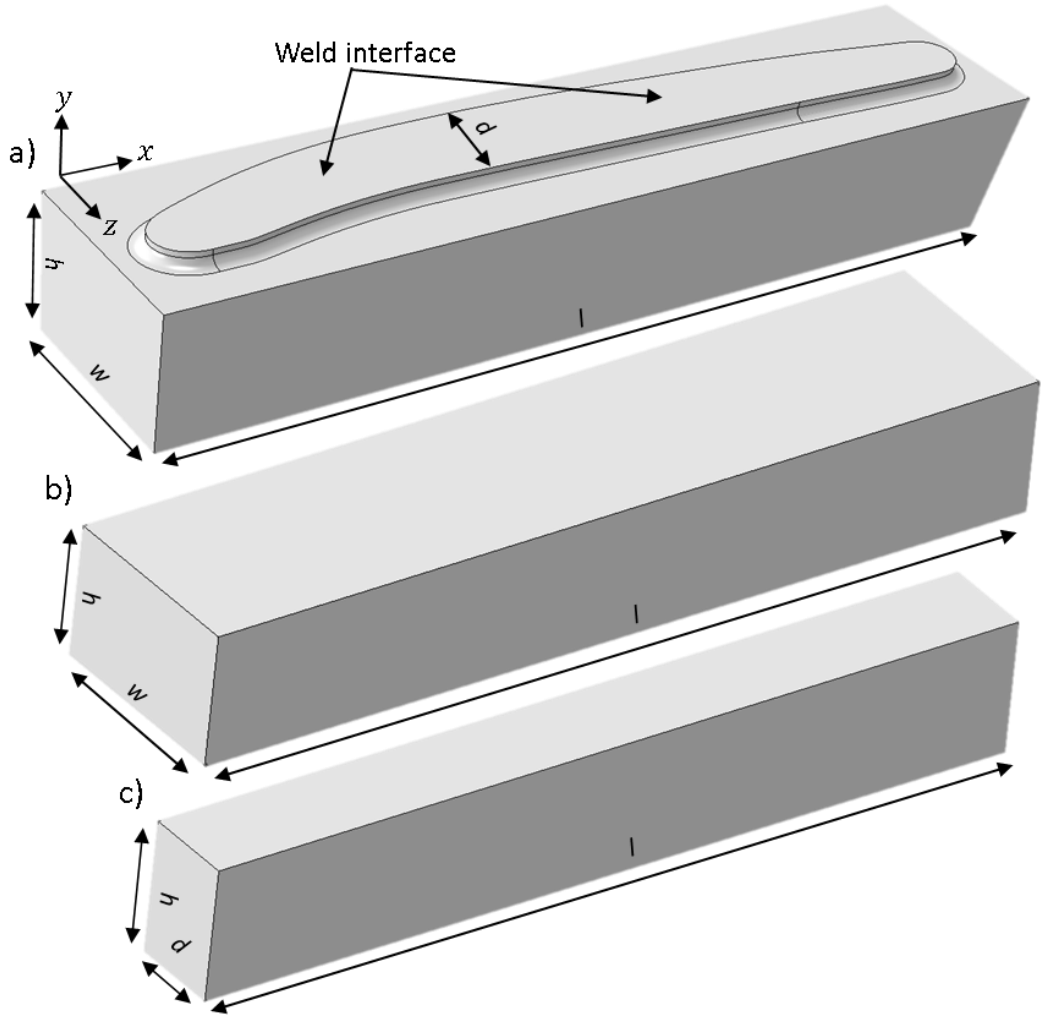

Figure 6-2: Isometric views of a) the blisk like geometry and rectangular geometries simulated in this chapter b) rectangular 1 and c) rectangular 2

6.2.2 Modelling approach

The sequentially-coupled modelling approach developed in chapter 3 (thermal modelling) and chapter 4 (mechanical modelling) was used with the same material properties. A fine element length of 0.3 mm was used across the weld interface and its vicinity which then coarsened to 3 mm, as shown in Figure 6-3. The elements are predominantly hexahedral, particularly near the weld interface with some tetrahedral elements being used further away to allow coarsening of the mesh.

Using the approach presented in chapter 3 to post-process the machine data obtained from the welding trials, the average power of phase 3 and burn-off rate for each weld were extracted, see Table 6-2. The repeatability of the experiments was reasonable, with misalignments of the weld interfaces of the workpieces being responsible for the discrepancies in the results, notably between weld 1 and 2 power. Numerical models were created for welds 1 and 3 and were compared with the contour method measurements.

Additional models were computed using the two rectangular geometries presented in Figure 6-2 a) and b). To calculate the residual stress profiles, the equilibrium temperature profiles obtained from the blisk welds 1 and 3 thermal models were mapped on the rectangular models, following the modelling approach developed in chapter 5. This study aimed to analyse the effect of the blisk like geometry compared to a rectangular block.

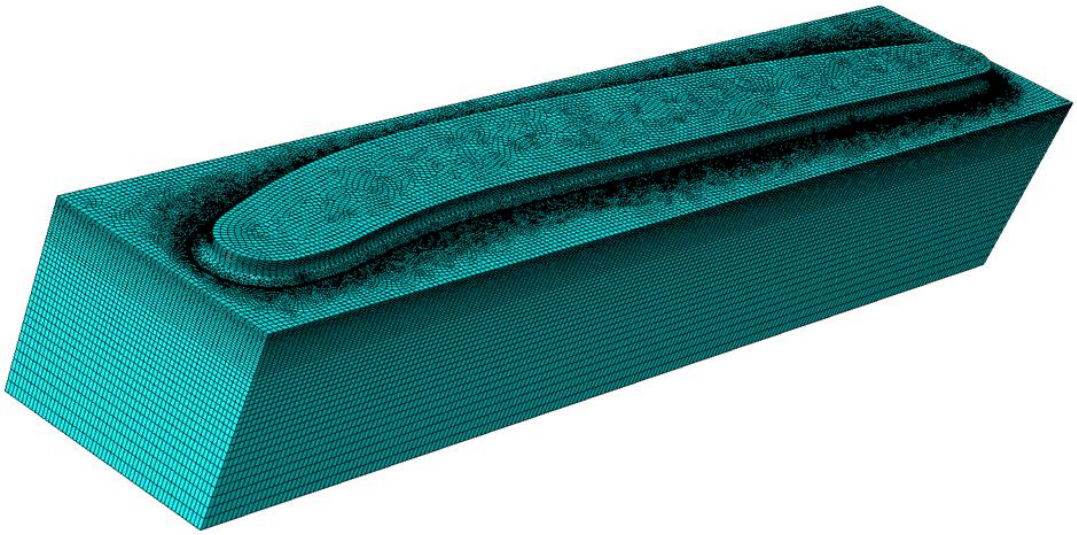

Figure 6-3: Blisk like mesh

Table 6-2: Equilibrium power and burn-off rate from the experimental conditions in Table 6-1

Weld	Average Phase 3 Power (kW)	Average Phase 3 Burn-off Rate (mm/s)
1	14.89	2.50
2	12.66	2.59
3	5.45	1.65
4	5.61	1.70

6.2.3 Post-weld heat treatment modelling

Three post-weld heat treatment (PWHT) cycles are simulated for welds 1 and 3, from Table 6-1. The sample was heated to a holding temperature in one hour and then held for a certain duration before cooling down to ambient temperature in one hour. The holding temperatures and times for the different PWHT cycles are presented in Table 6-3. Creep data were added to the previous set of material properties. A strain-hardening version of the power-law creep model proposed in ABAQUS, see equation 6-1, was used to fit the experimental data from Badea et al.[125]. This power-law is suitable under a fluctuating stress-state[126] as is the case with these specimens.

$$\dot{\bar{\varepsilon}}^{cr} = (\mathrm{A} * \bar{q}^{n} * [(m+1) * \bar{\varepsilon}^{cr}]^{m})^{\frac{1}{m+1}} \qquad 6\text{-}1$$

where $\dot{\bar{\varepsilon}}^{cr}$ is the uniaxial creep strain rate, $\bar{\varepsilon}^{cr}$ is the equivalent creep strain, $\bar{q}$ the Mises equivalent stress for isotropic material, t the time, A, n and m are functions of the temperature and are determined by experiments.

Figure 6-4 displays the experimental data measured by Badea et al.[125] fitted with a power-law and the values of A and n for different temperatures. The coefficient m was chosen equal to zero because only the secondary creep strain was modelled. Experimental measurements from Badea et al.[125] showed that the primary creep strain was limited compared to the secondary and tertiary, and the tertiary creep strain only occurred close to the rupture of the material.

Table 6-3: Holding temperature and holding time for the three PWHT cycles simulated

Cycle	Holding Temperature (°C)	Holding Time (h)
1	565	3
2	565	6
3	665	3

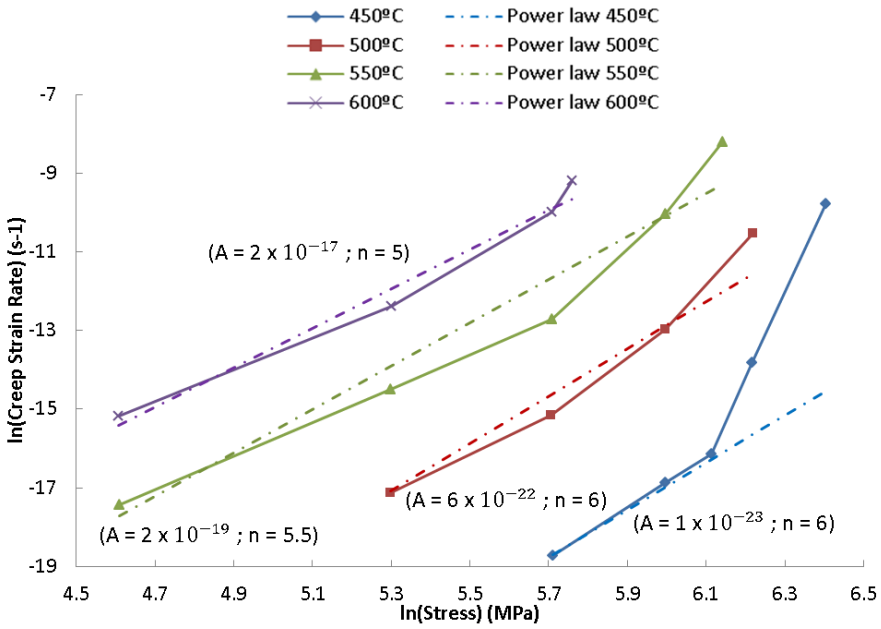

Figure 6-4: Creep data from Badea et al.[125] (plain lines) fitted with a power-law (dash lines) with its associated coefficients A and n

6.3 Results and discussion

6.3.1 Comparison of residual stresses predicted numerically against contour method measurements

Contour plots of residual stress in the *x* direction, at the middle of the weld, numerically predicted and measured by the contour method are displayed for weld 1 and weld 3 respectively in Figure 6-5 a) and b). Overall, numerical predictions and contour method measurements are in a reasonable agreement. Strong tensile residual stress developed at the weld interface and its vicinity. Higher magnitudes and smaller distributions of residual stress are numerically predicted compared to those measured with the contour method for the reasons detailed in chapter 4. Minimal differences in the residual stress profiles are exhibited between both contour method results. Furthermore unlike the contour method, numerical results display a reduction in the magnitude of the residual stress close to the edges of the weld interface. This a consequence of the physical presence of the flash on the blisk like welds used for contour method. Indeed, in chapter 4, the flash was removed prior to experimental measurement

on the rectangular welds and a clear reduction of the residual stress magnitudes is recorded close to the edges measured by the contour method technique.

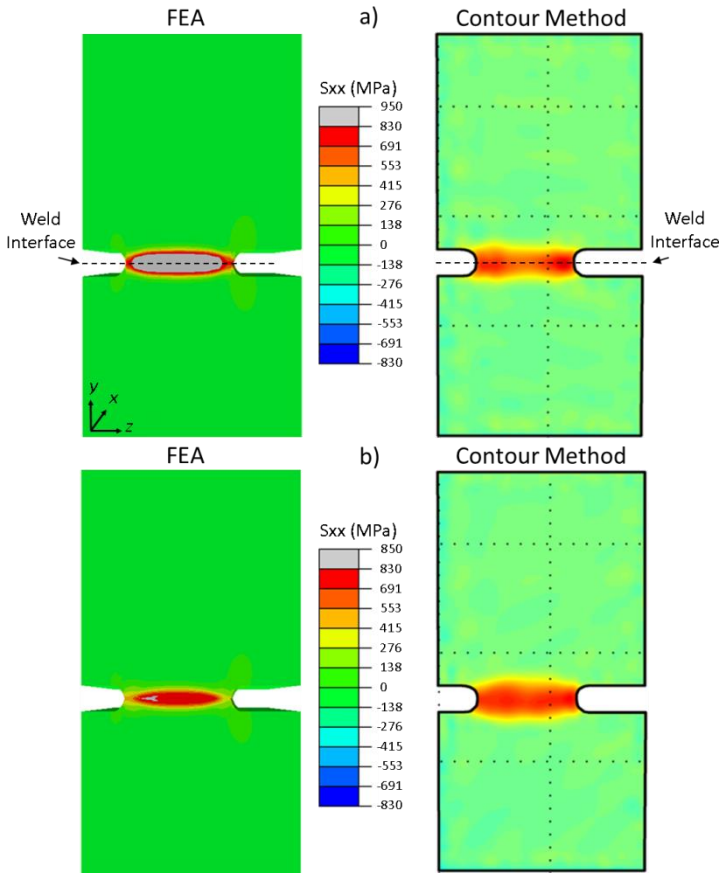

Figure 6-5: Residual stress contour plots in the x direction predicted numerically and measured by contour method for a) weld 1 and b) weld 3

6.3.2 Residual stress prediction within blisk like geometry joints

The residual stress distributions in the three directions of space across the weld, extracted at the middle of the weld, for both blisk like geometry welds are presented in Figure 6-6. Similar to the rectangular coupons in the previous chapters, the highest residual stress magnitudes developed in the longest direction of the weld interface *x*, the second highest in the second direction of the weld interface *z* and negligible residual stresses in the direction of the applied pressure *y*. Interestingly, an increase in the residual stress magnitude further away from the weld interface is recorded for weld 1, see Figure 6-6 a),

before decreasing. This is believed to be a combined effect of the weld interface geometry and equilibrium temperature profile slowing down the conduction of the heat back to the cold material and stress relieving the residual stresses at the weld joint.

Overall, there are small differences between the numerically predicted residual stress profiles of welds 1 and 3, as shown in Figure 6-7 a) which matches well with the trend previously observed in the contour method results. Numerically, higher magnitude residual stresses were obtained for weld 1 condition compared to weld 3, as shown in Figure 6-7 a). Having a reduced input welding frequency for weld 3 decreased the burn-off rate as shown in Table 6-2 resulting in a shallower temperature gradient for the equilibrium temperature profile, see Figure 6-7 b). Like the rectangular coupons, a shallow temperature profile reduced the plastic strain misfit across the weld, lowering the magnitude of the residual stresses created. Furthermore, it is worth noting that reducing the input welding frequency from 35 Hz to 20 Hz resulted in a large reduction of the weld interface temperature, as shown in Figure 6-7 b), due to the decrease in the equilibrium phase 3 power magnitude and the longer welding time involved, generating more heat losses by conduction.

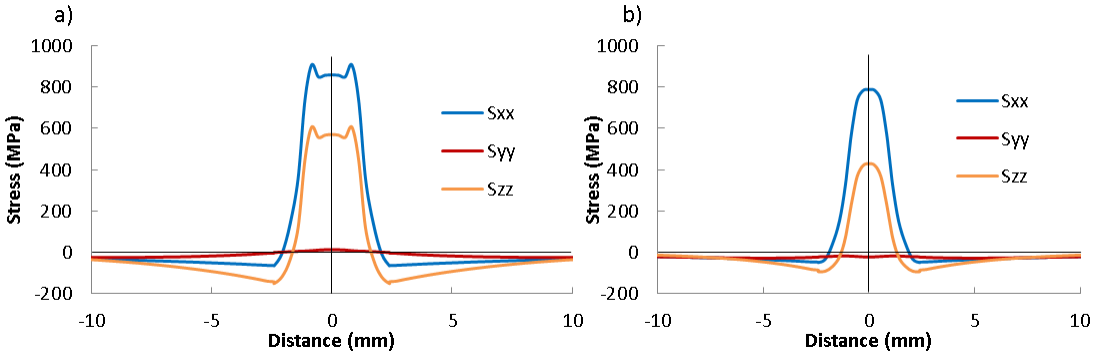

Figure 6-6: Residual stresses predicted in the three directions of space for the blisk like geometry joints a) weld 1 and b) weld 3

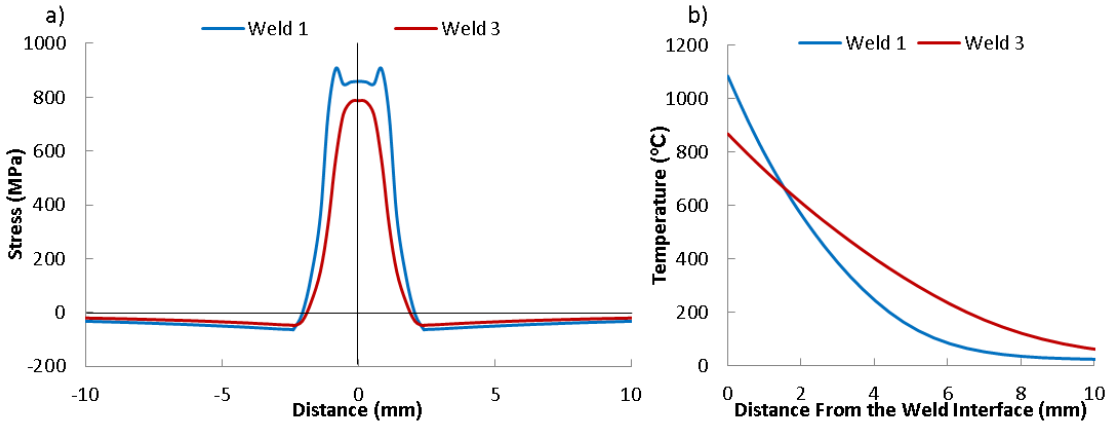

Figure 6-7: a) Residual stress profiles in the x direction for both welding conditions and b) their associated equilibrium temperature profiles

6.3.3 Effect of the blisk like geometry on residual stresses

Section views of the residual stress distribution in the *x* direction for the blisk model and rectangular models 1 and 2 using the sets of welding parameters welds 1 and 3 (see Table 6-1), are respectively presented in Figure 6-8 a) and b). The highest magnitudes are located close to the edges with reduced residual stress magnitudes at the centre of the welds. During heating, the edges can expand more freely unlike the centre of the weld, resulting in significantly lower compressive stresses which will subsequently counteract the development of tensile residual stress to a lesser extent. Interestingly, distributions on the blisk like geometry coupon and on the rectangular models display similar features. However, higher peak residual stress magnitudes developed for the rectangular models due to their larger weld interface areas.

Residual stress profiles in the three directions of space extracted at mid thickness from the blisk like model and rectangular models 1 and 2 for the welding conditions weld 1 and weld 3 are respectively presented in Figure 6-9 a) and Figure 6-9 b). Residual stress profiles in the *x* direction are similar between the blisk and rectangular models; however differences arise in the *z* direction as a consequence of the reduced dimension of the blisk interface along that axis and the curvature of its geometry. Owing to its reduced weld interface dimension in the *z* direction, the model rectangular 2 model developed

lower magnitude residual stress compared to the model rectangular 1 in that direction. The residual stress peaks developed by the blisk models in the z direction are positioned approximately half way between those predicted for the models rectangular 1 and 2. To conclude, using a rectangular coupon with the modelling approach developed in chapter 5 offers a good insight into the magnitude and distribution of residual stress profiles created by the welding process.

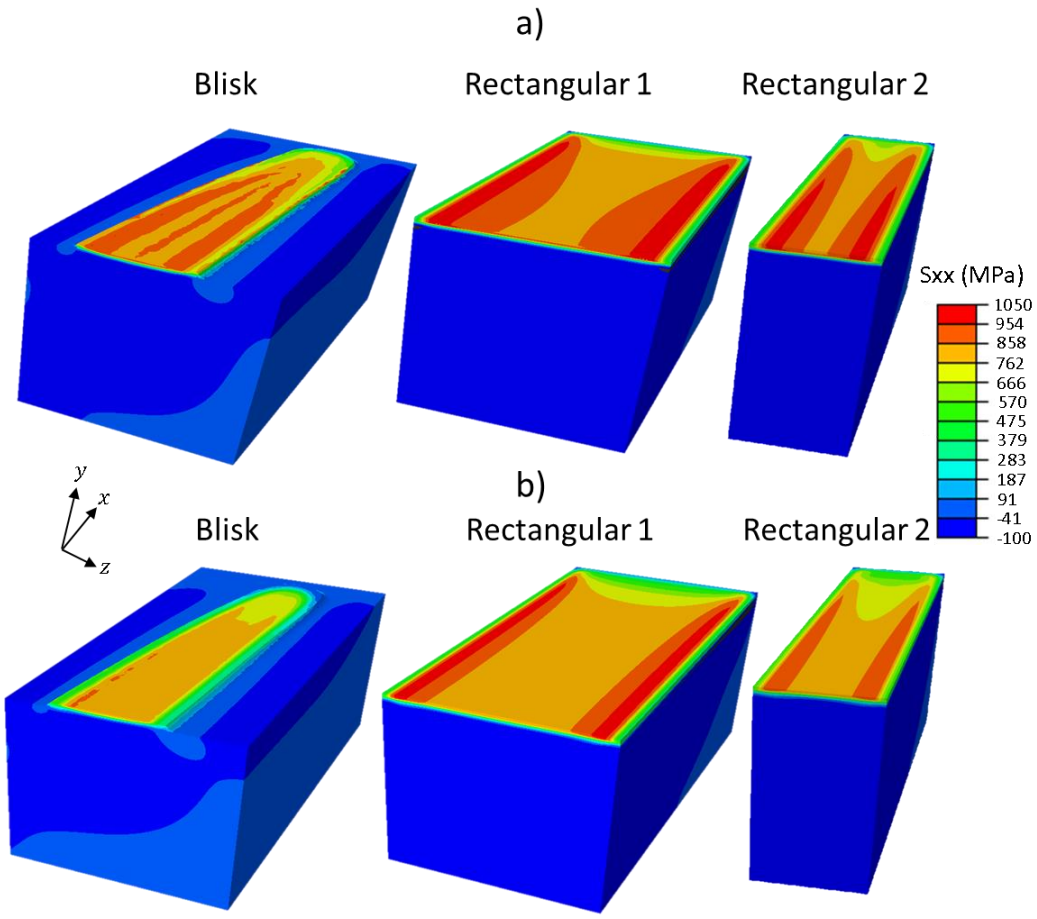

Figure 6-8: Section views of the residual stress in the *x* direction for the blisk and rectangular 1 and 2 models, using the welding conditions of a) weld 1 and b) weld 3

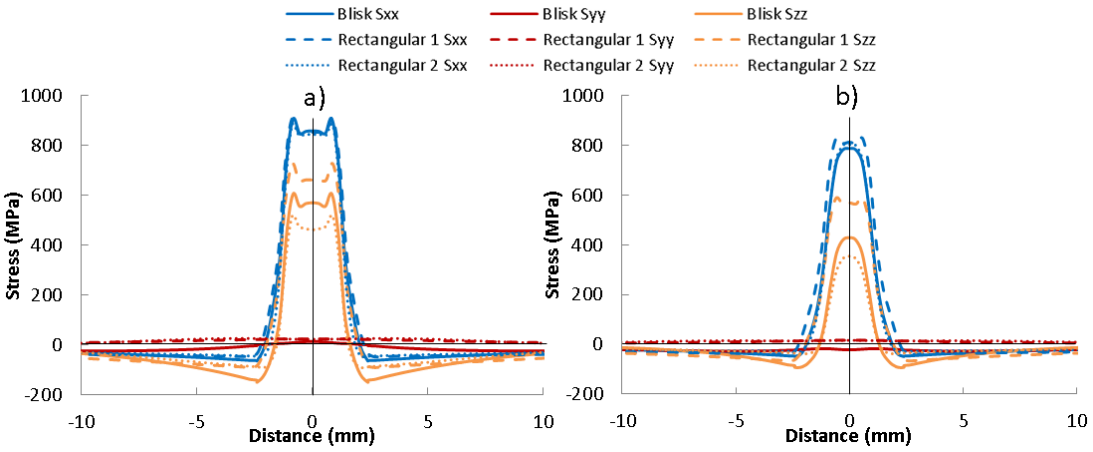

Figure 6-9: Comparison of residual stresses predicted within the blisk like geometry model and rectangular models 1 and 2 in the *x* direction, using the welding conditions of a) weld 1 and b) weld 3

6.3.4 Post-weld heat treatment

Numerical predictions of as-welded and post-weld heat treated samples with the cycle 1 heat treatment (see Table 6-3) produced the residual stress profiles shown in Figure 6-10 for welds 1 and 3. The combined effect of lowering the yield stress, allowing the material to yield due to the internal residual stresses and creep mechanism, reduced the peak magnitude of residual stresses to about 100 MPa for weld 1 and 70 MPa for weld 3. Therefore, the post-weld heat treatment shows a significant relief in the residual stress magnitudes but did not affect the widths of their distribution which is dictated by the width of the original residual stress profile. These results are comparable with the measurements done by Frankel et al.[45] using synchrotron X-ray diffraction on LFW post-weld heat treated samples with a holding temperature of about 650 ºC; however the holding time was not provided by the authors.

Residual stresses predicted in the x direction for welds 1 and 3, after simulating the different PWHT cycles presented in Table 6-3 are shown in Figure 6-11. Little variation is recorded in the stress profile when increasing the holding temperature by 100 ºC. Furthermore, after 3h most of the stress relief had already occurred and the numerical predictions show that no benefit arises from holding the same temperature for 6h. Finally, owing to the small differences in

the residual stress profiles obtained with the different PWHT cycles, cycle 1 seems to be adequate to relieve the majority of the residual stresses.

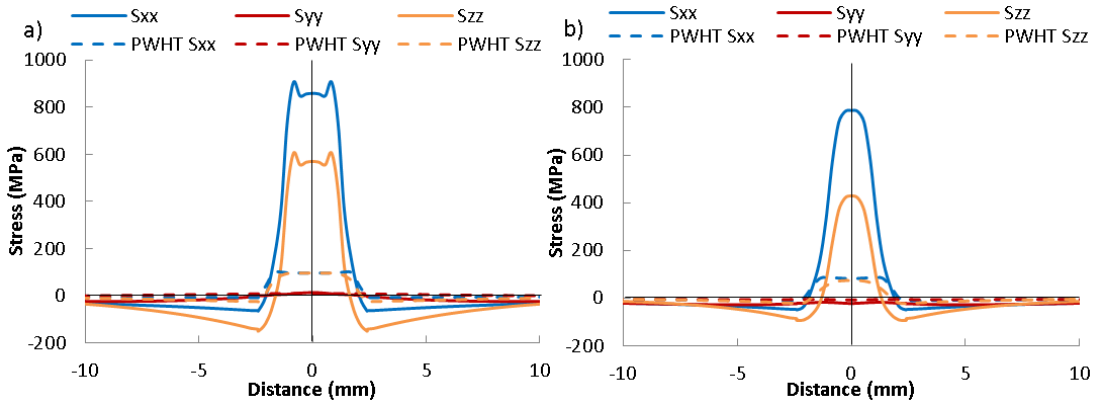

Figure 6-10: Comparison of the residual stress profiles obtained as welded and after PWHT cycle 1 for a) weld 1 and b) weld 3

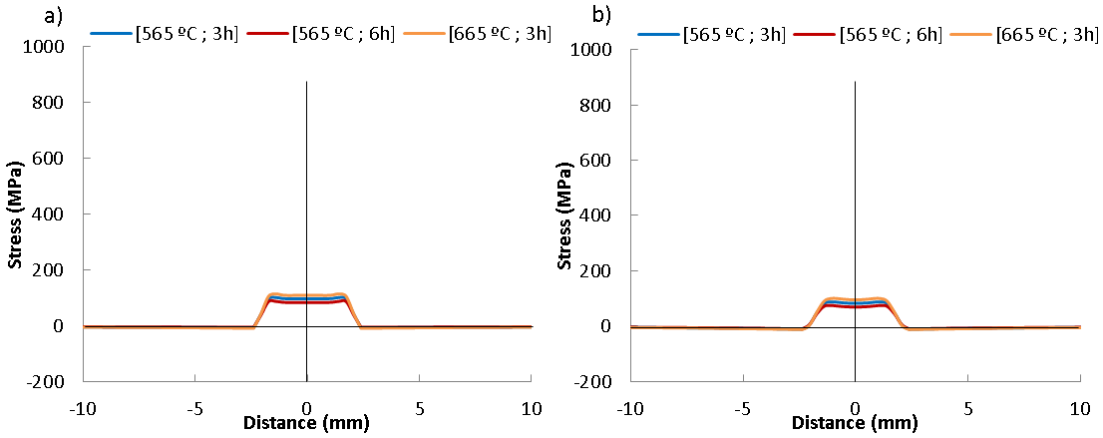

Figure 6-11: Residual stress in the *x* direction for different PWHT cycles with the holding temperature and holding time displayed for each curves for a) weld 1 and b) weld 3

6.4 Conclusions

The key findings from this work are:

1. The method for predicting residual stresses in this thesis can successfully predict residual stresses in a complex geometry such as a blisk. A reasonable agreement was found between residual stresses numerically predicted for the two welding conditions and those measured using contour method. Experiments and numerical predictions showed

only small differences in the results between both welding conditions.

2. The flash was found to extend the large magnitude residual stresses to the edges of the weld interface in the contour measurements.

3. The residual stress distribution created on a rectangular coupon showed many similarities with the blisk like geometry weld. Notably, residual stresses extracted in the longest direction of the weld interface, which typically have the highest magnitudes, were almost identical. This result demonstrates that the peculiar shape of the blisk like geometry weld does not affect significantly the residual stress field, as the peak magnitude is driven by the overall length of the part and the thermal profile prior to cooling.

4. A significant stress relief was achieved after a PWHT cycle. Among the cycles investigated, a holding temperature of 565 ºC and a holding time of 3h were found to be adequate to remove most of the residual stresses.

Chapter 7: Thesis conclusions

Numerical prediction of residual stresses within LFW

The main objective of this project was to develop a computationally efficient modelling approach capable of predicting the residual stress field created after welding and provide a deep understanding of its development. The computational constraints inherent to the modelling approaches available in the literature have been explained. Authors from the literature tend to model the mechanical mixing occurring at the interface of a linear friction weld which is complex, making it difficult to study the development of residual stresses within real engineering workpieces. To address this, a sequentially-coupled numerical model of a Ti-6Al-4V LFW was developed, bypassing the modelling of the oscillations by applying a heat flux at the weld interface and sequentially removing rows of elements to account for the burn-off. Prior to the computation of the model, the machine data obtained during welding was post-processed and the average heat flux per phase was calculated and used as an input to the model.

The thermal and mechanical predictions for several sets of welding condition were validated. Thermal histories numerically predicted on rectangular welds, exhibited a reasonable match against the thermocouple recordings with errors in thermal gradients obtained after 0.3 mm of burn-off, between experiments and simulations, ranging from 4% with weld 5 to 29% with weld 3. A comparison of residual stresses numerically predicted and measured using contour method and neutron diffraction on rectangular welds displayed a good agreement for the welding condition with the lowest rubbing velocity. Contour method measurements for other welding conditions were also conducted and exhibited more differences against the numerical results. Similar discrepancies were recorded between the contour method and synchrotron X-ray diffraction measurements conducted by Frankel et al.[45]. These discrepancies are believed to have been enhanced by cutting-induced plasticity and increased surface roughness owing to the EDM cut because of the significantly higher stress

gradients developed by these welding conditions. This may indicate that further research should be conducted on implementing the contour method technique specifically for LFW to improve its accuracy.

Experimental measurements found in the literature on rectangular welds were found to be in good agreement, both in terms of magnitude and distribution, with the residual stress numerically predicted in this thesis. The modelling approach was also successfully implemented on a real engineering workpiece. In chapter 6, a blisk LFW was modelled with numerical predictions showing reasonable agreement with the contour method measurements. The outcomes from chapter 6 are significant because to the best knowledge of the author, it is the first time that an accurate residual stress prediction was made on a blisk geometry LFW. This demonstrates how the modelling approach developed in this thesis can be applied to real engineering components.

Effects of process parameters on residual stress development

A limited number of publications on the effect of process parameters on the residual stress field developed within LFW can be found and often focus on the effect of the applied pressure[13,14,50,93]. Various effects of the process parameters on the residual stress development in rectangular welds have been studied in this thesis and one of them is the rubbing velocity in chapter 4. Increasing the rubbing velocity resulted in an increase of the peak of residual stress for the model and a narrower band of tensile residual stress. Furthermore, this study highlighted a strong correlation between the phase 3 temperature profile developed during welding and the residual stress field subsequently created, which is consistent with the conclusion made by Turner et al.[13]. For this reason, coefficients which relate directly to the thermal gradient and peak temperature values of the phase 3 temperature profile were used as inputs in the ANOVA conducted in chapter 5. The ANOVA demonstrated that the temperature gradient has a dominant effect on the residual stress magnitude and distribution in the direction of the weld interface which is consistent with the results from a numerical model developed by Fu et al.[14]. A practical outcome of the results found in chapter 5 is that to minimise the

magnitude of the residual stresses, a low phase 3 thermal gradient is necessary, which is created with a low burn-off rate welding condition (achievable with low values of frequency and amplitude[11]). However, this will result in a wide distribution of the residual stress and the effect on the microstructure and mechanical properties will need further investigation. Low weld interface temperature should be sought since it was found to reduce both the magnitude and the size of the distribution of the tensile residual stresses and it can also be achieved with the low burn-off rate value as detailed in chapter 3.

Other parameters studied on rectangular welds include the weld interface length dimensions which were found to have an important effect on the residual stress magnitude but little effect on the width of the distribution. The combination of a low thermal gradient and small interface dimensions can result in a stress-free LFW which is of interest to end users of the process. Moreover, it was found that a large magnitude applied pressure was necessary to observe a reduction in the residual stress magnitude which is in agreement with the experimental results from Romero et al.[50] and the numerical results from Turner et al.[13]. The clamping pressure was found to have little effect on the residual stresses and should therefore be set to prevent the wobbling of the workpieces during welding.

Almost exclusively, authors in the literature focus their study on rectangular coupons because of its convenient shape, it is cheaper to manufacture and easier to model numerically. However, in chapter 6 the peculiar blisk like geometry was shown to have little effect on the final residual stress field as the peak magnitude is driven by the overall length of the part and the thermal profile prior to cooling. As a result, approximating the blisk geometry by a rectangular coupon offers good insight into the magnitude and distribution of residual stress profiles created.

No simulation of PWHT on LFW is available in the literature; however this is one of the techniques used to mitigate the residual stress with LFW. Several PWHT cycles were simulated to investigate the effect of the holding temperature and

time on the final residual stress field of a blisk weld. Among the different cycles investigated, a holding temperature of 565 ºC and a holding time of 3h were found optimal with a peak of residual stress magnitude reduced to 70 MPa after post-weld heat treatment. The stress relief achieved in this thesis is comparable with some of Frankel et al.'s measurements[45]; however the holding temperature is not explicitly given in this study. Further experiments would be necessary to validate the numerical predictions reached with the PWHT simulations.

Prospect for future research

This thesis addresses the gaps in knowledge presented in Chapter 2; however more work can be done to aid further development and optimisation of the linear friction welding process.

Recommended areas for further work are:

- Extend the modelling approach developed in this thesis to other materials, including dissimilar material welds.
- Include microstructural modelling capability to improve the accuracy of the numerical predictions.
- Conduct a similar ANOVA to the one presented in this thesis for the blisk-like geometry LFW.
- Conduct residual stress measurements on post-weld heat treated welds to confirm the numerical results.
- Improve the accuracy of contour method measurements on LFW.

References

1. Kumar, B. V. R. R. A Review on Blisk Technology. *Int. J. Innov. Res. Sci. Eng. Technol.* **2,** 1353–1358 (2013).
2. Wanjara, P. & Jahazi, M. Linear friction welding of Ti-6Al-4V: Processing, microstructure, and mechanical-property inter-relationships. *Metall. Mater. Trans. A* **36,** 2149–2164 (2005).
3. Li, W., Wu, H., Ma, T., Yang, C. & Chen, Z. Influence of Parent Metal Microstructure and Post-Weld Heat Treatment on Microstructure and Mechanical Properties of Linear Friction Welded Ti-6Al-4V Joint. *Adv. Eng. Mater.* **14,** 312–318 (2012).
4. Ofem, U. U., Colegrove, P. A., Addison, A. & Russell, M. J. Energy and force analysis of linear friction welds in medium carbon steel. *Sci. Technol. Weld. Join.* **15,** 479–485 (2010).
5. Li, W.-Y., Ma, T. & Li, J. Numerical simulation of linear friction welding of titanium alloy: Effects of processing parameters. *Mater. Des.* **31,** 1497–1507 (2010).
6. Schroeder, F., Ward, R. M., Turner, R. P., Walpole, A. R., Attallah, M. M., Gebelin, J.-C. & Reed, R. C. Validation of a Model of Linear Friction Welding of Ti6Al4V by Considering Welds of Different Sizes. *Metall. Mater. Trans. B* **46,** 2326–2331 (2015).
7. McAndrew, A. R., Colegrove, P. A., Addison, A. C., Flipo, B. C. D., Russell, M. J. & Lee, L. A. Modelling of the workpiece geometry effects on Ti–6Al–4V linear friction welds. *Mater. Des.* **87,** 1087–1099 (2015).
8. McAndrew, A. R., Colegrove, P. A., Addison, A. C., Flipo, B. C. D. & Russell, M. J. Modelling the influence of the process inputs on the removal of surface contaminants from Ti–6Al–4V linear friction welds. *Mater. Des.* **66,** 183–195 (2015).
9. Schroeder, F., Ward, R. M., Turner, R. P., Attallah, M. M., Gebelin, J. & Reed, R. C. Linear Friction Welding of Titanium Alloys for Aeroengine Applications : Modelling and Validation. in *9th Int. Conf. Trends Weld. Res.* 886–892 (2012).
10. Turner, R., Gebelin, J.-C., Ward, R. M. & Reed, R. C. Linear friction welding of Ti–6Al–4V: Modelling and validation. *Acta Mater.* **59,** 3792–3803 (2011).
11. McAndrew, A. R., Colegrove, P. A., Addison, A. C., Flipo, B. C. D. & Russell, M. J. Energy and Force Analysis of Ti-6Al-4V Linear Friction Welds for Computational Modeling Input and Validation Data. *Metall. Mater. Trans. A* **45,** 6118–6128 (2014).
12. Zhao, P., Fu, L. & Zhong, D. Numerical simulation of transient temperature and axial deformation during linear friction welding between TC11 and TC17 titanium alloys. *Comput. Mater. Sci.* **92,** 325–333 (2014).
13. Turner, R., Ward, R. M., March, R. & Reed, R. C. The Magnitude and

Origin of Residual Stress in Ti-6Al-4V Linear Friction Welds: An Investigation by Validated Numerical Modeling. *Metall. Mater. Trans. B* **43,** 186–197 (2012).

14. Fu, Y., Li, W.-Y., Yang, X.-W., Ma, T.-J. & Vairis, A. The effects of forging pressure and temperature field on residual stresses in linear friction welded Ti6Al4V joints. *Adv. Manuf.* **4,** 314–321 (2016).
15. Vairis, A. & Frost, M. High frequency linear friction welding of a titanium alloy. *Wear* **217,** 117–131 (1998).
16. Song, X., Xie, M., Hofmann, F., Jun, T. S., Connolley, T., Reinhard, C., Atwood, R. C., Connor, L., Drakopoulos, M., Harding, S. & Korsunsky, A. M. Residual stresses in Linear Friction Welding of aluminium alloys. *Mater. Des.* **50,** 360–369 (2013).
17. Liu, X., Lan, S. & Ni, J. Analysis of process parameters effects on friction stir welding of dissimilar aluminum alloy to advanced high strength steel. *Mater. Des.* **59,** 50–62 (2014).
18. DeWald, A. T., Legzdina, D., Clausen, B., Brown, D. W., Sisneros, T. A. & Hill, M. R. in (eds. Ventura, C. E., Crone, W. C. & Furlong, C.) **4,** 183–189 (Springer New York, 2013).
19. Maalekian, M. Friction welding – critical assessment of literature. *Sci. Technol. Weld. Join.* **12,** 738–759 (2007).
20. Guo, Y., Jung, T., Chiu, Y. L., Li, H., Bray, S. & Bowen, P. Microstructure and microhardness of Ti6246 linear friction weld. *Mater. Sci. Eng. A* **562,** 17–24 (2013).
21. Bhamji, I., Preuss, M., Threadgill, P. L. & Addison, A. C. Solid state joining of metals by linear friction welding: a literature review. *Mater. Sci. Technol.* **27,** 2–12 (2011).
22. Mishra, R. S. & Ma, Z. Y. Friction stir welding and processing. *Mater. Sci. Eng. R Reports* **50,** 1–78 (2005).
23. Mitlin, D., Radmilovic, V., Pan, T., Chen, J., Feng, Z. & Santella, M. L. Structure–properties relations in spot friction welded (also known as friction stir spot welded) 6111 aluminum. *Mater. Sci. Eng. A* **441,** 79–96 (2006).
24. D'Urso, G. Thermo-mechanical characterization of friction stir spot welded AA6060 sheets: Experimental and FEM analysis. *J. Manuf. Process.* **17,** 108–119 (2015).
25. Cox, C. D., Gibson, B. T., Strauss, A. M. & Cook, G. E. Energy input during friction stir spot welding. *J. Manuf. Process.* **16,** 479–484 (2014).
26. Chamanfar, A., Jahazi, M. & Cormier, J. A Review on Inertia and Linear Friction Welding of Ni-Based Superalloys. *Metall. Mater. Trans. A* **46,** 1639–1669 (2015).
27. Maalekian, M., Kozeschnik, E., Brantner, H. P. & Cerjak, H. Comparative analysis of heat generation in friction welding of steel bars. *Acta Mater.* **56,** 2843–2855 (2008).

28. Alves, E. P., Piorino Neto, F. & An, C. Y. Welding of AA1050 Aluminum with AISI 304 stainless steel by rotary friction welding process. *J. Aerosp. Technol. Manag.* **2,** 301–306 (2010).

29. Richter, W. Herbeifuehrung einer haftverbindung zwischen plaettchen aus werkzeugstahl und deren traegern nach art einer schweissung oder loetung. (1929).

30. Coules, H. E. Characterising the effects of high-pressure rolling on residual stress in structural steel welds. (2012).

31. Effertz, P., Fuchs, F. & Enzinger, N. 3D Modelling of Flash Formation in Linear Friction Welded 30CrNiMo8 Steel Chain. *Metals (Basel).* **7,** 449 (2017).

32. Li, W., Shi, S., Wang, F., Zhang, Z. & Li, J. Numerical Simulation of Friction Welding Processes Based on Abaqus Environment. *Eng. Sci. Technol. Rev.* **5,** 10–19 (2012).

33. Vairis, A. & Frost, M. Modelling the linear friction welding of titanium blocks. *Mater. Sci. Eng. A* **292,** 8–17 (2000).

34. Li, W. Y., Shi, S. X., Wang, F. F., Ma, T. J., Li, J. L., Gao, D. L. & Vairis, A. Heat reflux in flash and its effect on joint temperature history during linear friction welding of steel. *Int. J. Therm. Sci.* **67,** 192–199 (2013).

35. Midling, O. T. & Grong, O. A process model for friction welding of A1-Mg-Si alloys and Al-SiC metal matrix composite--I . HAZ temperature and strain rate distribution. *Acta Met. mater.* **42,** 1595–1609 (1994).

36. Sorina-Müller, J., Rettenmayr, M., Schneefeld, D., Roder, O. & Fried, W. FEM simulation of the linear friction welding of titanium alloys. *Comput. Mater. Sci.* **48,** 749–758 (2010).

37. Grujicic, M., Arakere, G., Pandurangan, B., Yen, C.-F. & Cheeseman, B. a. Process Modeling of Ti-6Al-4V Linear Friction Welding (LFW). *J. Mater. Eng. Perform.* **21,** 2011–2023 (2012).

38. Maio, L., Liberini, M., Campanella, D., Astarita, A., Esposito, S., Boccardi, S. & Meola, C. Infrared thermography for monitoring heat generation in a linear friction welding process of Ti6Al4V alloy. *Infrared Phys. Technol.* **81,** 325–338 (2017).

39. Moody, S. M. & Atkinson, J. R. Linear Friction Welding of Polypropylene and Polycarbonate .1. Effects of Welding Conditions on Strength of Welds. *Plast. Rubber Compos. Process. Appl.* **17,** 203–209 (1992).

40. Moody, S. M. & Atkinson, J. R. Linear Friction Welding of Polypropylene and Polycarbonate .2. The Microstructures and Mechanical-Properties of Pp Welds Made Using Optimum Conditions. *Plast. Rubber Compos. Process. Appl.* **17,** 211–217 (1992).

41. Ruponen, J., Čermák, P., Rhême, M., Miettinen, A., Rohumaa, A. & Rautkari, L. Influence of Welding Time on Tensile-Shear Strength of Linear Friction Welded Birch (Betula pendula L.) Wood. *BioResources* **10,** 3481–3491 (2015).

42. Omrani, P., Mansouri, H. R., Duchanois, G. & Pizzi, A. Fracture Mechanics of Linearly Welded Wood Joints: Effect of Wood Species and Grain Orientation. *J. Adhes. Sci. Technol.* **23,** 2057–2072 (2009).

43. Vaziri, M., Lindgren, O. & Pizzi, A. Influence of Machine Setting and Wood Parameters on Crack Formation in Scots Pine Joints Produced by Linear Friction Welding Influence of Machine Setting and Wood Parameters on Crack Formation in Scots Pine Joints Produced by. **4243,** (2017).

44. Addison, A. C. *Linear friction welding information for production engineering. TWI industrial members report - 961/2010*. (2010).

45. Frankel, P., Preuss, M., Steuwer, A., Withers, P. J. & Bray, S. Comparison of residual stresses in Ti–6Al–4V and Ti–6Al–2Sn–4Zr–2Mo linear friction welds. *Mater. Sci. Technol.* **25,** 640–650 (2009).

46. Li, W., Suo, J., Ma, T., Feng, Y. & Kim, K. Abnormal microstructure in the weld zone of linear friction welded Ti–6.5Al–3.5Mo–1.5Zr–0.3Si titanium alloy joint and its influence on joint properties. *Mater. Sci. Eng. A* **599,** 38–45 (2014).

47. Chen, X., Xie, F. Q., Ma, T. J., Li, W. Y. & Wu, X. Q. Effects of post-weld heat treatment on microstructure and mechanical properties of linear friction welded Ti2AlNb alloy. *Mater. Des.* **94,** 45–53 (2016).

48. Karadge, M., Preuss, M., Lovell, C., Withers, P. J. & Bray, S. Texture development in Ti–6Al–4V linear friction welds. *Mater. Sci. Eng. A* **459,** 182–191 (2007).

49. McAndrew, A. R., Colegrove, P. A., Flipo, B. C. D. & Bühr, C. 3D modelling of Ti–6Al–4V linear friction welds. *Sci. Technol. Weld. Join.* **1718,** 1–9 (2016).

50. Romero, J., Attallah, M. M., Preuss, M., Karadge, M. & Bray, S. E. Effect of the forging pressure on the microstructure and residual stress development in Ti–6Al–4V linear friction welds. *Acta Mater.* **57,** 5582–5592 (2009).

51. Daymond, M. R. & Bonner, N. W. Measurement of strain in a titanium linear friction weld by neutron diffraction. *Phys. B Condens. Matter* **325,** 130–137 (2003).

52. Turner, R., Schroeder, F., Ward, R. M. & Brooks, J. W. The Importance of Materials Data and Modelling Parameters in an FE Simulation of Linear Friction Welding. *Adv. Mater. Sci. Eng.* **2014,** 1–8 (2014).

53. García, A. M. M. BLISK Fabrication by Linear Friction Welding. *Adv. Gas Turbine Technol.* 411–434 (2011).

54. Jun, T.-S., Rotundo, F., Song, X., Ceschini, L. & Korsunsky, A. M. Residual strains in AA2024/AlSiCp composite linear friction welds. *Mater. Des.* **31,** S117–S120 (2010).

55. Jun, T. & Korsunsky, A. M. Eigenstrain reconstruction method in linear friction welded aluminium alloy and MMC plates. *Int. J. Numer. Methods*

Eng. **84,** 989–1008 (2010).

56. Fratini, L., Buffa, G., Cammalleri, M. & Campanella, D. On the linear friction welding process of aluminum alloys: Experimental insights through process monitoring. *CIRP Ann. - Manuf. Technol.* **62,** 295–298 (2013).

57. Buffa, G., Cammalleri, M., Campanella, D., La Commare, U. & Fratini, L. Linear friction welding of dissimilar AA6082 and AA2011 aluminum alloys: microstructural characterization and design guidelines. *Int. J. Mater. Form.* **10,** 307–315 (2017).

58. Li, W., Wang, F., Shi, S., Ma, T., Li, J. & Vairis, A. 3D Finite Element Analysis of the Effect of Process Parameters on Linear Friction Welding of Mild Steel. *J. Mater. Eng. Perform.* **23,** 4010–4018 (2014).

59. Bhamji, I., Moat, R. J., Preuss, M., Threadgill, P. L., Addison, A. C. & Peel, M. J. Linear friction welding of aluminium to copper. *Sci. Technol. Weld. Join.* **17,** 314–320 (2012).

60. Bhamji, I., Preuss, M., Moat, R. J., Threadgill, P. L. & Addison, A. C. Linear friction welding of aluminium to magnesium. *Sci. Technol. Weld. Join.* **17,** 368–374 (2012).

61. Bhandari, V. Linear friction welding of titanium to stainless steel. M.Sc. Thesis. (2010).

62. Peters, M., Hemptenmacher, J., Kumpfert, J. & Leyens, C. in *Titan. Titan. Alloy. Fundam. Appl.* 1–36 (2003).

63. Lütjering, G. Influence of processing on microstructure and mechanical properties of (α+β) titanium alloys. *Mater. Sci. Eng. A* **243,** 32–45 (1998).

64. Liu, C. & Dong, C. Internal residual stress measurement on linear friction welding of titanium alloy plates with contour method. *Trans. Nonferrous Met. Soc. China* **24,** 1387–1392 (2014).

65. Li, W.-Y., Ma, T., Zhang, Y., Xu, Q., Li, J., Yang, S. & Liao, H. Microstructure Characterization and Mechanical Properties of Linear Friction Welded Ti-6Al-4V Alloy. *Adv. Eng. Mater.* **10,** 89–92 (2008).

66. Withers, P. J. Residual stress and its role in failure. *Reports Prog. Phys.* **70,** 2211–2264 (2007).

67. Ueda, Y., Murakawa, H. & Ma, N. in *Weld. Deform. Residual Stress Prev.* 35–53 (Elsevier, 2012).

68. Ashby, M. F. Physical modelling of materials problems. *Mater. Sci. Technol.* **8,** 102–111 (1992).

69. Van Boven, G., Chen, W. & Rogge, R. The role of residual stress in neutral pH stress corrosion cracking of pipeline steels. Part I: Pitting and cracking occurrence. *Acta Mater.* **55,** 29–42 (2007).

70. L.D. Cozzolino. Finite element analysis of localised rolling to reduce residual stress and distortion. (2013).

71. Masubuchi. Analysis and Control of Distortion in Welded Aluminum Structures. *Weld. Res.* 251–262 (1978).

72. Vanderaa, E. M. Local Cooling during Welding : Prediction and Control of Residual Stresses and Buckling Distortion. (2007).

73. Xie, P., Zhao, H. & Liu, Y. Measuring residual stresses in linear friction welded joints composed by dissimilar titanium. *Sci. Technol. Weld. Join.* **21,** 351–357 (2016).

74. Smith, M., Bichler, L. & Sediako, D. Measurement of Residual Stresses in Linear Friction Welded In-Service Inconel 718 Superalloy. *Mater. Sci. Forum* **879,** 1800–1806 (2016).

75. Prime, M. B. Cross-Sectional Mapping of Residual Stresses by Measuring the Surface Contour After a Cut. *J. Eng. Mater. Technol.* **123,** 162 (2001).

76. Sun, Y. L., Roy, M. J., Vasileiou, A. N., Smith, M. C., Francis, J. A. & Hosseinzadeh, F. Evaluation of Errors Associated with Cutting-Induced Plasticity in Residual Stress Measurements Using the Contour Method. *Exp. Mech.* **57,** 719–734 (2017).

77. Traoré, Y., Hosseinzadeh, F. & Bouchard, P. J. Plasticity in the Contour Method of Residual Stress Measurement. *Adv. Mater. Res.* **996,** 337–342 (2014).

78. Schajer, Gary, S. in *Pract. Residual Stress Meas. Methods* (2013).

79. Prime, M. B., Dewald, A. T. & Schajer, G. S. in *Pract. Residual Stress Meas. Methods* 109–138 (2013).

80. Bragg, L. X-ray crystallography. *Sci. Am.* **219,** 58–70 (1968).

81. Johnson, G. Residual stress measurements using the contour method. (2008).

82. Withers, P. J. Depth capabilities of neutron and synchrotron diffraction strain measurement instruments. I. The maximum feasible path length. *J. Appl. Crystallogr.* **37,** 596–606 (2004).

83. Ma, T. J., Li, X., Zhong, B. & Li, W. Y. Effects of annealing on microstructure and properties of linear friction welded dissimilar titanium joints. *Sci. Technol. Weld. Join.* **19,** 689–695 (2014).

84. Smith, M., Bichler, L., Gholipour, J. & Wanjara, P. Mechanical properties and microstructural evolution of in-service Inconel 718 superalloy repaired by linear friction welding. *Int. J. Adv. Manuf. Technol.* **90,** (2017).

85. Wanjara, P., Dalgaard, E., Gholipour, J., Cao, X., Cuddy, J. & Jonas, J. J. Effect of Pre- and Post-weld Heat Treatments on Linear Friction Welded Ti-5553. *Metall. Mater. Trans. A* **45,** 5138–5157 (2014).

86. Li, W., Vairis, A., Preuss, M. & Ma, T. Linear and rotary friction welding review. *Int. Mater. Rev.* **61,** 71–100 (2016).

87. Dong, P., Song, S. & Zhang, J. Analysis of residual stress relief mechanisms in post-weld heat treatment. *Int. J. Press. Vessel. Pip.* **122,** 6–14 (2014).

88. Boyer, Rodney Welsch, Gerhard Collings, E. *Materials Properties Handbook: Titanium Alloys*. (ASM International, 1994).

89. Carslaw, H. S. & Jaeger, J. C. *The Conduction of Heat in Solids*. (Oxford University Press, 1959).

90. Li, W.-Y., Ma, T. & Yang, S. Microstructure Evolution and Mechanical Properties of Linear Friction Welded Ti-5Al-2Sn-2Zr-4Mo-4Cr (Ti17) Titanium Alloy Joints. *Adv. Eng. Mater.* **12,** 35–43 (2010).

91. Doghri, I. *Mechanic of Deformable Solids: Linear, Non-linear, analytical and Computational Aspects*. (Springer, 2000).

92. Bhavikatti, S. S. *Finite Element Analysis*. (New Age International, 2005).

93. Nikiforov, R., Medvedev, A., Tarasenko, E. & Vairis, A. Numerical Simulation of Residual Stresses in Linear Friction Welded Joints. *J. Eng. Sci. Technol. Rev.* **8,** 157–173 (2015).

94. Yamileva, A. M., Gazizov, R. K. & Vairis, A. Computer modelling of the effect of clamping in linear friction welding. *J. Eng. Mater. Technol.* **8,** 65–68 (2015).

95. Ceretti, E., Fratini, L., Giardini, C. & La Spisa, D. Numerical modelling of the linear friction welding process. *Int. J. Mater. Form.* **3,** 1015–1018 (2010).

96. Fratini, L., Buffa, G., Campanella, D. & La Spisa, D. Investigations on the linear friction welding process through numerical simulations and experiments. *Mater. Des.* **40,** 285–291 (2012).

97. Calamaz, M., Coupard, D. & Girot, F. A new material model for 2D numerical simulation of serrated chip formation when machining titanium alloy Ti–6Al–4V. *Int. J. Mach. Tools Manuf.* **48,** 275–288 (2008).

98. Gardner, J. D. *Comparative Study of Finite Element Simulation Software*. *Consort. Deburring Edge Finish.* (2005).

99. He, X., Gu, F. & Ball, A. A review of numerical analysis of friction stir welding. *Prog. Mater. Sci.* **65,** 1–66 (2014).

100. Dubourg, L., Doran, P., Gharghouri, M. A., Larose, S. & Jahazi, M. Prediction and Measurements of Thermal Residual Stresses in AA2024-T3 Friction Stir Welds as a Function of Welding Parameters. *Mater. Sci. Forum* **638–642,** 1215–1220 (2010).

101. Khandkar, M. Z. H., Khan, J. a., Reynolds, A. P. & Sutton, M. A. Predicting residual thermal stresses in friction stir welded metals. *J. Mater. Process. Technol.* **174,** 195–203 (2006).

102. El-Hadek, M. a. Numerical Simulation of the Inertia Friction Welding Process of Dissimilar Materials. *Metall. Mater. Trans. B* **45,** 2346–2356 (2014).

103. Grant, B., Preuss, M., Withers, P. J., Baxter, G. & Rowlson, M. Finite element process modelling of inertia friction welding advanced nickel-based superalloy. *Mater. Sci. Eng. A* **513–514,** 366–375 (2009).

104. Balasubramanian, V., Li, Y., Stotler, T., Crompton, J., Katsube, N. & Soboyejo, W. An Energy Balance Method for the Numerical Simulation of Inertia Welding. *Mater. Manuf. Process.* **14,** 755–773 (1999).

105. Blau, P. J. The significance and use of the friction coefficient. *Tribol. Int.* **34,** 585–591 (2001).

106. McAndrew, A. R., Colegrove, P. A., Bühr, C., Flipo, B. C. D. & Vairis, A. A literature review of Ti-6Al-4V linear friction welding. *Prog. Mater. Sci.* **92,** 225–257 (2018).

107. Majorell, A., Srivatsa, S. & Picu, R. C. Mechanical behavior of Ti – 6Al – 4V at high and moderate temperatures — Part I : Experimental results. *Mater. Sci. Eng. A* **326,** 306–316 (2002).

108. Kiselyeva, S, K., Yamileva, A, M. & Karavaeva, M, V. Computer Modelling of Linear Friction Welding Based on the Joint Microstructure. *J. Eng. Sci. Technol. Rev.* **5,** 44–47 (2012).

109. Grong, O. *Metallurgical Modelling of Welding*. *Metall. Model. Weld.* (Institute of Materials, 1997).

110. Boivineau, M., Cagran, C., Doytier, D., Eyraud, V., Nadal, M.-H., Wilthan, B. & Pottlacher, G. Thermophysical Properties of Solid and Liquid Ti-6Al-4V (TA6V) Alloy. *Int. J. Thermophys.* **27,** 507–529 (2006).

111. Mills, K. C. *Recommended values of thermophysical properties for selected commercial alloys*. (Woodhead publishing, 2002).

112. Shean Lee, R. & Chang Lin, H. Process design based on the deformation mechanism for the non-isothermal forging of Ti–6Al–4V alloy. *J. Mater. Process. Technol.* **79,** 224–235 (1998).

113. Basak, D., Overfelt, R. a & Wang, D. Measurement of Specific Heat Capacity and Electrical Resistivity of Industrial Alloys Using Pulse Heating Techniques. *Int. J. Thermophys.* **24,** 1721–1733 (2003).

114. Seshacharyulu, T., Medeiros, S. C., Frazier, W. G. & Prasad, Y. V. R. K. Hot working of commercial Ti–6Al–4V with an equiaxed α–β microstructure: materials modeling considerations. *Mater. Sci. Eng. A* **284,** 184–194 (2000).

115. Chen, G., Ren, C., Qin, X. & Li, J. Temperature dependent work hardening in Ti–6Al–4V alloy over large temperature and strain rate ranges: Experiments and constitutive modeling. *Mater. Des.* **83,** 598–610 (2015).

116. Guo, Z., Saunders, N. & Miodownik, a P. Modelling high temperature flow stress curves of Titanium alloys. in *MRS Int. Mater. Res. Conf.* (2008).

117. Schröder, F., Ward, R. M., Walpole, A. R., Turner, R. P., Attallah, M. M., Gebelin, J.-C. & Reed, R. C. Linear friction welding of Ti6Al4V: experiments and modelling. *Mater. Sci. Technol.* **31,** 372–384 (2015).

118. Muránsky, O., Hamelin, C. J., Hosseinzadeh, F. & Prime, M. B. Evaluation of a self-equilibrium cutting strategy for the contour method of residual stress measurement. *Int. J. Press. Vessel. Pip.* 1–10 (2016). doi:http://dx.doi.org/10.1016/j.ijpvp.2017.04.002

119. Pratihar, S., Turski, M., Edwards, L. & Bouchard, P. J. Neutron diffraction residual stress measurements in a 316L stainless steel bead-on-plate

weld specimen. *Int. J. Press. Vessel. Pip.* **86,** 13–19 (2009).

120. Stapleton, A. M., Raghunathan, S. L., Bantounas, I., Stone, H. J., Lindley, T. C. & Dye, D. Evolution of lattice strain in Ti–6Al–4V during tensile loading at room temperature. *Acta Mater.* **56,** 6186–6196 (2008).
121. Seshacharyulu, T., Medeiros, S. C., Frazier, W. G. & Prasad, Y. V. R. K. Microstructural mechanisms during hot working of commercial grade Ti–6Al–4V with lamellar starting structure. *Mater. Sci. Eng. A* **325,** 112–125 (2002).
122. Richards, D. G., Prangnell, P. B., Williams, S. W. & Withers, P. J. Global mechanical tensioning for the management of residual stresses in welds. *Mater. Sci. Eng. A* **489,** 351–362 (2008).
123. Khuri, I. & Mukhopadhyay, S. Response surface methodology. *Wires Comput. Stat.* **2,** 128–149 (2010).
124. Bezerra, M., Santelli, R., Oliveira, E., Villar, L. & Escaleira, L. Response surface methodology (RSM) as a tool for optimization in analytical chemistry. **76,** 965–977 (2008).
125. Badea, L., Surand, M., Ruau, J. & Viguier, B. Creep behavior of Ti-6Al-4V from 450 ° C to 600 ° C. *U.P.B. Sci. Bull.* **76,** 185–196 (2014).
126. Simulia, A. 6. 1. Abaqus Analysis User's Guide/Inelastic Mechanical Properties/Metal plasticity/Creep behavior.

Appendix A : Ti-6Al-4V material properties used in the modelling work

Thermal and mechanical material properties used in the modelling work of this thesis are displayed in this appendix.

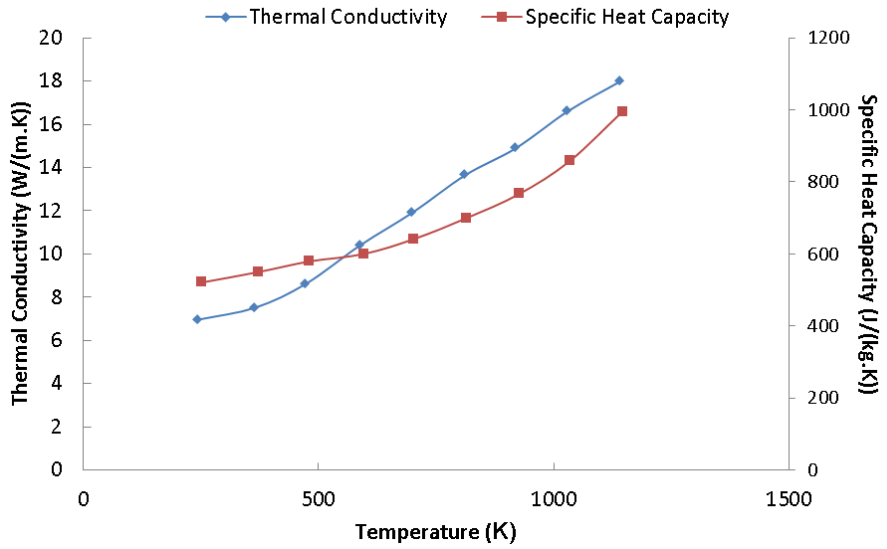

Thermal properties of Ti-6Al-4V used in the modelling work. These data are part of DEFORM software's standard library.

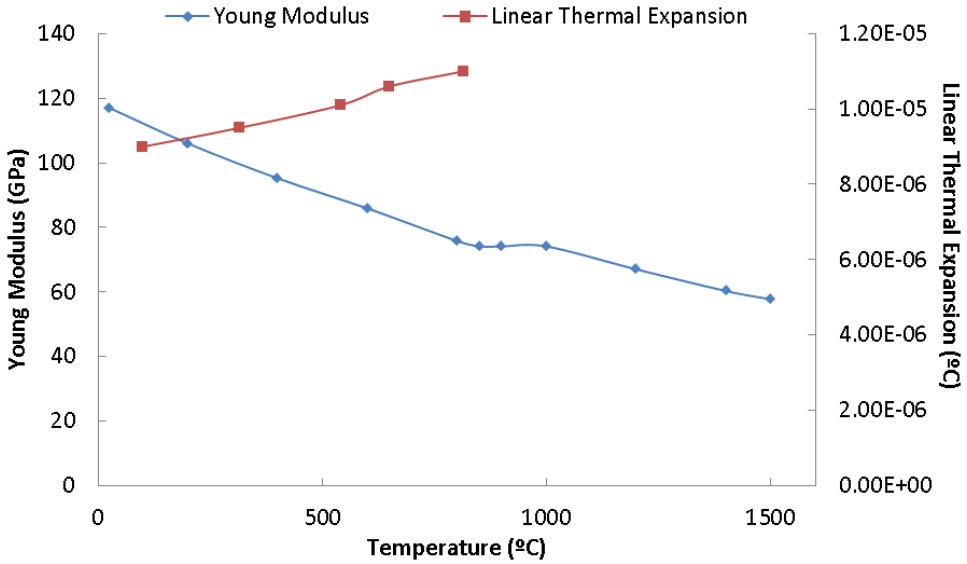

Young's modulus (source Turner et al.[13]) and linear thermal expansion coefficients (source Boyer et al.[88]) of Ti-6Al-4V used in the modelling work.

Appendix B: Equation from McAndrew et al. used in the thesis

Equation from McAndrew et al.[8] used to calculate the TMAZ thicknesses:

$$\textbf{TMAZ thickness} = 3.06495 + 1.17408 * A - 0.040652 * F_a - 0.29568 * A^2 + 2.20636 * 10^{-4} * {F_a}^2$$

where A is the amplitude and F_a is the applied force.

Equation from McAndrew et al.[8] used to calculate the experimental phase 3 burn-off rate:

$$\textbf{Burn} - \textbf{off rate} = 0.69581 - 0.042711 * f + 0.039751 * A - 6.79114 * 10^{-3} * F_a + 0.036051 * f * A + 4.66901 * 10^{-4} * f * F_a$$

where f is the frequency.

Appendix C: Neutron diffraction spectrums

Neutron diffraction spectrums in the directions *x* and *z* measured simultaneously in a LFW using the ENGIN-X diffractometer at the ISIS facility are presented below. Similarly, spectrums in the third direction of space and in the stress-free sample were also measured.

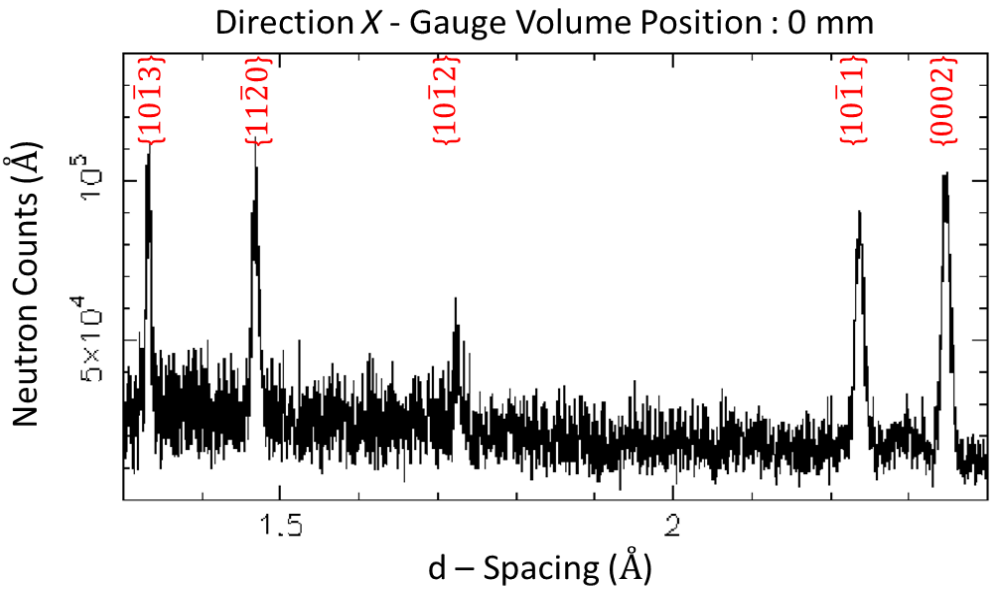

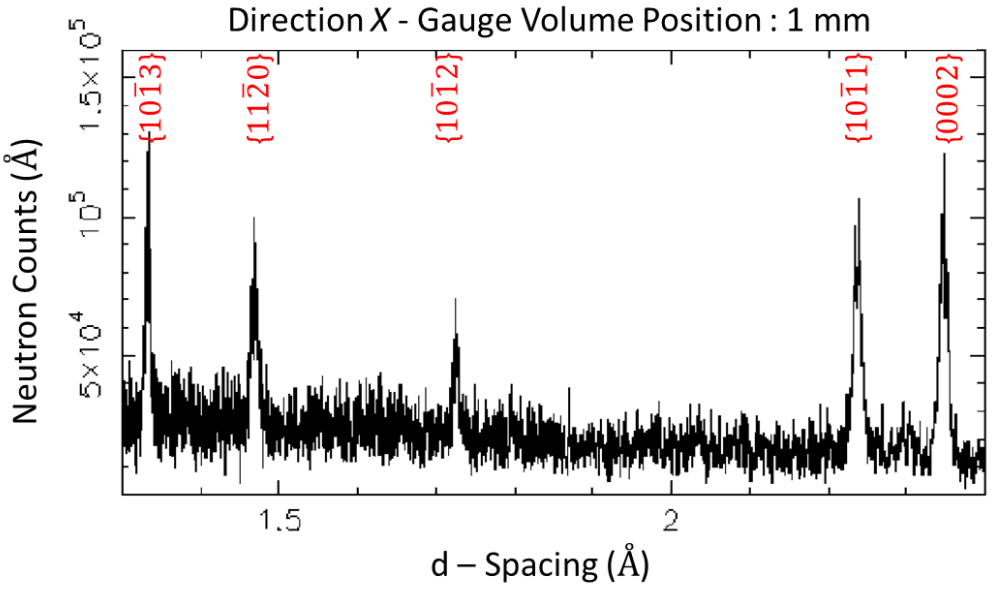

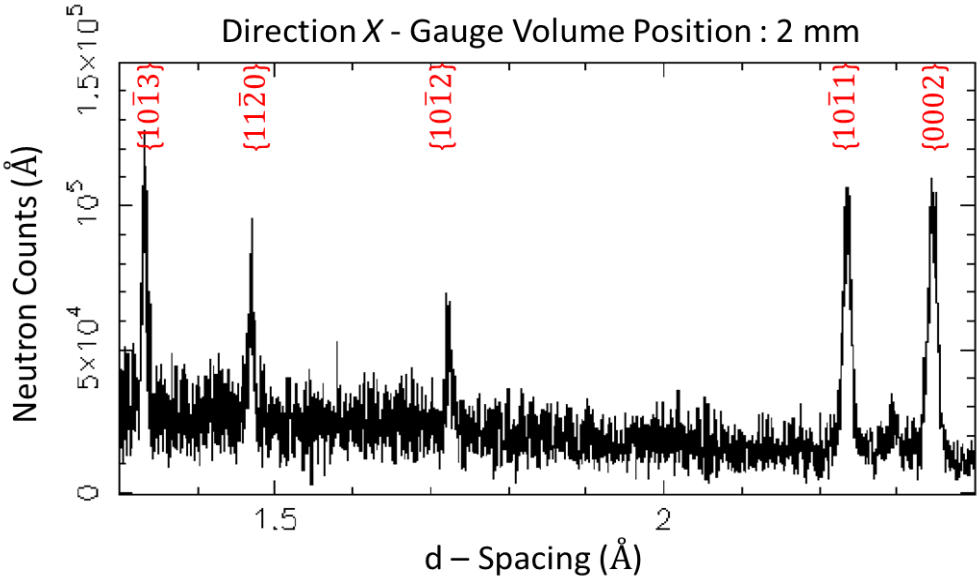
Direction X - Gauge Volume Position : 2 mm
Neutron Counts (Å)
0
5×10^4
10^5
1.5×10^5
{10$\bar{1}$3}
{11$\bar{2}$0}
{10$\bar{1}$2}
{10$\bar{1}$1}
{0002}
1.5
2
d – Spacing (Å)

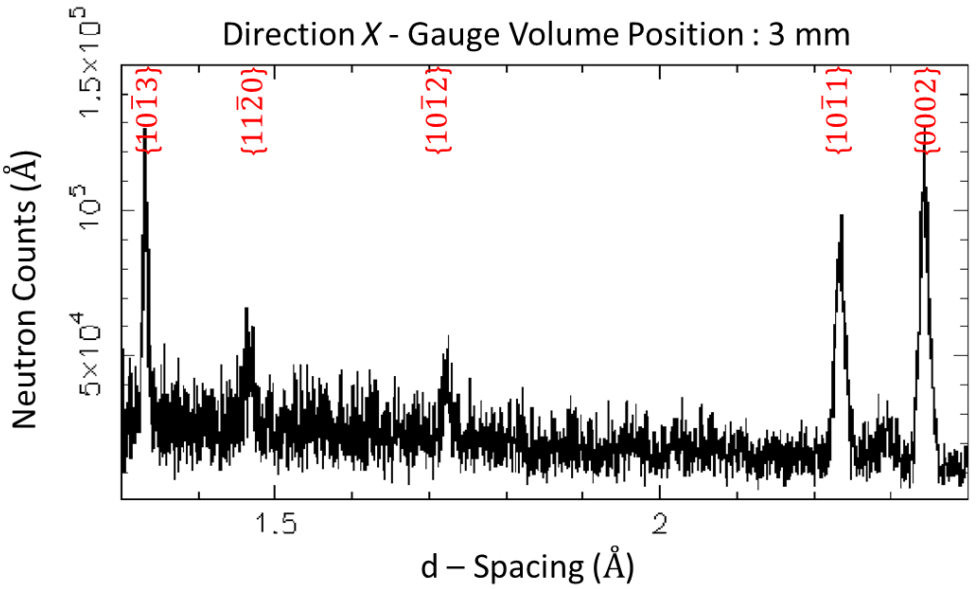
Direction X - Gauge Volume Position : 3 mm
Neutron Counts (Å)
5×10^4
10^5
1.5×10^5
{10$\bar{1}$3}
{11$\bar{2}$0}
{10$\bar{1}$2}
{10$\bar{1}$1}
{0002}
1.5
2
d – Spacing (Å)

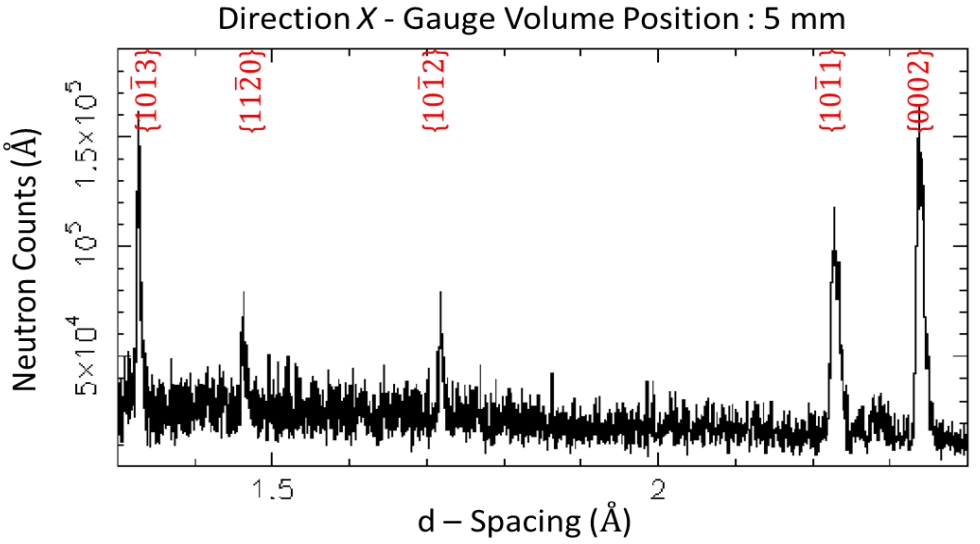
Direction X - Gauge Volume Position : 5 mm
Neutron Counts (Å)
5×10^4
10^5
1.5×10^5
{10$\bar{1}$3}
{11$\bar{2}$0}
{10$\bar{1}$2}
{10$\bar{1}$1}
{0002}
1.5
2
d – Spacing (Å)

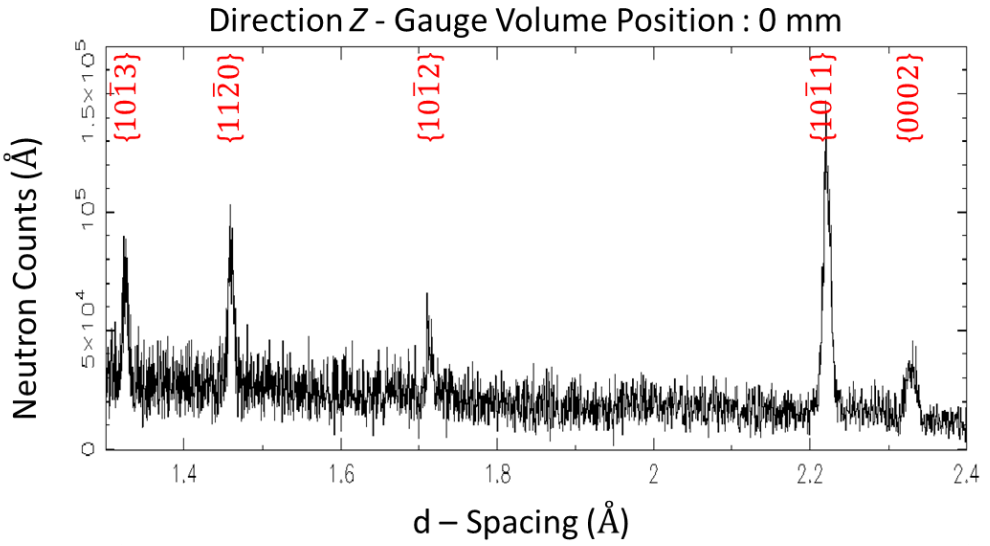
Direction Z - Gauge Volume Position : 0 mm
Neutron Counts (Å)
d – Spacing (Å)
{10$\bar{1}$3}
{11$\bar{2}$0}
{10$\bar{1}$2}
{10$\bar{1}$1}
{0002}

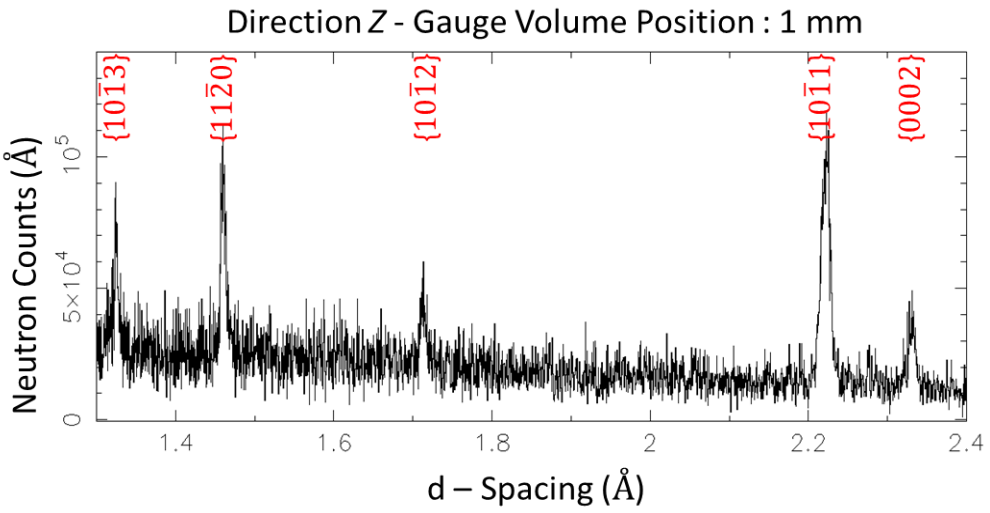
Direction Z - Gauge Volume Position : 1 mm
Neutron Counts (Å)
d – Spacing (Å)
{10$\bar{1}$3}
{11$\bar{2}$0}
{10$\bar{1}$2}
{10$\bar{1}$1}
{0002}

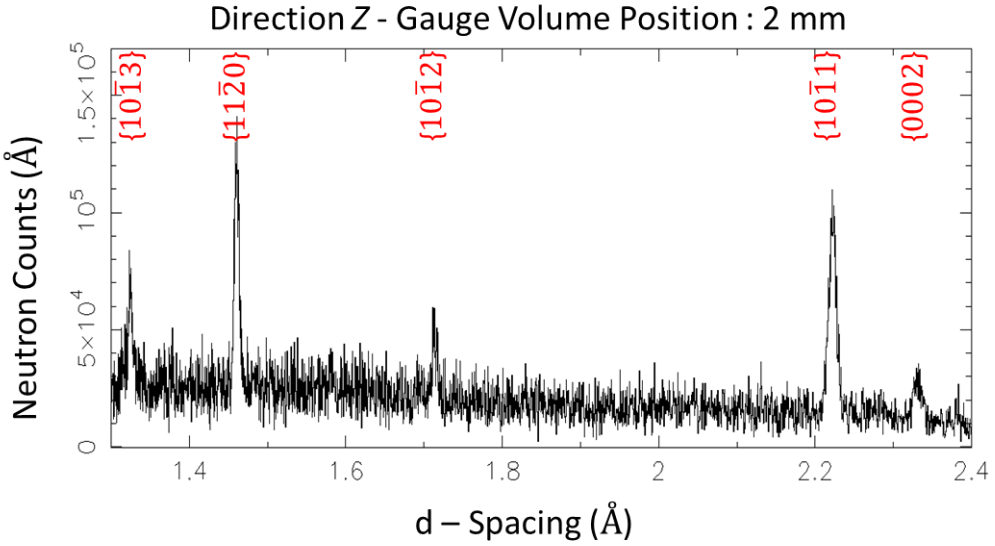
Direction Z - Gauge Volume Position : 2 mm
Neutron Counts (Å)
d – Spacing (Å)
{10$\bar{1}$3}
{11$\bar{2}$0}
{10$\bar{1}$2}
{10$\bar{1}$1}
{0002}

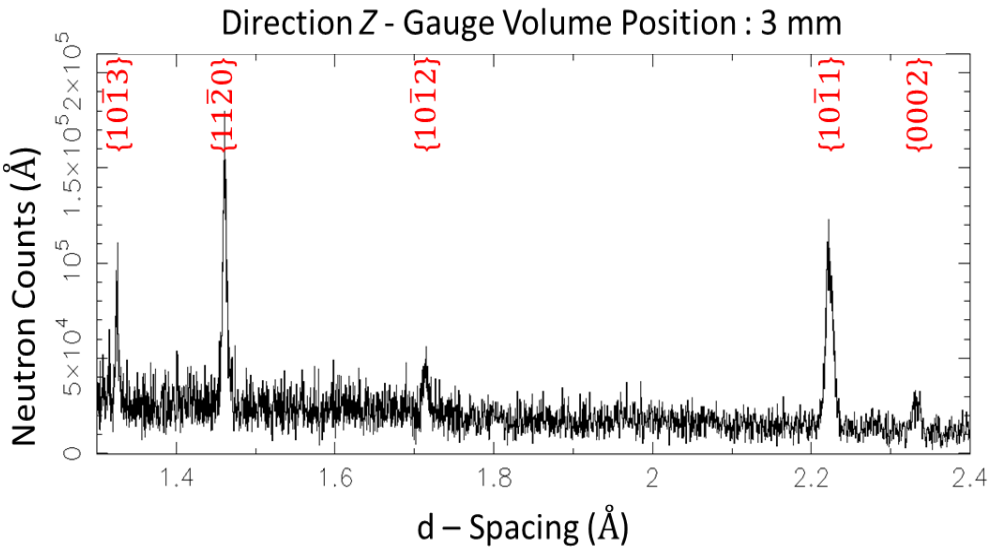
Direction Z - Gauge Volume Position : 3 mm
Neutron Counts (Å)
0
5×10^4
10^5
1.5×10^5
2×10^5
{10$\bar{1}$3}
{11$\bar{2}$0}
{10$\bar{1}$2}
{10$\bar{1}$1}
{0002}
1.4
1.6
1.8
2
2.2
2.4
d – Spacing (Å)

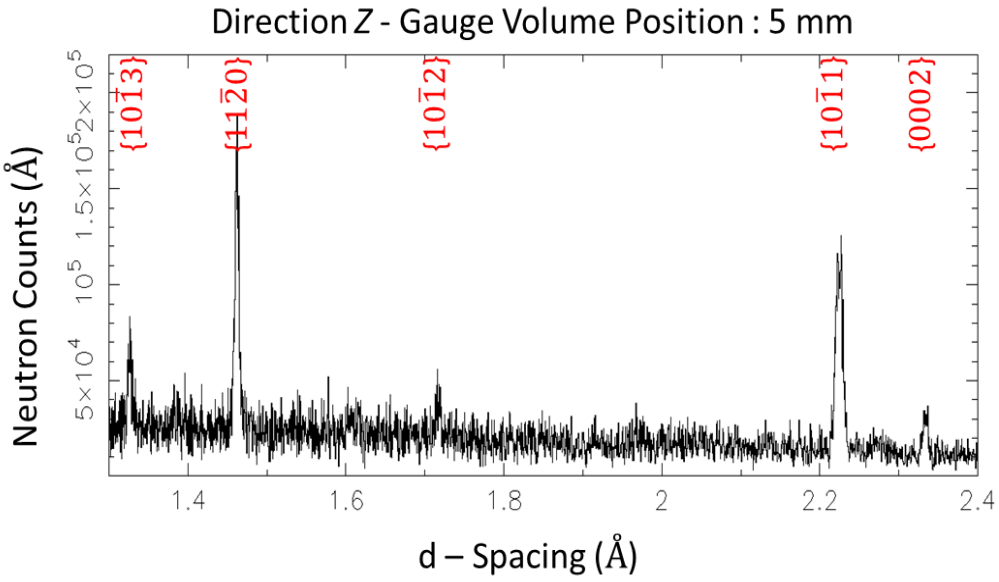
Direction Z - Gauge Volume Position : 5 mm
Neutron Counts (Å)
5×10^4
10^5
1.5×10^5
2×10^5
{10$\bar{1}$3}
{11$\bar{2}$0}
{10$\bar{1}$2}
{10$\bar{1}$1}
{0002}
1.4
1.6
1.8
2
2.2
2.4
d – Spacing (Å)

Appendix D: Example of propagation of fitting errors to calculate residual stress in the *x* direction

For a given position, the lattice dimensions a_x, a_y and a_z and their fitting errors Δa_x, Δa_y and Δa_z (respectively a_{0x}, a_{0y}, a_{0z} and Δa_{0x}, Δa_{0y}, Δa_{0z} for the stress-free lattice dimensions) are obtained from the post-processing of the diffraction peaks presented in 0. Consequently, the following strains can be calculated:

$\varepsilon_{x,a_x} = \frac{a_x - a_{0x}}{a_{0x}}$; $\varepsilon_{x,a_{x\,error}} = \frac{(a_x + \Delta a_x) - a_{0x}}{a_{0x}}$ and $\varepsilon_{x,a_{0x\,error}} = \frac{a_x - (a_{0x} + \Delta a_{0x})}{(a_{0x} + \Delta a_{0x})}$

Separated contributions of fitting errors Δa_x and Δa_{0x} on the strain are respectively:

$\Delta\varepsilon_{x,a_x} = \varepsilon_{x,a_{x\,error}} - \varepsilon_{x,a_x}$ and $\Delta\varepsilon_{x,a_{0x}} = \varepsilon_{x,a_{0x\,error}} - \varepsilon_{x,a_x}$

Therefore, the error made on the strain ε_x after propagation of fitting errors is:

$$\Delta\varepsilon_x = \sqrt{{\Delta\varepsilon_{x,a_x}}^2 + {\Delta\varepsilon_{x,a_{0x}}}^2}$$

Similarly, $\Delta\varepsilon_y$ and $\Delta\varepsilon_z$ can be calculated.

According to the Hooke's law:

$$\sigma_x = \frac{\nu E}{(1+\nu)(1-2\nu)}\left(\varepsilon_x + \varepsilon_y + \varepsilon_z\right) + \frac{E}{1+\nu}\varepsilon_x$$

Therefore,

$$\sigma_{x,x\,error} = \frac{\nu E}{(1+\nu)(1-2\nu)}\left((\varepsilon_x + \Delta\varepsilon_x) + \varepsilon_y + \varepsilon_z\right) + \frac{E}{1+\nu}(\varepsilon_x + \Delta\varepsilon_x)$$

$$\sigma_{x,y\,error} = \frac{\nu E}{(1+\nu)(1-2\nu)}\left((\varepsilon_x + (\varepsilon_y + \Delta\varepsilon_y) + \varepsilon_z\right) + \frac{E}{1+\nu}\varepsilon_x)$$

$$\sigma_{x,z\,error} = \frac{\nu E}{(1+\nu)(1-2\nu)}\left((\varepsilon_x + \varepsilon_y + (\varepsilon_z + \Delta\varepsilon_z)\right) + \frac{E}{1+\nu}\varepsilon_x)$$

Separated contributions of fitting errors $\Delta\varepsilon_x$, $\Delta\varepsilon_y$ and $\Delta\varepsilon_z$ on the stress are:

$\Delta\sigma_{x,x\ error} = \sigma_{x,x\ error} - \sigma_x$, $\Delta\sigma_{x,y\ error} = \sigma_{x,y\ error} - \sigma_x$ and $\Delta\sigma_{x,z\ error} = \sigma_{x,z\ error} - \sigma_x$

Therefore, the error made on the stress σ_x after propagation of fitting errors is:

$$\Delta\sigma_x = \sqrt{\Delta\sigma_{x,x\ error}{}^2 + \Delta\sigma_{x,y\ error}{}^2 + \Delta\sigma_{x,z\ error}{}^2}$$

Similarly, $\Delta\sigma_y$ and $\Delta\sigma_z$ can be calculated.

Appendix E: Response surface methodology

The raw data used to build the numerical models in the analysis of variance using response surface methodology are listed below:

Model Number	α (°C)	β ($m^{0.8}$)	P (Pa)	Lxx (m)	Lzz (m)	Clp_Px (Pa)	Clp_Pz (Pa)
1	879	4000	1.25E+08	0.02	0.2	1.25E+08	0.00E+00
2	1379	1700	6.25E+07	0.2	0.2	0.00E+00	1.25E+08
3	879	300	0.00E+00	0.2	0.11	0.00E+00	0.00E+00
4	879	2150	1.25E+08	0.02	0.02	1.25E+08	0.00E+00
5	1129	4000	0.00E+00	0.02	0.02	1.25E+08	0.00E+00
6	1379	4000	0.00E+00	0.11	0.2	0.00E+00	0.00E+00
7	879	4000	0.00E+00	0.02	0.2	6.25E+07	0.00E+00
8	879	300	1.25E+08	0.2	0.2	1.25E+08	0.00E+00
9	879	2150	1.25E+08	0.2	0.2	0.00E+00	0.00E+00
10	1379	1700	0.00E+00	0.02	0.02	6.25E+07	1.25E+08
11	879	4000	1.25E+08	0.2	0.02	1.25E+08	0.00E+00
12	879	4000	0.00E+00	0.02	0.02	1.25E+08	1.25E+08
13	879	300	0.00E+00	0.11	0.2	0.00E+00	1.25E+08
14	1129	1000	0.00E+00	0.02	0.2	0.00E+00	0.00E+00
15	1379	4000	1.25E+08	0.02	0.02	1.25E+08	1.25E+08
16	879	4000	1.25E+08	0.02	0.2	0.00E+00	1.25E+08
17	1004	3250	3.13E+07	0.15	0.15	9.38E+07	9.38E+07
18	879	300	0.00E+00	0.02	0.11	1.25E+08	0.00E+00
19	879	4000	0.00E+00	0.2	0.02	0.00E+00	0.00E+00
20	1129	4000	0.00E+00	0.2	0.2	0.00E+00	1.25E+08
21	879	300	1.25E+08	0.2	0.02	1.25E+08	1.25E+08

22	1129	1000	0.00E+00	0.2	0.02	0.00E+00	1.25E+08
23	879	300	1.25E+08	0.11	0.02	0.00E+00	0.00E+00
24	1379	1700	6.25E+07	0.02	0.02	1.25E+08	0.00E+00
25	879	300	1.25E+08	0.02	0.2	6.25E+07	1.25E+08
26	1379	4000	6.25E+07	0.2	0.2	1.25E+08	0.00E+00
27	1379	1700	0.00E+00	0.2	0.2	1.25E+08	6.25E+07
28	879	300	0.00E+00	0.02	0.02	0.00E+00	6.25E+07
29	1379	4000	0.00E+00	0.02	0.2	1.25E+08	1.25E+08
30	1379	4000	1.25E+08	0.02	0.2	6.25E+07	0.00E+00
31	1379	4000	1.25E+08	0.2	0.02	0.00E+00	0.00E+00
32	1379	4000	0.00E+00	0.2	0.11	1.25E+08	1.25E+08
33	1379	1700	1.25E+08	0.11	0.2	1.25E+08	1.25E+08
34	879	2150	0.00E+00	0.2	0.02	1.25E+08	0.00E+00
35	1379	1700	0.00E+00	0.11	0.02	0.00E+00	0.00E+00
36	879	4000	6.25E+07	0.02	0.02	0.00E+00	0.00E+00
37	879	4000	1.25E+08	0.2	0.2	1.25E+08	1.25E+08
38	879	300	1.25E+08	0.02	0.2	0.00E+00	0.00E+00
39	1379	1700	1.25E+08	0.02	0.11	0.00E+00	1.25E+08
40	879	4000	1.25E+08	0.2	0.02	0.00E+00	1.25E+08
41	1379	1700	1.25E+08	0.2	0.02	6.25E+07	1.25E+08
42	1379	1700	0	0.2	0.2	1.25E+08	0
43	879	300	0	0.02	0.02	0	0
44	879	4000	6.25E+07	0.02	0.02	0	6.25E+07
45	879	4000	6.25E+07	0.02	0.02	6.25E+07	0.00E+00
46	1379	4000	6.25E+07	0.02	0.02	6.25E+07	0.00E+00
47	1379	1700	0.00E+00	0.2	0.2	0.00E+00	0.00E+00
48	1129	1700	0.00E+00	0.2	0.2	0.00E+00	0.00E+00

49	879	300	1.25E+08	0.02	0.2	1.25E+08	1.25E+08
50	879	300	1.25E+08	0.02	0.11	0.00E+00	0.00E+00
51	879	300	1.25E+08	0.2	0.02	6.25E+07	1.25E+08
52	879	300	1.25E+08	0.2	0.02	0	0
53	879	300	1.25E+08	0.02	0.02	0	0
54	879	600	1.25E+08	0.02	0.02	0	0
55	879	600	1.25E+08	0.11	0.02	0	0
56	879	600	1.25E+08	0.02	0.11	0	0
57	879	400	1.25E+08	0.11	0.02	0	0
58	879	400	1.25E+08	0.02	0.11	0	0
59	879	500	1.25E+08	0.11	0.02	0	0
60	879	500	1.25E+08	0.02	0.11	0	0
61	979	4000	0	0.14	0.02	0	0
62	979	4000	0	0.2	0.02	0	0
63	979	4000	0	0.02	0.14	0	0
64	979	4000	0	0.02	0.2	0	0
65	979	3000	0	0.14	0.02	0	0
66	979	3000	0	0.2	0.02	0	0
67	979	3000	0	0.02	0.14	0	0
68	979	3000	0	0.02	0.2	0	0
69	979	2000	0	0.14	0.02	0	0
70	979	2000	0	0.2	0.02	0	0
71	979	2000	0	0.02	0.14	0	0
72	979	2000	0	0.02	0.2	0	0
73	979	4000	0	0.1	0.02	0	0
74	979	3000	0	0.1	0.02	0	0
75	979	2000	0	0.1	0.02	0	0

76	979	4000	0	0.02	0.1	0	0
77	979	3000	0	0.02	0.1	0	0
78	979	2000	0	0.02	0.1	0	0
79	979	4000	0	0.02	0.02	0	0
80	979	3000	0	0.02	0.02	0	0
81	979	4000	0	0.05	0.02	0	0
82	979	3000	0	0.05	0.02	0	0
83	979	4000	0	0.02	0.02	0	0
84	979	3000	0	0.02	0.02	0	0
85	979	4000	0	0.02	0.05	0	0
86	979	3000	0	0.02	0.05	0	0
87	1379	4000	0	0.2	0.02	0	0
88	1379	2800	0	0.2	0.02	0	0
89	1379	1700	0	0.2	0.02	0	0
90	1379	4000	0	0.02	0.2	0	0
91	1379	2800	0	0.02	0.2	0	0
92	1379	1700	0	0.02	0.2	0	0
93	1379	4000	0	0.1	0.02	0	0
94	1379	2800	0	0.1	0.02	0	0
95	1379	1700	0	0.1	0.02	0	0
96	1379	4000	0	0.02	0.1	0	0
97	1379	2800	0	0.02	0.1	0	0
98	1379	1700	0	0.02	0.1	0	0
99	1379	4000	0	0.02	0.02	0	0
100	1379	2800	0	0.02	0.02	0	0
101	1379	1700	0	0.02	0.02	0	0